The Planetary Science Journal, 7:216 (30pp), 2026 September https://doi.org/10.3847/PSJ/ae9d79
© 2026. The Author(s). Published by the American Astronomical Society.
OPEN ACCESS

A Whole-planet Model of the Earth without Life for Terrestrial Exoplanet Studies

Samantha Gilbert-Janizek[1], Rory K. Barnes[1], Peter E. Driscoll[2], Nicholas F. Wogan[3,4], Avi M. Mandell[5,6], Jessica L. Birky[7], Ludmila Carone[8], and Rodolfo Garcia[1]
[1] Department of Astronomy and Astrobiology Program, University of Washington, Box 351580, Seattle, WA 98195, USA; samroseg@uw.edu
[2] Earth and Planets Laboratory, Carnegie Institution for Science, Washington, DC 20015, USA
[3] SETI Institute, Mountain View, CA 94043, USA
[4] NASA Ames Research Center, Moffett Field, CA 94035, USA
[5] NASA Goddard Space Flight Center, 8800 Greenbelt Road, Greenbelt, MD 20771, USA
[6] Sellers Exoplanet Environment Collaboration, 8800 Greenbelt Road, Greenbelt, MD 20771, USA
[7] Astronomy Department, University of Washington, Seattle, WA 98195, USA
[8] Space Research Institute, Austrian Academy of Sciences, Schmiedlstrasse 6, A-8042 Graz, Austria
Received 2026 January 28; revised 2026 July 24; accepted 2026 August 17; published 2026 September 18

Abstract

As the only known habitable (and inhabited) planet in the Universe, Earth informs our search for life elsewhere. Future telescopes like the Habitable Worlds Observatory (HWO) will soon look for life on rocky worlds around Sun-like stars, so it is critical that we understand how to distinguish habitable planets from inhabited planets. However, it remains unknown if life is necessary to maintain a habitable planet, or how all of the components of an evolving planet impact habitability over time. As a first step toward answering these questions, we present a coupled interior-atmosphere evolution model of the Earth without life from 50 Myr to 5 Gyr that reproduces 19 key observations of the preindustrial Earth after 4.5 Gyr within estimated measurement uncertainties. We also produce a reflected-light spectrum covering the possible wavelength range of HWO. Our findings suggest that life may not be required to maintain long-term habitable surface conditions. The model presented here is apt for predicting the long-term habitability of Earth-like exoplanets by coupling the interior and surface evolution. By generating realistic reflected-light spectra from evolved atmospheric states, this model represents significant progress towards characterizing the observability of whole-planet evolution, which may ultimately provide a robust abiotic baseline for interpreting biosignature observations with HWO.

Unified Astronomy Thesaurus concepts: Exoplanet evolution (491); Exoplanet plate tectonics (493); Exoplanet surface characteristics (496); Exoplanets (498); Habitable planets (695); Extrasolar rocky planets (511); Exoplanet astronomy (486); Exoplanet atmospheres (487); Exoplanet atmospheric evolution (2308); Exoplanet atmospheric composition (2021); Exoplanet surface composition (2022); Exoplanet surfaces (2118)

1. Introduction

Earth is currently the only known inhabited planet in the Universe, and geological evidence suggests that it was habitable with liquid-water oceans for most of its 4.54 Gyr history (E. M. Cameron et al. 2024). Owing to its long-term habitability, Earth serves as the template that guides our search for biospheres elsewhere. Consequently, a validated model of the entire planet is valuable for both understanding our own planet and optimizing the search for life on worlds outside the solar system. Building on previous studies, here we present a coupled one-dimensional (1D) core–mantle–crust–climate model of the Earth that reproduces 19 key observations of the preindustrial Earth (PIE) within estimated measurement uncertainties.

An open question regarding Earth's evolution is whether or not it could be habitable over billion-year timescales without life's influence on the environment. The idea that life plays an active role in maintaining conditions favorable to its survival is popularly known as the "Gaia hypothesis" (J. E. Lovelock & L. Margulis 1974). Clearly, biology plays an important role in Earth's surface environment, which motivates our central question: Is life *required* to maintain the long-term habitability of a rocky planet?

As a first step toward answering this question, we simulate the Earth through time without life, with the goal of reproducing the habitable conditions of the PIE after 4.5 Gyr. We define habitability as the conditions required to maintain liquid water on the planetary surface (e.g., S. H. Dole & I. Asimov 1964; T. D. Robinson 2018). Ultimately, whether or not life is a requirement for long-term habitability has vast implications for the search for life on exoplanets; if life is not required for habitability, then the detection of habitable conditions alone is insufficient evidence for life. Instead, distinguishing inhabited from habitable and uninhabited worlds will require identifying atmospheric gases or surface features that can only be produced by life.

Developing this capability is critical as next-generation telescopes like the Habitable Worlds Observatory (HWO) prepare to search for life on nearby exoplanets. HWO is a planned space-based, infrared (IR)/optical/ultraviolet (UV) direct-imaging telescope of 6 m or larger that will discover and characterize Earth-like planets around Sun-like stars (National Academies of Sciences, Engineering, and Medicine 2021; E. Mamajek & K. Stapelfeldt 2023; L. D. Feinberg et al. 2026). The proper interpretation of photometry and spectroscopy of the "pale dots" detected in the habitable zones (HZs) of nearby stars with HWO is predicated on a complete and self-consistent model of Earth-like planets, defined as rocky

Original content from this work may be used under the terms of the Creative Commons Attribution 4.0 licence. Any further distribution of this work must maintain attribution to the author(s) and the title of the work, journal citation and DOI.

planets with approximately Earth's mass and radius (E. T. Wolf et al. 2017) and active interior-atmosphere volatile exchange (F. Rodler & M. López-Morales 2014; S. Fan et al. 2019). This broad definition likely includes planets with diverse compositions (S.-H. Shim 2014; A. Santerne et al. 2018), atmospheric structures (G. Vladilo et al. 2013), stellar hosts (E. Mamajek & K. Stapelfeldt 2023), instellations (R. K. Kopparapu et al. 2013), and even habitable planets that never developed life (C. S. Cockell 2014; R. Wordsworth & R. Pierrehumbert 2014; M. López-Morales et al. 2019; J. Krissansen-Totton et al. 2021). The atmospheres of "abiotic Earths" must be well quantified to serve as null hypotheses for identifying life's signatures and ruling out its imitators, or "false positives," on exoplanets observed with HWO (V. S. Meadows et al. 2018; J. Krissansen-Totton et al. 2021; T. Constantinou et al. 2026).

Many studies have simulated the coevolution of the Earth and Sun based on geological evidence (M. E. Barley et al. 2005; P. Kharecha et al. 2005; A. L. Zerkle et al. 2012; B. Charnay et al. 2013; G. Arney et al. 2016; J. Krissansen-Totton et al. 2018; D. C. Catling & K. J. Zahnle 2020; N. F. Wogan et al. 2022) and extrapolated these results to predict the conditions of Earth-like planets around other stars (A. Segura et al. 2005; L. Kaltenegger et al. 2007; A. Segura et al. 2010; E. A. Frank et al. 2014; M. Godolt et al. 2015, 2016; G. N. Arney et al. 2017; S. Gebauer et al. 2017; E. T. Wolf et al. 2017; S. Rugheimer & L. Kaltenegger 2018; G. N. Arney 2019; A. V. Young et al. 2024). The existing work largely models the atmospheric evolution of these systems by coupling climate to photochemistry to achieve atmospheric compositions that are in radiative–convective equilibrium. However, atmospheric evolution cannot be fully understood in isolation from interior processes that regulate volatile cycling through the crust and mantle.

The emerging concept of "whole-planet" modeling was first introduced in a pair of papers (P. Driscoll & D. Bercovici 2013; B. J. Foley & P. E. Driscoll 2016) that argued long-term habitability depends on evolving interior-atmosphere volatile exchange. B. J. Foley & P. E. Driscoll (2016) argue that climate influences whether or not plate tectonics develops, as low surface temperatures promote long-lived weak sheer zones, or "damage," in the lithosphere. In turn, plate tectonics facilitates volatile recycling at plate boundaries, which is particularly important for stabilizing the climate via the carbon cycle (J. C. Walker et al. 1981; R. A. Berner et al. 1983). The carbon cycle, therefore, can also affect the cooling rate of the interior by modulating mantle viscosity and melting, which influence tectonics and heat loss from the mantle, ultimately influencing the core cooling rate and thus magnetic field generation (B. J. Foley & P. E. Driscoll 2016). Because core convection and magnetic field strength are directly tied to the core's thermal and compositional evolution, the present-day magnetic field provides an independent observational constraint on a planet's internal dynamics, offering a valuable calibration point for whole-planet models. Finally, the strength of the planetary magnetic field has been hypothesized to affect the rate of atmospheric escape, potentially playing a role in the desiccation of Venus and thus its distinct evolutionary path (A. J. Watson et al. 1981; P. Driscoll & D. Bercovici 2013; C. Gillmann et al. 2022); the direct causal link between field strength and escape rates, however, remains an active area of research (e.g., H. Gunell et al. 2018).

Despite its potential importance, many questions about whole-planet modeling remain. J. Krissansen-Totton et al. (2021) developed a rigorously coupled mantle–surface–atmosphere model that includes a magma ocean phase and a transition from a mobile lid to plate tectonics, to explore the long-term carbon and oxygen cycles. However, they did not focus on the coupled evolution of the mantle and core, instead assuming that the core cooling decays exponentially. Drawing on the ideas of F. Nimmo (2002), M. Armann & P. J. Tackley (2012) argue that the surface and core are interconnected, demonstrating that an episodic stagnant lid can suppress core cooling.

Building on this work, R. Garcia et al. (2026) produced a coupled 1D solar–atmosphere–lithosphere–mantle–core model of Venus that reproduces present-day atmospheric H_2O and CO_2 abundances and the lack of a core dynamo. Their ability to fully validate the model is limited by the dearth of observations of Venus's surface and interior. Furthermore, as in P. Driscoll & D. Bercovici (2013), R. Garcia et al. (2026) assume a gray atmospheric model. To calculate the planet's energy balance, J. Krissansen-Totton et al. (2021) use a precalculated radiative-transfer grid to solve for the wavelength-dependent outgoing long-wave radiation (OLR) from the planet, and use a simple parameterization of albedo, planet–star distance, and stellar luminosity to solve for the absorbed short-wave radiation (ASR). Thus, no whole-planet evolutionary model yet includes radiative-transfer calculations to solve for the ASR and OLR balance of the changing planetary climate as well as the magnetic field evolution of the core. By adding these features to our whole-planet model, we can incorporate additional constraints on its evolution and potential habitability.

The presence of these interconnected feedback mechanisms make clear that long-term planetary evolution cannot be fully understood by studying individual subsystems in isolation. The stellar environment, atmosphere, surface, mantle, and core form a coupled system in which changes in one component may cascade to the whole system over geological timescales. For example, the evolution of atmospheric composition—the primary observable for missions like HWO—is mediated not only by photochemistry and climate, but also by outgassing set by mantle convection and water content, which in turn depend on the thermal state of the core and mantle. To correctly interpret observations of Earth-like exoplanets and establish a robust null hypothesis for biosignature detection, we require validated whole-planet models that self-consistently track the coevolution of all major planetary reservoirs. The PIE, with its relatively well-constrained properties across all subsystems, provides one possible validation target for such models.

Here, we present a 1D core–mantle–crust–climate model of the abiotic Earth that tracks the evolution of the core–mantle system, geochemistry, atmosphere, incoming solar flux, and solar effective temperature over the age of the solar system. We use our model to broadly reproduce observed quantities of the PIE. We choose this calibration point as the modern Earth is not in radiative balance due to human-driven climate change. Due to large uncertainties in early Earth conditions, we do not attempt to validate the model on the conditions of the early Earth. Finally, as a proof of concept, we demonstrate that atmospheric states from our model can be used to generate realistic reflected-light spectra comparable to observations HWO will obtain of Earth-like exoplanets.

In the following Section 2, we discuss the known properties of the PIE to establish our model's validation targets. Then, we

describe the whole-planet abiotic Earth model in Section 3, and present its validated results in Section 4. We discuss future model upgrades as well as potential applications of our validated model for HWO observations of Earth-like exoplanets in Section 5. Finally, we summarize our results and conclusions in Section 6.

2. Properties of the Preindustrial Earth

The "preindustrial" era defines the period of Earth's history prior to the Industrial Revolution (c. 1800), when widespread changes to human land use and atmospheric pollution first arose (E. Hawkins et al. 2017). From records, geological evidence, and modeling reconstructions, the PIE is known to have had lower atmospheric and ocean CO_2 concentrations and cooler global average surface temperatures than today. Measurements of these properties with their uncertainties and corresponding sources are summarized in Table 1. We report interior properties based on present-day measurements because (1) preindustrial measurements of these properties are largely nonexistent, and (2) mantle and core properties evolve on a sufficiently slow timescale that any variation from their present-day values should be insignificant. Similarly, we assume that the total mass of the ocean has not varied significantly in the last 300 yr.

2.1. Atmosphere

Earth retains a 1 bar atmosphere consisting of 78% N_2 (United States Committee on Extension to the Standard Atmosphere 1976). Oxygen, which comprises 21% of our atmosphere, became a major constituent after the proliferation of photosynthetic life (L. R. Kump 2008; J. Farquhar et al. 2011; T. W. Lyons et al. 2014). The remaining atmosphere consists of "trace components," including CO_2 and H_2O, which are effective greenhouse gases that help regulate planetary climate (J. Tyndall 1861). Water vapor is the most efficient greenhouse gas (J. R. Fleming 1998), and because warmer air can hold more water vapor, the atmospheric abundance of H_2O relates to global temperature in a positive feedback loop (I. M. Held & B. J. Soden 2000; V. K. Patel & J. Kuttippurath 2023). However, water vapor's short atmospheric residence time of ∼10 days (K. E. Trenberth 1998)—set by condensation and precipitation—means that H_2O cannot itself act as a long-term climate forcing. Instead, the noncondensing greenhouse gases such as CO_2, with atmospheric lifetimes of centuries to millennia, set the temperature structure that determines the equilibrium water-vapor abundance (A. A. Lacis et al. 2010). Below, we detail measurements of Earth's atmospheric CO_2 and H_2O abundances, as well as global average surface temperature.

A record of atmospheric CO_2 levels has been pieced together by analyzing air trapped in polar ice sheets. D. M. Etheridge et al. (1996) analyzed air bubbles in Antarctic ice cores dating back to 1000 C.E., finding that preindustrial atmospheric CO_2 abundances were around 280 ppm with annual fluctuations of ∼4 ppm. In Earth's 1 bar atmosphere (101,325 Pa), this abundance is equivalent to a partial pressure of 28.4 ± 0.4 Pa.

The abundance of H_2O in our atmosphere varies with latitude, with higher abundances in the humid tropics (S. Mockler 1995; R. P. Allan et al. 2022), as well as altitude, with much higher abundances below the atmospheric cold trap (A. Brewer 1949; W. Randel & M. Park 2019). The abundance and distribution of water vapor is also seasonally variable, but the resulting change to the global atmosphere is small, on the order of $\pm 1 \times 10^{15}$ kg H_2O, or less than 0.02% of the total atmospheric mass (K. E. Trenberth et al. 1987). Satellite and sounding measurements have provided anchor points for 1D

Table 1
Selected Properties of the Preindustrial Earth

Property	Value	Reference (s)
Atmosphere		
Atmospheric CO_2 (pCO_2)	28.4 ± 0.4 Pa	(1)
Atmospheric H_2O (pH_2O)	900 ± 700 Pa	(2), (3)
Global avg. surface temperature (T_{surf})	286.9 ± 0.1 K	(4), (5)
Surface		
Ground albedo (A_g)	0.14 ± 0.02	(6)–(8)
Ocean mass (w_{ocean})	1.4×10^{21} kg (1 TO)	(9)
Oceanic $(CO_2)_{aq}$	8 ± 2 μmol kg^{-1}	(10)
Surface ocean total dissolved inorganic carbon (DIC)	2000 ± 200 μmol kg^{-1}	(10), (11)
Ocean pH	8.18 ± 0.05	(12)
Interior		
Upper-mantle temperature (T_{UM})	1587^{+161}_{-34} K	(13)
Core–mantle boundary temp. (T_{CMB})	4000 ± 200 K	(14)
Upper-mantle heat flow (Q_{UM})	38 ± 3 TW	(13)
Core–mantle boundary heat flow (Q_{CMB})	11 ± 6 TW	(13)
Upper TBL viscosity (ν_{UM})[a]	$10^{17.38\pm1}$ m^2 s^{-1} ($10^{20.9\pm1}$ Pa·s)	(15)–(18)
Lower TBL viscosity (ν_{LM})[a]	$10^{17.28\pm1}$ m^2 s^{-1} ($10^{21.0\pm1}$ Pa·s)	(15)–(18)
Upper-mantle melt fraction (f_{UM})	11.5 ± 3.5%	(19)
Mantle melt mass flux	(1.3 ± 0.8) × 10^6 kg kg^{-1}	(20), (21)
Inner-core radius (R_{IC})	1221 ± 1 km	(22)
Magnetic moment	80 ± 4 ZAm^2 (1.00 ± 0.05 E.U.)	(23), (24)
Magnetopause radius	9.10 ± 0.14 $R_\oplus$ (1.00 ± 0.02 E.U.)	(25)

Note.
[a] Viscosities at the inner edges of the two thermal boundary layers (TBLs; ∼100 km depth and ∼300 km above the core–mantle boundary present day). Nominal values are the median of central values from references (15)–(18); the ±1 dex uncertainty reflects interstudy disagreement. Kinematic values assume ρ = 3300 and 5200 kg m^{-3} at the respective depths.

References. (1) D. M. Etheridge et al. (1996); (2) T. D. Robinson et al. (2011); (3) J. Lustig-Yaeger et al. (2023); (4) E. Hawkins & R. Sutton (2016); (5) E. Hawkins et al. (2017); (6) S. Solomon et al. (2007); (7) J. S. Kargel et al. (2014); (8) H. Genda (2016); (9) M. A. Charette & W. H. Smith (2010); (10) R. A. Feely et al. (2001); (11) M. Eide et al. (2017); (12) L.-Q. Jiang et al. (2019); (13) C. Jaupart et al. (2015); (14) K. Hirose et al. (2013); (15) A. Paulson et al. (2005); (16) J. Mitrovica & A. Forte (2004); (17) H. C. Lau et al. (2016); (18) B. Steinberger & A. R. Calderwood (2006); (19) A. Gale et al. (2013); (20) J.-P. Cogné & E. Humler (2004); (21) J. Li et al. (2015); (22) A. M. Dziewonski & D. L. Anderson (1981); (23) I. de Pater & J. Lissauer (2010); (24) M. G. Kivelson & F. Bagenal (2014); (25) calculated by P. Driscoll & D. Bercovici (2013) using equations from J.-M. Grießmeier et al. (2004).

models to map the vertical distribution of water vapor throughout Earth's atmosphere; for example, T. D. Robinson et al. (2011) analyzed archived satellite data corresponding to the dates of the EPOXI Earth-flyby mission in 2008, extracting water-vapor abundance profiles at latitudes of 0°, 19°, 41°, and 66° (J. Lustig-Yaeger et al. 2023; see their Figure 4). Each latitude profile represents the globally averaged vertical profile for all HEALPix bins with the corresponding north and south latitudes. The mean water-vapor profile includes a near-surface water-vapor volume mixing ratio of 0.0089, with near-surface abundances of 0.0158 and 0.00182 for the mean profiles acquired at 0° and 66°, respectively (J. Lustig-Yaeger et al. 2023). Treating the equatorial and midlatitude averages as upper and lower bounds, these measurements correspond to a present-day partial pressure of 900 ± 700 Pa, a large uncertainty that reflects the strong latitude dependency of near-surface water-vapor abundances.

Earth's global average surface temperature can be traced through time directly via historical records, and indirectly by estimating evolving radiative forcings, using global climate model simulations, and finally by compiling proxy evidence from tree rings, corals, and ice cores. E. Hawkins et al. (2017) combined all of these approaches to estimate that preindustrial temperatures were 0.55°C–0.80°C cooler than the global average surface temperature from 1986 to 2005. Establishing the corresponding 1986–2005 baseline as 14.4°C (E. Hawkins & R. Sutton 2016), we therefore assume the preindustrial global average surface temperature to be 286.9 ± 0.1 K (E. Hawkins et al. 2017).

2.2. Surface Properties

To first order, Earth's surface includes exposed land, oceans, and polar ice caps. These three surface types, along with atmospheric water-vapor clouds, contribute to the overall brightness or albedo of the planet, regulating planetary absorption of stellar radiation. In addition to H_2O, the oceans contain dissolved inorganic carbon (DIC) in the form of aqueous CO_2, carbonate (CO_3^{2-}), and bicarbonate (HCO_3^-), which together mediate the overall pH of the marine environment.

Earth sustains a surface liquid-water ocean of mass 1.4×10^{21} kg, or, by definition, 1 terrestrial ocean (TO; M. A. Charette & W. H. Smith 2010). Earth's vast oceans are a major carbon sequestration reservoir. Atmospheric CO_2 dissolves into the oceans as aqueous CO_2 and reacts with water to form carbonic acid, which dissociates into H^+ and HCO_3^-, which itself dissociates into H^+ and CO_3^{2-} (M. E. Pilson 2012).

Studies of ocean carbon isotopic fractionation reveal that the preindustrial oceanic carbon budget is largely abiotic. Since photosynthetic respiration preferentially uses the ^{12}C isotope (M. H. O'Leary 1981), ocean water enriched in heavier ^{13}C indicates abiotic DIC (P. Quay et al. 2003). Isotopic fractionation studies suggest nonhuman biological activity accounts for only ∼2% of the total DIC in the oceans (D. Carroll et al. 2022). Though marine life pumps dissolved carbon from the near-surface water column to the deep ocean (F. A. Le Moigne 2019), gravitational sinking dominates carbon export in modern oceans (P. W. Boyd et al. 2019; M. Nowicki et al. 2022; D. A. Siegel et al. 2023). Recent work using models to reconstruct preindustrial ocean chemistry supports near-surface, preindustrial DIC concentrations of 2000 ± 200 μmol kg^{-1} (R. A. Feely et al. 2001; M. Eide et al. 2017), an aqueous CO_2 concentration of 8 ± 2 μmol kg^{-1} (R. A. Feely et al. 2001), and a global average surface ocean pH of 8.18 ± 0.05 (L.-Q. Jiang et al. 2019).

Planetary surface albedo, a linear combination of albedo contributions from different surface types and clouds, affects climate by regulating the Earth's ASR from the Sun. Based on data from spectral libraries (A. M. Baldridge et al. 2009; R. N. Clark et al. 2003), previous planetary modeling work assumes that the albedos of seawater, rock, and ice are largely wavelength independent (L. Kaltenegger et al. 2007; P. Driscoll & D. Bercovici 2013), where ocean albedo $A_{oc} = 0.1$, rock albedo $A_r = 0.17$, and ice albedo $A_i = 0.6$. The ocean covers 71% of Earth's surface area (H. Genda 2016), and the remainder comprises land with seasonal variations in ice coverage.

Satellite measurements have been used to quantify a perennial surface ice area of 16.01–16.04 × 10^6 km^2 (S. Solomon et al. 2007; J. S. Kargel et al. 2014), or a perennial ice surface fraction of 3.4% that implies a remaining ice-free land surface fraction of 25.6%. On Earth, most of the ice-less land is covered by vegetation (D. Chu 2019), with 54% grasslands ($A \sim 0.4$) and 30% forests ($A \sim 0.1$). Since we are investigating an abiotic planet without life of any kind, we will assume that the surface of the abiotic Earth would instead be dominated by rock. Calculating the total expected ground albedo (A_g) as a linear combination of surface fraction and albedo contributions, we thus calculate $A_g = 0.14$. Seasonal changes in Earth's albedo imply variations of ± 0.02 (F. L. Bartman 1980).

In reality, Earth's *total* albedo also receives major contributions from atmospheric water-vapor clouds, as satellite measurements suggest Earth's total albedo is closer to $A_T = 0.29$ (B. A. Wielicki et al. 1996; N. G. Loeb et al. 2009). This total albedo is ∼0.15 brighter than the composite ground albedo because clouds are highly reflective and they partially block the path of stellar radiation to the ground (V. Ramanathan et al. 1989; E. F. Harrison et al. 1990). For an albedo representing an average of thick and thin clouds, I. de Pater & J. Lissauer (2010) and P. Driscoll & D. Bercovici (2013) use $A_{cl} = 0.89$.

2.3. Interior

Beneath a thin crustal layer, Earth has a convecting solid mantle, molten outer core, and solid iron inner core. Here, we describe how various measurements and models have been used to establish values (with uncertainties) for key core and mantle properties of the Earth, including temperature, heat flow, viscosity, upper-mantle melt fraction, and magnetic moment. These properties are not independent: Mantle viscosity governs convective vigor and plate speed, which in turn set the rates of volatile outgassing and regassing that control atmospheric CO_2 and H_2O content. As discussed in Section 1, the magnetic moment and magnetopause radius provide an additional, independent observational constraint on the planet's evolving internal heat budget, since core convection and magnetic field generation are directly tied to the thermal and compositional evolution of the core–mantle system. These interior properties control the dynamical processes that ultimately shape the planet's evolving surface habitability.

The mantle geotherm describes how the laterally averaged temperature of the mantle changes with depth. The temperature of the mantle at various depths may be estimated using

petrological constraints on the temperature of mid-ocean ridge basalts (MORB; R. J. Kinzler & T. L. Grove 1992) and the identification of several important phase changes: the 440 km-deep olivine–wadsleyite phase change (T. Katsura et al. 2004), the 660 km-deep postspinel phase transition (T. Katsura et al. 2003), and the inner-core boundary (ICB; D. Alfè et al. 2002; S. Labrosse 2003; C. Jaupart et al. 2015). Using the depths of these phase changes as anchor points, previous studies have used isentropic profiles combined with thermal boundary layers (TBLs) to describe a continuous mantle geotherm (e.g., T. Katsura et al. 2004; P. Driscoll & D. Bercovici 2014). Synthesizing these measurements and models has resulted in the following literature estimates for the temperature of the upper mantle (at the base of the lithosphere) and the core–mantle boundary (CMB): $T_{\rm UM} = 1587^{+161}_{-34}$ K (C. Jaupart et al. 2015) and $T_{\rm CMB} = 4000 \pm 200$ K (K. Hirose et al. 2013), respectively.

Over geological time, the mantle undergoes solid-state convection, transporting heat from the CMB to the surface. The viscosity of the mantle, an important quantity for determining the vigor of mantle convection and heat transfer, is expected to vary significantly between the upper and lower mantle due to variations in temperature, pressure, and composition (R. Jeanloz & S. Morris 1986; R. Boehler 1996; C. Jaupart et al. 2015). Mantle viscosity is not merely a descriptive feature of the present-day Earth: It is a material transport property that plays a central role in controlling the long-term evolution of the interior. Water content and heat reduce mantle viscosity, enhancing convective vigor and plate speed, which accelerates the rates of volatile regassing and degassing that set atmospheric composition over time (J. Seales & A. Lenardic 2020; R. Garcia et al. 2026). We describe how viscosity enters our convection and plate-speed parameterization in Section 3.

The radial viscosity structure of the mantle has been inferred from glacial isostatic adjustment (GIA) observations, joint inversions of GIA and mantle convection data, and geodynamically optimized profiles (J. Mitrovica & A. Forte 2004; A. Paulson et al. 2005; B. Steinberger & A. R. Calderwood 2006; H. C. Lau et al. 2016). Though the inferred viscosity profiles differ in places, the depths corresponding to the two TBL edges yield per-study central values of $[10^{20.5}$–$10^{21.25}]$ Pa·s at ∼100 km depth and $[10^{20}$–$10^{22}]$ Pa·s at ∼300 km above the CMB. We adopt the median of the per-study central values as our nominal targets, $\eta_{\rm UM} = 10^{20.9}$ Pa·s and $\eta_{\rm LM} = 10^{21.0}$ Pa·s, with an adopted uncertainty of ±1 order of magnitude. This envelope reflects the disagreement found among independent inversions arising from differing ice histories, tomographic models, regularization, and treatment of deep radial structure. Indeed, the interstudy variability often exceeds the formal posterior width of any single study. Some *bulk* lower-mantle viscosity estimates ($\gtrsim 10^{22}$ Pa·s) exceed our adopted estimate, likely because they do not account for temperature in the lower-mantle TBL approaching its melting temperature, which will significantly decrease the local viscosity. In fact, models that explicitly resolve the structure in the lowermost mantle do show viscosity decreasing around the lower-mantle TBL (J. Mitrovica & A. Forte 2004; B. Steinberger & A. R. Calderwood 2006). Assuming densities of $\rho_{\rm UM} = 3300$ kg m^{-3} and $\rho_{\rm LM} = 5200$ kg m^{-3} at the respective boundary-layer depths, these correspond to nominal kinematic viscosities of $\nu_{\rm UM} \approx 2.4 \times 10^{17}$ m^2 s^{-1} and $\nu_{\rm LM} \approx 1.9 \times 10^{17}$ m^2 s^{-1}.

Although surface measurements constrain the upper-mantle heat flow to $Q_{\rm UM} = 38 \pm 3$ TW (C. Jaupart et al. 2015), the CMB heat flow cannot be measured directly. However, the temperature jump across the lower-mantle TBL can be constrained by extrapolating the mantle geotherm down and the ICB temperature up to the CMB. This approach, combined with the estimated viscosity of the lower mantle, typically gives an estimate of $Q_{\rm CMB}$ to be 11 ± 6 TW (C. Jaupart et al. 2015). Thermal evolution models of the Earth, therefore, should be within these margins of uncertainty to be considered accurate.

The subduction of Earth's tectonic plates drives the upwelling of ambient mantle at mid-ocean ridges, facilitating the cycling of volatiles between the solid interior and atmosphere over geological timescales. The fraction of upwelling mantle that melts and its rate of flow determine the melt mass flux, which also plays a role in heat transport and can have a direct impact on planetary thermal evolution. The extent of melting of MORB has been estimated by compiling various measurements of basalt chemistry as a function of axial depth, and averaging the data over large distances to account for small-scale variability in basalt composition (E. M. Klein & C. H. Langmuir 1987). This analysis suggests that the average extent of MORB melting is 8%–15% (A. Gale et al. 2013).

Measurements of crustal production rates at plate boundaries probe mantle melting by providing estimates on the upward mass flux of mantle melt. J.-P. Cogné & E. Humler (2004) used direct measurements of currently visible seafloor surfaces bounded by pairs of geophysical isochrones in the Atlantic, Indian, Antarctic, Pacific, Nazca, and Cocos ocean basins to estimate a seafloor production rate of 5–15 km^3 yr^{-1}. J. Li et al. (2015) used three-dimensional (3D) seismic tomography to measure magmatic accretion at the Southwest Indian Ridge, measuring a crustal production rate of ∼20 km^3 yr^{-1} and providing an upper bound on mantle melt mass flux. Assuming an upper-mantle density of ∼3300 kg m^{-3}, a crustal production rate range of 5–20 km^3 yr^{-1} corresponds to a mantle melt mass flux of $(1.3 \pm 0.8) \times 10^6$ kg s^{-1} (values below zero not permitted). The amount of heat transported by the melt has been estimated to be ∼1.5 TW (T. Nakagawa & P. J. Tackley 2012).

Earth's magnetic field is generated by convection in its liquid iron outer core. Core convection is primarily generated compositionally through the solidification of the solid iron inner core, where light elements are rejected into the liquid, thereby decreasing the local density of the fluid and driving fluid flow. The radius of the inner core has been measured to high precision by seismographs, yielding $R_{\rm IC} = 1221 \pm 1$ km (A. M. Dziewonski & D. L. Anderson 1981).

Key measurements of the terrestrial magnetic field include the dipolar magnetic moment, which quantifies the strength of the core field, and magnetopause radius, which is the boundary between the terrestrial magnetic field and that of the solar wind. Measurements of Earth's magnetic field suggest a terrestrial magnetic moment of 80 ZAm^2 (I. de Pater & J. Lissauer 2010; M. G. Kivelson & F. Bagenal 2014), which we define as 1 Earth unit. Similarly, using the stand-off distance equation from J.-M. Grießmeier et al. (2004), P. Driscoll & D. Bercovici (2013) calculated a magnetopause radius of ∼9.1 Earth radii

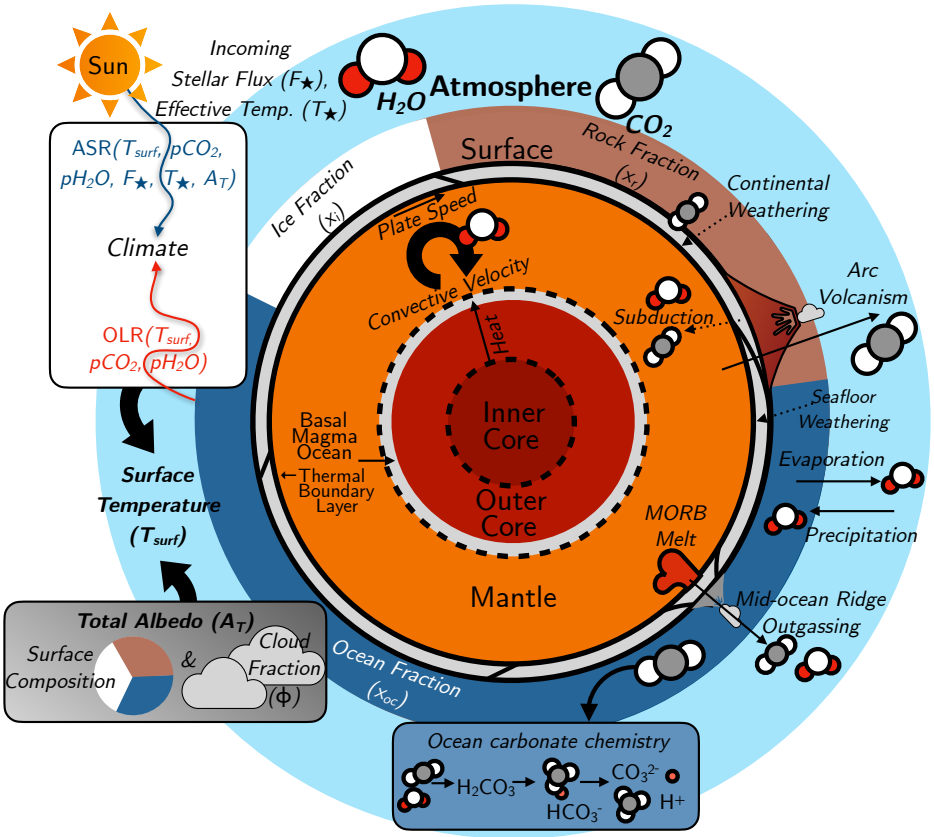


Figure 1. A schematic of the key processes included in our abiotic Earth model. Remotely observable quantities (surface temperature, albedo, and atmospheric H_2O and CO_2) are in bold. Volatile cycling is diagrammed in more detail in Figure 2.

(P. Driscoll & D. Bercovici 2013), which we also define as 1 Earth unit. This calculated value is consistent with previous measurements from geosynchronous satellites, which suggested a plausible magnetopause radius range between 9 and 10 $R_\oplus$ (J.-H. Shue et al. 1998). While the values for both the magnetic field moment and magnetopause radius lack formal uncertainty estimates, we adopt conservative validation tolerances of ± 0.015 Earth units for the magnetopause radius and ± 0.05 Earth units for the magnetic moment. These $\leqslant 5\%$ tolerances effectively account for known variability in these quantities: The location of the magnetopause varies with solar wind conditions, while the magnetic dipole moment exhibits secular variation.

3. Methods

Our fully coupled model builds on `VPLanet` (R. Barnes et al. 2020; R. Garcia et al. 2026) by incorporating published models of the carbon cycle (B. J. Foley 2015), deep water cycle (J. Seales & A. Lenardic 2020), surface hydrological cycle (P. Driscoll & D. Bercovici 2013), and climate (N. F. Wogan et al. 2025b) for planets with plate tectonics. Our abiotic Earth model components are summarized in the schematic in Figure 1, with a more detailed schematic of CO_2 and H_2O cycling between the interior, surface, and atmosphere shown in Figure 2.

In this section, we describe the assumptions and governing equations used to upgrade `VPLanet`'s `ThermInt` module. Any equations and physical parameters not detailed here are implemented as described by R. Barnes et al. (2020, their Appendix K). Model constants are defined in Appendix A.

3.1. Model Assumptions

We make several simplifying assumptions about interior and atmosphere processes for model tractability. For the interior, we assume that the model is initialized immediately following the solidification of the magma ocean. Since this brief phase (1–10 Myr) likely dictated the initial composition of the atmosphere (L. T. Elkins-Tanton 2008; K. Hamano et al. 2013; H. Lammer et al. 2018; E. E. Stueeken et al. 2020; K.-H. Chao et al. 2021; L. Carone et al. 2025), we choose a set of appropriate initial conditions that apply after the bulk of the mantle has solidified.

We also assume active plate tectonics throughout Earth's history, consistent with Earth–Moon geology that suggests plate tectonics began as early as the middle Hadean (S. Maruyama et al. 2018). A number of alternative hypotheses for Earth's tectonic evolution exist, including transitions from a stagnant-lid mode to modern plate tectonics during the Archean (K. C. Condie et al. 2016), from sluggish to active-lid convection (M. Al Asad & H. C. Lau 2024), or a slowdown in plate velocity due to compositional buoyancy and lithospheric stiffening (J. Korenaga 2006). Since we validate our model only against PIE properties, assessing the tectonic regime during the Hadean and Archean is outside the scope of this work.

For the atmosphere, as in previous work (J. Krissansen-Totton et al. 2021), we assume that the atmosphere maintains a constant 1 bar of N_2, since our 1 bar, abiotic atmospheres lack photosynthetic oxygen. Since abiotic methane sources generate fluxes several orders of magnitude lower than biological production (G. Etiope & B. Sherwood Lollar 2013;

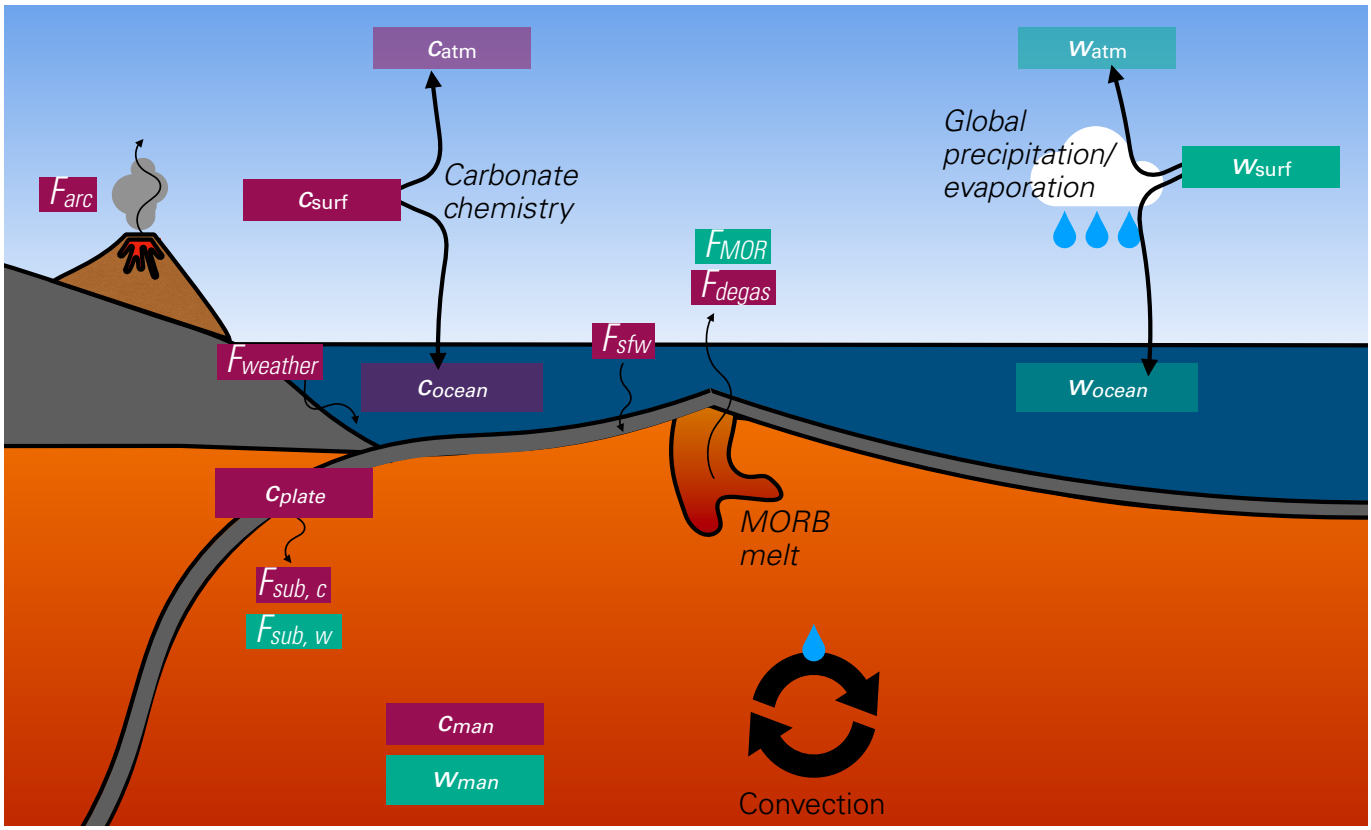


Figure 2. A schematic showing the atmospheric sources and sinks that define the new volatile cycling processes in `VPLanet`'s `ThermInt` module, inspired by Figure 1 in B. J. Foley (2015). Fluxes related to CO_2 are color-coded magenta, and fluxes related to H_2O are color-coded teal. We incorporate the climate-stabilizing carbon cycle from B. J. Foley (2015), tracking the mass of CO_2 across the mantle (c_{man}), plate (c_{plate}), and surface (c_{surf}) reservoirs. We include the deep water cycle from J. Seales & A. Lenardic (2020), and a precipitation/evaporation parameterization from P. Driscoll & D. Bercovici (2013), which allow us to track the mass of H_2O across the mantle (w_{man}) and surface (w_{surf}) reservoirs. At each time step, surface carbon and water are partitioned into the atmosphere (c_{atm}, w_{atm}) and the ocean (c_{ocean}, w_{ocean}) by enforcing equilibrium at the air–water boundary. This schematic does not depict the modeled ocean chemistry.

N. Wogan et al. 2020; M. A. Thompson et al. 2022), we focus our model on CO_2 and H_2O as the primary greenhouse gases regulating climate on an Earth without life, with a discussion of reduced species in Section 5.2. Additionally, we assume atmospheric escape is negligible, including magnetically mediated escape processes, in our model. The present-day escape rate is small: Observed hydrogen loss rates are negligible relative to Earth's volatile inventories over the model integration time, and the tropopause cold trap keeps most of the water-vapor inventory close to the surface (J. F. Kasting et al. 1984; F. Tian et al. 2013; G. Gronoff et al. 2020).

Extending this assumption to earlier epochs, when the strength of the geodynamo may have differed, requires further justification, which we base on two considerations. First, the effect of a weaker paleofield on escape is uncertain: A planetary magnetosphere may suppress some escape channels (sputtering and ion pickup) while enabling others (polar cap and cusp outflow), resulting in a nonmonotonic relationship between magnetic field strength and total escape rate (H. Gunell et al. 2018; G. Gronoff et al. 2020). Second, the strongest empirical constraint on Earth's integrated escape history, the xenon isotope record, admits interpretations ranging from the loss of an ocean's worth of hydrogen to little escape at all (see Section 5.5). Given these open questions, we choose zero escape as a reasonable limiting case for Earth, and leave coupled escape processes as future work (Section 5.6).

Finally, we acknowledge that due to large uncertainties in early Earth conditions, we validate the model only against properties of the PIE. We therefore use observed preindustrial continental weathering rates as our reference, acknowledging that these rates likely reflect some degree of biological enhancement by land vegetation and soil microbial communities. However, the quantitative contribution of biology to silicate weathering rates remains poorly constrained, with field estimates of the biotic enhancement factor spanning nearly 2 orders of magnitude (e.g., M. Ford Cochran & R. A. Berner 1996; C. Dessert et al. 2003), and no true abiotic control site exists on Earth today (B. Wild et al. 2022). We discuss addressing these uncertainties in Section 5.

3.2. Core, Mantle, and Basal Magma Ocean

We use the `VPLanet` core–mantle interior module, `ThermInt`, and the radiogenic heating module, `RadHeat`, as described by R. Barnes et al. (2020). We make two key modifications to the nominal model: (1) a basal magma ocean (BMO) layer, which treats radiogenic heating contributions from both the core and the BMO in one combined term prior to present-day solidification, and (2) a mantle viscosity influenced by the water content in the mantle as described in R. Garcia et al. (2026). The mantle water content is controlled by the deep water cycle and is described in Section 3.4.

Earth's mantle may have solidified from the middle out (C.-É. Boukaré et al. 2025), where a prolonged BMO would have

solidified slowly and become enriched in incompatible elements, including radiogenic species of K, Th, and U (S. Labrosse et al. 2007). With potential enrichment as high as ~200 times that of the bulk silicate Earth (S. Labrosse et al. 2007), the BMO may have provided a stable, thermally insulating layer that slowed core cooling. However, the existence of the BMO is not yet widely accepted (M. G. Jackson et al. 2010; I. H. Campbell & H. S. C. O'Neill 2012; R. W. Carlson et al. 2014). For example, I. H. Campbell & H. S. C. O'Neill (2012) note that the measured heat flux from upper-mantle plumes is inconsistent with a radioactively enriched layer in the lower mantle. To capture the thermal effect of an enriched BMO, we define a new effective BMO + core radiogenic heating rate, $Q_{\mathrm{rad,BMO+C}} = Q_{\mathrm{rad,BMO}} + Q_{\mathrm{rad,C}}$ that folds in the radiogenic heating of the BMO. With this modification, the core energy balance in `ThermInt` becomes

$$\dot{T_C} = \frac{Q_{\mathrm{rad,BMO+C}} - Q_{\mathrm{BMO}}}{M_C c_C - \frac{dM_{\mathrm{IC}}}{dT_C}(L_H + E_G)}, \tag{1}$$

where M denotes mass, c_C denotes the core specific heat capacity, $\dot{T}$ denotes the evolving reservoir temperature, and Q denotes heat flow. The subscripts indicate the relevant reservoir, where "C," "CMB," and "BMO" represent the core, core–mantle boundary, and basal magma ocean layer, respectively. Thus, $Q_{\mathrm{rad,BMO}}$ represents the radiogenic heat production in the BMO, and $Q_{\mathrm{rad,C}}$ represents the radiogenic heat production in the core. Additionally, $\frac{dM_{\mathrm{IC}}}{dT_C}$ is the derivative of the inner-core mass with respect to core temperature, and L_H and E_G give the latent and gravitational energy released at the ICB per unit mass. For the full derivation, see Appendix B.

This approach approximates the effect of a BMO enriched in radiogenic elements without modeling its solidification. In reality, as the mantle gradually solidifies downward toward the core and the liquid BMO shrinks, it becomes further enriched in radiogenic elements (S. Labrosse et al. 2007). This effectively maintains a higher concentration of radiogenic elements outside the core and provides a stable, thermally insulating layer.

To match estimates of upper-mantle heat flow within uncertainties, we find that our model requires approximately 3.5 TW of combined core and lower-mantle radiogenic power by 4.5 Gyr. Given that core radiogenic heating today is thought to be significantly lower than this amount (K. Watanabe et al. 2014; I. Blanchard et al. 2017; P. Faure et al. 2020), the bulk of the heating must come from the BMO. To assess whether this excess heating is physically plausible, we calculate the total present-day heat budget from a thin, enriched BMO layer.

S. Labrosse et al. (2007) estimate that if the early Earth's magma ocean gradually solidified downward toward the core, incompatible radiogenic elements would be expelled from solid-mantle minerals and concentrated in the remaining liquid BMO. They find that the primordial BMO could be enriched in the main radioactive elements (^{40}K, ^{232}Th, ^{235}U, and ^{238}U) by 200 times their concentrations in the bulk silicate Earth (see their Figure 4). Assuming the BMO is a spherical shell with a thickness of 4 km and that it is slightly denser than the solid mantle due to its relative enrichment in iron (6000 kg m^{-3}), we find a present-day combined heating budget of 3.67 TW due to ^{40}K, ^{232}Th, ^{235}U, and ^{238}U. This calculation demonstrates that attributing 3.5 TW of core heating to a radiogenically enriched, thin, long-lived BMO is physically plausible.

3.3. Carbon Cycle

The model conserves the mass of CO_2 over geological time as it cycles between three reservoirs: the mantle (c_{man}), plate (c_{plate}), and surface (c_{surf}), which includes the ocean (c_{ocean}) and atmosphere (c_{atm}) reservoirs. At each time step, we calculate the following fluxes as in B. J. Foley (2015): arc volcanic (F_{arc}), continental weathering (F_{weather}), seafloor weathering (F_{sfw}), degassing (F_{degas}), and subduction ($F_{\mathrm{sub,c}}$) (see Figure 2). The fluxes are balanced between the planet's CO_2 reservoirs according to the following equations (B. J. Foley 2015):

$$\dot{c}_{\mathrm{plate}} = \frac{F_{\mathrm{weather}}}{2} + F_{\mathrm{sfw}} - F_{\mathrm{sub,c}}, \tag{2}$$

$$\dot{c}_{\mathrm{man}} = \chi_{\mathrm{sub,c}} F_{\mathrm{sub,c}} - F_{\mathrm{degas}}, \tag{3}$$

where $\chi_{\mathrm{sub},c}$ is a factor that represents the subduction efficiency. The continental weathering flux is divided by a factor of 2 to account for the fact that half of the carbon initially sunk into the continental plate is returned to the atmosphere when carbonates form on the seafloor (R. A. Berner et al. 1983; B. J. Foley 2015). Finally, we have

$$\dot{c}_{\mathrm{surf}} = F_{\mathrm{arc}} + F_{\mathrm{degas}} - \frac{F_{\mathrm{weather}}}{2} - F_{\mathrm{sfw}}, \tag{4}$$

where by mass conservation $c_{\mathrm{surf}} = c_{\mathrm{atm}} + c_{\mathrm{ocean}}$ (see Section 3.6 for a detailed description of partitioning CO_2 into the atmosphere and ocean).

We define the fluxes according to B. J. Foley (2015), with some minor changes. The subduction flux is given by

$$F_{\mathrm{sub}} = 2 c_{\mathrm{plate}} v L \frac{d_{\mathrm{melt}}}{V_{\mathrm{man}}}, \tag{5}$$

where v is the speed of the tectonic plates (see below), L is the present-day length of the ocean trenches, d_{melt} is the depth to the base of the upper-mantle melt region (see R. Barnes et al. 2020, their Appendix K), and V_{man} is the volume of the mantle. The $d_{\mathrm{melt}}/V_{\mathrm{man}}$ term represents division by the effective area of the mantle melt. The arc volcanic flux is subsequently defined as

$$F_{\mathrm{arc}} = (1 - \chi_{\mathrm{sub,c}}) F_{\mathrm{sub}}, \tag{6}$$

where $1 - \chi_{\mathrm{sub,c}}$ is the fraction of subducting carbon that degasses. The degassing flux is therefore given by

$$F_{\mathrm{degas}} = 2 f_{\mathrm{UM}} \chi_{\mathrm{degas,c}} c_{\mathrm{man}} \frac{v L d_{\mathrm{melt}}}{V_{\mathrm{man}}}, \tag{7}$$

where f_{UM} is the upper-mantle melt fraction, $\chi_{\mathrm{degas,c}}$ is the fraction of the melted mantle that degasses, and V_{man} is the volume of the mantle. We include the additional f_{UM} term to ensure that the degassing flux is tightly coupled to the size of the melt layer. As in B. J. Foley (2015), we assume that the length of the ocean ridges is equivalent to that of the trenches. We note that the upper-mantle melt fraction describes partial melting of the upwelling mantle, and not the whole-mantle volumetric melt fraction sometimes used in models that parameterize the solidification of the magma ocean (e.g., L. T. Elkins-Tanton 2008; J. Krissansen-Totton et al. 2021).

The arc and ridge degassing fluxes are the CO_2 sources in the surface (atmosphere + ocean). Both terms include

efficiency factors $\chi_{\rm sub,c}$ and $\chi_{\rm degas,c}$. We calibrate these factors to give a total carbon outgassing flux similar to present-day observations of $\sim$7.5 T mol yr^{-1} (D. C. Catling & J. F. Kasting 2017), as well as PIE $p{\rm CO}_2$ values.

Prior to subduction, seafloor and continental weathering deposit carbon into the oceanic plate. The seafloor and continental weathering fluxes strongly influence the $p{\rm CO}_2$ evolution in our model. B. J. Foley (2015) gives the seafloor weathering flux as

$$F_{\rm sfw} = F_{\rm sfw,0}\left(\frac{v}{v_0}\right)\left(\frac{p{\rm CO}_2}{p{\rm CO}_{2,0}}\right)^{\alpha}, \tag{8}$$

where $F_{\rm sfw,0}$ is the present-day seafloor weathering flux, v_0 is the present-day speed of the tectonic plates, $p{\rm CO}_2$ is the partial pressure of CO$_2$, $p{\rm CO}_{2,0}$ is its present-day value, and α quantifies the dependence of basalt carbonation on atmospheric CO$_2$. J. Krissansen-Totton et al. (2018) showed that seafloor weathering should include a strong temperature dependence to reproduce the Cenozoic $^{87}{\rm Sr}/^{86}{\rm Sr}$ record. Incorporating an Arrhenius temperature relation from J. Krissansen-Totton et al. (2018), our seafloor weathering equation becomes

$$F_{\rm sfw} = F_{\rm sfw,0}\left(\frac{v}{v_0}\right)\left(\frac{p{\rm CO}_2}{p{\rm CO}_{2,0}}\right)^{\alpha} \times \exp\left(\frac{E_{\rm bas}}{R_{\rm g}}\left(\frac{1}{T_{\rm pore,0}} - \frac{1}{T_{\rm pore}}\right)\right), \tag{9}$$

where $E_{\rm bas} = 92$ kJ mol^{-1} is the empirically derived activation energy for basalt weathering (L. A. Coogan & S. E. Dosso 2015), $R_{\rm g}$ is the universal gas constant, $T_{\rm pore}$ is the pore-space temperature, and $T_{\rm pore,0}$ is its modern-day value. The pore-space temperature is directly related to deep-ocean temperatures ($T_{\rm D}$; L. A. Coogan & S. E. Dosso 2015), which in turn are related to the global mean surface temperature ($T_{\rm surf}$; see Section 3.8). By fitting empirical data on global mean surface temperature and deep-ocean temperature, J. Krissansen-Totton et al. (2018) give $T_{\rm pore} = T_{\rm D} + 9$ and $T_{\rm D} = a_{\rm grad}T_{\rm surf} + b_{\rm int}$, with $a_{\rm grad} = 1.02$ and $b_{\rm int} = -16.7$ as the best-fit parameters.

Finally, B. J. Foley (2015) derives a continental weathering flux that accounts for supply-limited behavior at high $p{\rm CO}_2$ such that

$$F_{\rm weather} = F_{\rm weather,s} \times \left\{1 - \exp\left[-\frac{F_{\rm weather,0}}{F_{\rm weather,s}}\frac{x_{\rm r}}{x_{\rm l,0}} \times \left(\frac{p{\rm CO}_2}{p{\rm CO}_{2,0}}\right)^{\beta_1}\left(\frac{P_{\rm sat}}{P_{\rm sat,0}}\right)^{a_1} \times \exp\left(\frac{E_{\rm a}}{R_{\rm g}}\left(\frac{1}{T_{\rm surf,0}} - \frac{1}{T_{\rm surf}}\right)\right)\right]\right\}, \tag{10}$$

where $F_{\rm weather,s}$ is the supply limit to weathering, $F_{\rm weather,0}$ is the present-day silicate weathering rate, β_1 is the partial pressure of CO$_2$ ($p{\rm CO}_2$) scaling parameter for silicate weathering, $P_{\rm sat}$ is the saturation vapor pressure, $P_{\rm sat,0}$ is the present-day saturation vapor pressure, a_1 is the saturation vapor pressure scaling parameter for silicate weathering, $E_{\rm a}$ is the activation energy of the weathering reaction, and $T_{\rm surf,0}$ is the present-day surface temperature. The equation also includes a term that scales the evolving exposed-rock fraction, $x_{\rm r}$, at a given time step by the present-day land fraction, $x_{\rm l,0}$. The treatment of evolving surface composition is described in further detail in Section 3.7.

The supply limit to weathering represents the maximum achievable flux given the available weatherable rock on the surface of the planet. We calculate the supply limit using the relation $F_{\rm weather,s} = (A_{\rm Earth}x_{\rm r}E_{\rm max}f_{\rm cc}\,\rho_{\rm r})/\bar{m}_{\rm cc}$, where $E_{\rm max}$ is the maximum erosion rate, $f_{\rm cc}$ is the fraction of Mg, Ca, K, and Na in the continental crust, $\rho_{\rm r}$ is the density of the regolith, and $\bar{m}_{\rm cc}$ is the average molar mass of Mg, Ca, K, and Na (B. J. Foley 2015). Mg, Ca, K, and Na are relevant as these are the weatherable components of felsic continental crust (A. J. West 2012). This relation gives the supply limit in units of mol s^{-1}, which we convert to kg s^{-1} by multiplying by the molar mass of CO$_2$, $\bar{m}_{\rm c}$. The saturation vapor pressure is related to its present-day value and the surface temperature of the planet according to the relation

$$P_{\rm sat} = P_{\rm sat,ref}\exp\left[-\frac{\bar{m}_{\rm w}L_{\rm w}}{R_{\rm g}}\left(\frac{1}{T_{\rm surf}} - \frac{1}{T_{\rm sat,ref}}\right)\right], \tag{11}$$

where $\bar{m}_{\rm w}$ is the molar mass of water, $L_{\rm w}$ is the latent heat of water, and $T_{\rm sat,0}$ is the reference saturation vapor temperature (P. Driscoll & D. Bercovici 2013).

The fluxes $F_{\rm arc}$, $F_{\rm sfw}$, $F_{\rm degas}$, and $F_{\rm sub,c}$ are related to the speed of the tectonic plates, v. We implement the J. Seales & A. Lenardic (2020) parameterization, which relates v to the mantle Rayleigh number:

$$v = \frac{a_2\kappa}{2(R_{\rm man} - R_c)}\left(\frac{\rm Ra}{\rm Ra_{crit}}\right)^{2\beta_2}, \tag{12}$$

where a_2 and β_2 are scaling terms, κ is the thermal diffusivity, $R_{\rm man}$ is the radius of the mantle, $R_{\rm c}$ is the radius of the core, Ra is the mantle Rayleigh number (see R. Barnes et al. 2020, their Appendix K), and ${\rm Ra}_{\rm crit} = 660$ is the critical Rayleigh number.

3.4. Water Cycle

We track the mass of water as it cycles between the mantle ($w_{\rm man}$) and the surface ($w_{\rm surf}$), which includes the ocean ($w_{\rm ocean}$), and the atmosphere ($w_{\rm atm}$), via a subduction flux ($F_{\rm sub,w}$) and a mid-ocean ridge degassing flux ($F_{\rm MOR}$). The fluxes balance according to the following system of differential equations:

$$\dot{w}_{\rm man} = F_{\rm sub,w} - F_{\rm MOR} \tag{13}$$

and

$$\dot{w}_{\rm surf} = F_{\rm MOR} - F_{\rm sub,w}, \tag{14}$$

where mass conservation requires that $w_{\rm surf} = w_{\rm ocean} + w_{\rm atm}$.

The abundance of water in the mantle impacts the viscosity of the upper mantle and thus the efficiency of heat transfer via the Arrhenius viscosity. R. Garcia et al. (2026) give the Arrhenius component of the viscosity as

$$\nu_{\rm Arr} = \nu_{\rm ref}\exp\left[\frac{E_{\rm a,man}}{T_{\rm UM}R_{\rm g}} - \frac{\Delta E_{\rm H_2O}(w_{\rm man}/M_{\rm man})}{T_{\rm UM}R_{\rm g}}\right], \tag{15}$$

where $\nu_{\rm ref}$ is the reference viscosity of the upper mantle, $E_{\rm a,man}$ is the viscosity activation energy of the upper mantle, $\Delta E_{\rm H_2O}$ is the depression of the mantle viscosity activation energy due to water, $M_{\rm man}$ is the mass of the mantle, and $T_{\rm UM}$ is the temperature of the upper mantle. The viscosity of the upper mantle (within ∼100 km depth of the upper TBL) is then calculated by dividing the Arrhenius viscosity term by the upper-mantle viscosity-melt factor (R. Garcia et al. 2026). The viscosity of the lower mantle (within ∼300 km depth of the CMB) is calculated by scaling the upper-mantle viscosity by a fixed viscosity ratio, a standard closure in parameterized thermal evolution models (P. Driscoll & D. Bercovici 2014; R. Barnes et al. 2020; V. Patočka et al. 2020). The melt viscosity factor is calculated following P. E. Driscoll & R. Barnes (2015). First, we define the normalized melt fraction:

$$\Phi = \frac{f_{\rm UM}}{\phi_s}, \tag{16}$$

where $f_{\rm UM}$ is the upper-mantle melt fraction and $\phi_s = 0.8$ is the reference melt fraction parameter. Next, we calculate the melt geometry factor:

$$F = (1 - \xi) \cdot \mathrm{erf}\left[\frac{\sqrt{\pi}}{2(1-\xi)}\Phi(1 + \Phi^{\gamma})\right], \tag{17}$$

where the viscosity-melt reduction coefficient $\xi = 5 \times 10^{-4}$, the viscosity-melt reduction exponent $\gamma = 6.0$, and erf is the error function. Finally, the melt viscosity reduction factor is given by

$$\eta_{\rm melt} = \frac{1 + \Phi^{\delta}}{(1 - F)^{B\phi_s}}, \tag{18}$$

where the viscosity-melt reduction exponent $\delta = 6.0$ and the viscosity-melt reduction parameter $B = 2.5$ (A. Costa et al. 2009). The mantle viscosity depends on melt fraction through the parameterization of A. Costa et al. (2009), which we adopt because it is constructed to be smooth and monotonic across the full range of melt fractions traversed by our model. The more general multiphase framework developed by T. Keller & J. Suckale (2019), spanning the full range of melt fractions, adopts this same relation as its reference effective-viscosity closure for basalt–olivine, showing that it reproduces the experimentally constrained exponential melt weakening at low melt fraction (G. Hirth & D. Kohlstedt 2003) while transitioning smoothly across the disaggregation threshold toward the solid limit—unlike diffusion-creep closures (Y. Takei & B. K. Holtzman 2009; J. F. Rudge 2018) or the Einstein–Roscoe relation, which drop to zero or introduce unrealistically sharp transitions at their critical fractions.

To calculate the fluxes of water into and out of the mantle, we assume the definitions of $F_{\rm sub,w}$ and $F_{\rm MOR}$ given by J. Seales & A. Lenardic (2020), so that

$$F_{\rm sub,w} = f_h \rho_{\rm man} D_{\rm hydr} S \chi_{\rm regas,w}, \tag{19}$$

where f_h is the mass fraction of water in the serpentinized layer, $\rho_{\rm man}$ is the density of the mantle, $D_{\rm hydr}$ is the thickness of the serpentinized layer, S is the spreading rate of the tectonic plates, and $\chi_{\rm regas,w}$ is the regassing efficiency factor. The thickness of the serpentinized layer is related to the surface temperature $T_{\rm surf}$ according to the relation $D_{\rm hydr} = (k|T_{\rm surf} - 973|)/q_{\rm m}$, where k is the thermal conductivity and $q_{\rm m}$ is the heat flux through the upper mantle (see R. Barnes et al. 2020, their Appendix K). Note that this parameterization of the subduction flux assumes that there is always a sufficient supply of water to drive the serpentinization reaction. The spreading rate is related to the speed of the plates as $2Lv$, where the factor of $2L$ represents bidirectional spreading.

The mid-ocean ridge degassing flux is thus given by

$$F_{\rm MOR} = \rho_{\rm man} f_{\rm UM} X_{\rm melt} d_{\rm melt} S \chi_{\rm degas,w}, \tag{20}$$

where $X_{\rm melt}$ is the abundance of water in the erupting magma and $\chi_{\rm degas,w}$ is the degassing efficiency factor. The parameters $f_{\rm UM}$ and $d_{\rm melt}$ are calculated as described by R. Barnes et al. (2020, their Appendix K), while the fraction of water in the melt can be found by taking $X_{\rm melt} = \chi_{\rm m}/[D_{\rm H_2O} + f_{\rm UM}(1 - D_{\rm H_2O})]$, where $\chi_{\rm m}$ is the mass fraction of water in the mantle ($w_{\rm man}/M_{\rm man}$) and $D_{\rm H_2O}$ is the bulk distribution coefficient (J. Seales & A. Lenardic 2020).

The mass of H_2O on the surface (atmosphere + ocean) results from the balance of the mid-ocean ridge degassing sources and the subduction sinks at the plate boundaries. In our model, both terms include degassing and regassing efficiency factors, $\chi_{\rm degas,w}$ and $\chi_{\rm regas,w}$, respectively. We tune these factors to give the PIE mass of water in the oceans and atmosphere after 4.5 Gyr, and to give a degassing flux on the order of present-day observations, ∼95 Tmol $\rm yr^{-1}$ (D. C. Catling & J. F. Kasting 2017).

3.5. Atmospheric Constituents

Our Earth-like atmospheres consist of N_2, H_2O, and CO_2. Atmospheric H_2O and CO_2 are allowed to vary based on the balance of sources and sinks from volatile cycling, while N_2 is kept at a constant 1 bar (see Section 3.1). In the model framework, we treat both H_2O and CO_2 as combined surface reservoirs. At each time step, we partition each gas between the atmosphere and the ocean by enforcing instantaneous equilibrium. Thus, by mass conservation, we require that $c_{\rm surf} = c_{\rm ocean} + c_{\rm atm}$ and $w_{\rm surf} = w_{\rm ocean} + w_{\rm atm}$. Here, we describe the partitioning of water, while the partitioning of CO_2 is described in the following subsection.

To maintain hydrostatic equilibrium at the air–water boundary, at each time step we partition water between the atmosphere and the ocean by initially calculating the mass of water in the atmosphere ($w_{\rm atm}$) in excess of the amount of moisture the air can hold at a given time step (P. Driscoll & D. Bercovici 2013). Since the Earth's oceans and atmosphere achieve equilibrium on the order of days, whereas `ThermInt` processes evolve on geological timescales, we assume that the flow of water between the atmosphere and ocean occurs instantaneously in the model. At each time step, we calculate the saturation vapor pressure (B. J. Foley 2015) as a function of $T_{\rm surf}$, and we then multiply by a factor of RH $\times$ $(M_{\rm atm,T}/P_{\rm T})$ $\times$ $(\bar{m}_{\rm w}/\bar{w}_{\rm atm})$ to obtain $m_{\rm moist}$, the maximum mass of water that the air can hold, where RH represents the tunable global average relative humidity.

When $w_{\rm atm} > m_{\rm moist}$, the excess water mass is subtracted from $w_{\rm atm}$ and added to $w_{\rm ocean}$. In the inverse case, when $w_{\rm atm}$

$< m_{\mathrm{moist}}$, to maintain equilibrium between the air and ocean, we subtract the mass difference from w_{ocean} and add it to w_{atm}. To obtain $p\mathrm{H_2O}$ in Pa, we convert w_{atm} to moles of $\mathrm{H_2O}$, divide by the total moles in the atmosphere, and multiply by P_{T}. This simplified zero-dimensional approximation provides the initial atmospheric $\mathrm{H_2O}$ partial pressure needed as input to the climate calculation (Section 3.8), where it is subsequently refined using the vertically resolved atmospheric structure.

3.6. Ocean Chemistry

The total reservoir of carbon in the ocean (total dissolved inorganic carbon, or DIC) is the sum of the aqueous $[\mathrm{CO_2}]$, $[\mathrm{CO_3^{2-}}]$, and $[\mathrm{HCO_3^-}]$. Since we enforce equilibrium at the air–ocean boundary, we assume that all ocean chemistry values are representative of surface waters. Initially, atmospheric $\mathrm{CO_2}$ dissociates in ocean water following Henry's law (M. E. Pilson 2012), which quantifies the solubility of a gas according to its partial pressure above a liquid, so that

$$(\mathrm{CO_2})_{\mathrm{aq}} = H \times p\mathrm{CO_2}, \tag{21}$$

where $(\mathrm{CO_2})_{\mathrm{aq}}$ gives the aqueous concentration of $\mathrm{CO_2}$ in units of mol $\mathrm{kg^{-1}}$ $\mathrm{H_2O}$, H is the Henry's law coefficient in units of mol $\mathrm{kg^{-1}}$ $\mathrm{atm^{-1}}$, and $p\mathrm{CO_2}$ is the partial pressure of atmospheric $\mathrm{CO_2}$. We obtain c_{ocean} by multiplying $(\mathrm{CO_2})_{\mathrm{aq}}$ by the total mass of water in the ocean, w_{ocean}, and the molar mass of $\mathrm{CO_2}$. By definition, $c_{\mathrm{atm}} = (p\mathrm{CO_2}/P_{\mathrm{T}}) \times (\bar{m}_{\mathrm{c}}/\bar{m}_{\mathrm{atm}}) \times M_{\mathrm{atm,T}}$, where P_{T} is the total pressure, $\bar{m}_{\mathrm{atm}}$ is the average molar mass of the atmosphere, and $M_{\mathrm{atm,T}}$ is the total mass of the atmosphere. Substituting $p\mathrm{CO_2} = \mathrm{CO_{2aq}}/H$ into the mass conservation constraint, we solve a quadratic equation to obtain $(\mathrm{CO_2})_{\mathrm{aq}}$ based on the integration of Equation (4) at each time step. Finally, to obtain $p\mathrm{CO_2}$ in Pa, we take the $(\mathrm{CO_2})_{\mathrm{aq}}$ solution and divide by the Henry's law coefficient, and convert from standard atmospheric pressure to Pa.

Next, aqueous $\mathrm{CO_2}$ and $\mathrm{H_2O}$ combine to make carbonic acid in the following equilibrium reaction:

$$(\mathrm{CO_2})_{\mathrm{aq}} + \mathrm{H_2O} \underset{\mathrm{b}}{\overset{\mathrm{a}}{\rightleftharpoons}} \mathrm{H_2CO_3}, \tag{22}$$

where the forward reaction (a) is governed by the rate constant k_a, and the reverse reaction (b) is governed by the rate constant k_b. Depending on the ocean pH, carbonic acid readily dissociates into $\mathrm{H^+}$ and bicarbonate in the following equilibrium reaction:

$$\mathrm{H_2CO_3} \underset{\mathrm{d}}{\overset{\mathrm{c}}{\rightleftharpoons}} \mathrm{H^+} + \mathrm{HCO_3^-}, \tag{23}$$

with k_c and k_d for the forward and reverse reactions, respectively. Finally, bicarbonate may further dissolve into $\mathrm{H^+}$ and a carbonate ion:

$$\mathrm{HCO_3^-} \underset{\mathrm{f}}{\overset{\mathrm{e}}{\rightleftharpoons}} \mathrm{H^+} + \mathrm{CO_3^{2-}}, \tag{24}$$

where k_e and k_f give the dissolution and combination rate constants, respectively.

As in E. W. Schwieterman et al. (2019b) and J. Krissansen-Totton et al. (2021), we assume that calcite is saturated, so that

$$[\mathrm{CO_3^{2-}}] = \frac{\Omega_{\mathrm{cal}} \times K_{\mathrm{sp}}(T_{\mathrm{surf}})}{[\mathrm{Ca^{2+}}]}, \tag{25}$$

where Ω_{cal} is the unitless global ocean calcite saturation factor, K_{sp} is the calcite solubility product, and $[\mathrm{Ca^{2+}}]$ is the concentration of calcite in the oceans in mol $\mathrm{kg^{-1}}$. To calculate solubility self-consistently with surface temperature, we use the temperature- and salinity-dependent solubility product formula given by F. J. Millero (2005). As in E. W. Schwieterman et al. (2019a), for all solubility parameterizations we assume that ocean salinity remains constant at 35 ppt. We also assume that the temperature of the ocean is equivalent to the global average surface temperature, as we assume that the ocean and atmosphere equilibrate faster than our model's geological timescales.

Using Equation (25), a saturation factor, and a calcite concentration, we can calculate the carbonate concentration in the ocean. E. W. Schwieterman et al. (2019a) assumed $\Omega_{\mathrm{cal}} = 1$, but calcite may need to be supersaturated ($\Omega_{\mathrm{cal}} \sim 10$–$20$) for abiotic precipitation to occur. Furthermore, over Earth's history, the calcite concentration has varied from $[\mathrm{Ca^{2+}}] = 10^{-2}$ to 3×10^{-1} mol $\mathrm{kg^{-1}}$ (I. Halevy & A. Bachan 2017). We therefore tune $\Omega_{\mathrm{cal}}/[\mathrm{Ca^{2+}}]$ to match the observed total DIC in the surface oceans for preindustrial conditions (see Table A1).

This tuning approach requires justification, as our model represents an Earth without oxygenic photosynthesis or complex skeletal organisms, analogous to conditions during the Archean and early Proterozoic eons. In the modern ocean, carbonate precipitation is predominantly biogenic (K. E. Chave & E. Suess 1970; O. M. Bialik et al. 2022), though O. M. Bialik et al. (2022) estimate that abiotic aragonite precipitation accounts for approximately 15% of $\mathrm{CO_2}$ efflux in oligotrophic regions where surface waters remain supersaturated with respect to calcium carbonate. However, evidence supports that abiotic carbonate precipitation processes, while kinetically slower than biogenic precipitation, can achieve similar steady-state DIC concentrations over geological timescales. Laboratory experiments show that abiotic calcite precipitates at rates 2–5 orders of magnitude slower than biotic calcite (S. J. Carpenter & K. C. Lohmann 1992), but given billion-year timescales, kinetic limitations become less constraining.

Furthermore, geological evidence supports widespread abiotic carbonate precipitation in Earth's early history. The Precambrian geological record shows extensive carbonate platform deposition (J. P. Grotzinger 1989; J. P. Grotzinger & J. F. Kasting 1993; J. P. Grotzinger & N. P. James 2000), including meter-thick beds of fibrous calcite and aragonite precipitated directly on the Archean seafloor (D. Y. Sumner & J. P. Grotzinger 1996). D. Y. Sumner & J. P. Grotzinger (1996) argued that high rates of abiotic precipitation in Archean oceans were facilitated by elevated $\mathrm{Fe^{2+}}$ concentrations in anoxic seawater, which paradoxically promoted aragonite precipitation while inhibiting calcite nucleation. This geological evidence demonstrates that abiotic processes can generate substantial carbonate deposits, supporting our assumption that calcite saturation is achievable without biology.

We find that the optimal $\Omega_{\mathrm{cal}}/[\mathrm{Ca^{2+}}]$ to match preindustrial DIC is 408.1 kg $\mathrm{mol^{-1}}$. Recent spatial mapping of global calcite saturation in present-day oceans shows an average $\Omega_{\mathrm{cal}} = 4.3$ (I. Shaik et al. 2025), and the present-day $[\mathrm{Ca^{2+}}]$ is 10.28 mmol $\mathrm{kg^{-1}}$ (I. Halevy & A. Bachan 2017),

corresponding to a present-day ratio of $\Omega_{\rm cal}/[{\rm Ca}^{2+}] = 398$. Conservatively estimating that a supersaturation factor of $\Omega_{\rm cal} = 20$ is required for abiotic carbonate precipitation, our calibrated $\Omega_{\rm cal}/[{\rm Ca}^{2+}]$ corresponds to a calcite concentration of 49 mmol kg^{-1}. We discuss the possible limitations of this tuning approach in Section 5.3.

We model this chemical system using the following equations adopted from M. E. Pilson (2012):

$$k_e = \frac{[{\rm H}^+][{\rm HCO}_3^-]}{({\rm CO}_2)_{\rm aq}} \tag{26}$$

and

$$k_f = \frac{[{\rm H}^+][{\rm CO}_3^{2-}]}{[{\rm HCO}_3^-]}. \tag{27}$$

Since $k_e/k_f = [{\rm HCO}_3^-]^2/([{\rm CO}_3^{2-}][{\rm CO}_2])$, we can combine these rate constant equations to solve for the concentration of bicarbonate:

$$[{\rm HCO}_3^-] = \sqrt{({\rm CO}_2)_{\rm aq}[{\rm CO}_3^{2-}] \times \frac{k_e}{k_f}}. \tag{28}$$

Finally, we can solve for the concentration of $[{\rm H}^+]$ by taking

$$[{\rm H}^+] = \frac{K_{\rm sp}[{\rm HCO}_3^-]}{[{\rm CO}_3^{2-}]}, \tag{29}$$

where ${\rm pH} = -\log_{10}[{\rm H}^+]$.

3.7. Surface Albedo

The surface albedo of the planet in our model consists of contributions from the ground and atmospheric water-vapor clouds. Based on previous work (P. Driscoll & D. Bercovici 2013), we simulate the evolving total planetary surface albedo $A_{\rm T}$ by allowing the ground albedo $A_{\rm g}$ and cloud fraction ϕ to vary with time, so that

$$A_{\rm T} = A_{\rm g}(1 - \phi) + A_{\rm cl}\,\phi. \tag{30}$$

We assume that our Earth-like water-vapor clouds have an albedo of $A_{\rm cl} = 0.89$, which represents an average albedo of thick and thin clouds (I. de Pater & J. Lissauer 2010; P. Driscoll & D. Bercovici 2013). We assume a constant fraction of the atmospheric H_2O reservoir condenses into clouds, and tune the wavelength-independent cloud opacity pressure to ensure we match the PIE surface temperature at 4.5 Gyr. As in P. Driscoll & D. Bercovici (2013), we then calculate the cloud reflectivity fraction using the two-stream Eddington approximation:

$$\phi = \frac{\gamma(1 - e^{-2\beta\tau_{\rm cl}})}{1 - \gamma^2 e^{-2\beta\tau_{\rm cl}}}, \tag{31}$$

with $\tau_{\rm cl} = 4800$ Pa as the constant cloud opacity pressure and scattering constants

$$\gamma = \frac{\beta - 2(1 - \bar{w})}{\beta + 2(1 - \bar{w})} \tag{32}$$

and

$$\beta = \sqrt{3(1 - \bar{w})(1 - \bar{w}g_w)}, \tag{33}$$

where $\bar{w}$ is the single-scattering albedo $1 - \bar{w} = 1 \times 10^{-7}$ and $g_w = 0.74$ is the asymmetry factor (G. L. Hashimoto & Y. Abe 2001). Given that this simplified cloud model cannot account for more complex effects like radiative heating due to clouds and wavelength-dependent reflectivity, we tune the cloud opacity pressure to match the PIE temperature. Thus, we will *not* attempt to match the PIE cloud fraction with the model.

The ground albedo $A_{\rm g}$ consists of contributions from surface rock ($x_{\rm r}$), ocean ($x_{\rm oc}$), and ice ($x_{\rm i}$) fractions, where

$$A_{\rm g} = x_{\rm r}A_{\rm r} + x_{\rm oc}A_{\rm oc} + x_{\rm i}A_{\rm i}. \tag{34}$$

We take the albedo of rock to be $A_{\rm r} = 0.17$ (L. Kaltenegger et al. 2007; P. Driscoll & D. Bercovici 2013), the albedo of ocean water to be $A_{\rm oc} = 0.1$ (I. de Pater & J. Lissauer 2010; P. Driscoll & D. Bercovici 2013), and the albedo of ice to be $A_{\rm i} = 0.6$ (L. Kaltenegger et al. 2007; P. Driscoll & D. Bercovici 2013). We assume a conical ocean basin as in P. Driscoll & D. Bercovici (2013), with a slope angle of $\theta_{\rm oc} = 0.^{\circ}06188$ calibrated to give $x_{\rm oc} = 0.71$ when $w_{\rm ocean} = 1.4 \times 10^{21}$ kg. To model ice growth, we include the simple relation from P. Driscoll & D. Bercovici (2013), which gives $x_{\rm i} = x_{\rm i,max} \times (1 - x_{\rm oc}) \times (x_{\rm oc}/x_{\rm oc,0})$, where $x_{\rm i,max} = 0.12$ is the maximum ice fraction, $(1 - x_{\rm oc})$ is the fraction of land, and $x_{\rm oc,0}$ is the present-day ocean fraction of 0.71.

Previous work has established that habitability requires only some amount of liquid water on the planetary surface (J. F. Kasting et al. 1993), and that global average surface temperatures can be meaningfully compared to spatially resolved 3D climate states when assessing habitability thresholds (B. Charnay et al. 2013; G. Arney et al. 2016). B. Charnay et al. (2013) demonstrated through 3D general circulation modeling that complete glaciation (e.g., a "snowball" Earth) likely does not occur until global average surface temperatures fall below 240 K, owing to spatial heterogeneity in ice coverage and meridional heat transport that maintains liquid-water reservoirs at the equator. We therefore allow $x_{\rm i} = 1.0$ when the global average surface temperature is $\leqslant$240 K, though like P. Driscoll & D. Bercovici (2013) our model does not currently handle transitions between global glaciation phases and $x_{\rm i,max}$.

3.8. Climate

Planetary surface temperature is related to surface and atmospheric characteristics, as well as the radiation received from the star. We determine surface temperature by calculating thermal equilibrium between the ASR and the OLR. OLR is a function of surface temperature and the atmospheric abundances of water vapor and CO_2, while ASR is additionally a function of the total albedo, incoming stellar flux, and effective stellar temperature.

To calculate ASR and OLR, we use the `Clima` module of the `Photochem` software package (N. F. Wogan et al. 2025b). `Clima` uses standard two-stream methods (O. B. Toon et al. 1989) to solve the radiative-transfer equations, incorporating opacity tables to simulate continuum UV absorption, Rayleigh scattering, and collision-induced absorption (CIA), while accounting for line absorption with the correlated-k method. This approach explicitly captures the wavelength-dependent absorption and scattering processes that gray atmosphere models cannot. `Clima` has been benchmarked against other community radiative-transfer codes, including SOCRATES

(E. T. Wolf et al. 2022), ExoRT (E. T. Wolf et al. 2022), SMART (V. S. Meadows & D. Crisp 1996), and the radiative-transfer code used by R. K. Kopparapu et al. (2013), demonstrating good agreement across a range of atmospheric compositions and stellar spectra. Furthermore, the code reproduces the observed pressure–temperature profiles of Venus, Earth, Mars, Jupiter, and Titan (N. F. Wogan et al. 2025b).

To resolve 1D atmospheric structure, we use the mode of `Clima` that assumes an isothermal stratosphere above a convective troposphere with a pseudo-moist adiabat. The stratospheric temperature is estimated via the skin temperature for an assumed Bond albedo, A_B. As in any 1D climate model, `Clima` has a limited ability to self-consistently calculate the radiative impact of clouds. As a result, we follow previous work (e.g., R. K. Kopparapu et al. 2013) and "paint" them onto the surface by incorporating them into the total surface albedo, which is an input to the radiative-transfer calculation (see Section 3.7).

Using the stellar evolution module in `VPLanet` (I. Baraffe et al. 2015), we calculate the evolving incoming stellar flux ($F_\star$) and temperature ($T_\star$) as a function of time. To determine the top-of-atmosphere (TOA) solar flux, `Clima` calculates a blackbody distribution corresponding to $T_\star$. This ensures that ASR accounts for how the evolving Sun impacts wavelength-dependent atmospheric opacity. Rather than calling the full radiative-transfer calculation at every time step, which would be computationally prohibitive for billion-year integrations, we precompute a grid of OLR and ASR values as functions of surface temperature, atmospheric CO_2 partial pressure, total H_2O surface inventory, stellar flux, stellar effective temperature, and surface albedo.

The grid spans surface temperatures from 100 to 500 K (41 points, spaced at 10 K intervals), CO_2 partial pressures from 10^{-6} to 10^4 bar (21 points, logarithmically spaced at 0.5 dex intervals), H_2O total surface pressures from 10^{-3} to 10^4 bars (15 points, logarithmically spaced at 0.5 dex intervals), stellar fluxes from 800 to 2000 W m^{-2} (13 points, spaced at 100 W m^{-2} intervals), surface albedos of 0.0, 0.1, 0.3, 0.5, 0.7, and 0.9 (six discrete values), and stellar effective temperatures from 5000 to 6000 K (five points, spaced at 250 K intervals). At each model time step, we pass the current values of T_{surf}, pCO_2, total surface water inventory (in bars), stellar flux ($F_\star$), A_T, and stellar effective temperature ($T_\star$) to a multidimensional linear interpolation routine that returns the corresponding OLR and ASR from the precomputed grid. The complete grid contains approximately 9.7 million precomputed atmospheric states.

We then use Brent's method (R. P. Brent 2013) to iteratively solve for the equilibrium surface temperature at which ASR equals OLR, using a bracket of [100, 600] K and a tolerance of 2×10^{-12}. Once convergence is achieved, we pass the solved T_{surf} back to `VPLanet` to update all temperature-dependent parameters. This grid-based approach maintains the approximate accuracy of full radiative-transfer calculations ($<\sim$1 K error) while reducing computational cost by approximately 3 orders of magnitude, enabling efficient exploration of long-term planetary evolution.

In `Clima`, we parameterize the H_2O inventory as a pressure column (in bars) representing the total surface water reservoir (w_{surf} converted to an equivalent pressure). `Clima` internally partitions the combined surface reservoir between atmospheric vapor (limited by saturation vapor pressure at each vertical level) and condensed phases, capturing the coupled radiative–thermodynamic effects of water-vapor feedback. Once a steady-state climate is computed, we extract the atmospheric composition using `Clima`'s vertically resolved solution. We extract the surface water-vapor mixing ratio and the total surface pressure from the interpolated grid output, which represent `Clima`'s self-consistent partitioning of water between the atmosphere and ocean when accounting for temperature stratification throughout the atmospheric column. This more physically accurate partitioning refines our initial surface-only estimates described in Sections 3.5. We recalculate w_{atm}, w_{ocean}, c_{atm}, and c_{ocean} to match `Clima`'s atmospheric state, ensuring that the water distribution used in subsequent carbon-cycle and thermal evolution calculations remains consistent with the radiative-transfer solution.

3.9. Reflected-light Spectra

We use the `PICASO` code (N. E. Batalha et al. 2019) to compute synthetic HWO reflected-light spectra (0.2–2.0 μm) for the true Earth and the abiotic Earth's atmospheric state after 4.5 Gyr. We use a set of $R = 15{,}000$ resampled opacities archived on Zenodo (N. Wogan et al. 2025a), derived from a similar set of HITEMP (L. S. Rothman et al. 2010) and HITRAN (I. E. Gordon et al. 2017) opacities used by `Clima` for climate calculations (Section 3.8). The opacity database accounts for line absorption from the following relevant species: CO_2, H_2O, O_2, O_3, and CH_4. Relevant CIA partners include CO_2–CO_2, H_2O–H_2O, H_2O–N_2, N_2–N_2, N_2–O_2, and O_2–O_2. `PICASO` also includes Rayleigh scattering for all specified molecules.

We compute two reflected-light spectra: (1) a realistic modern Earth spectrum using temperature and mixing-ratio profiles from the Intercomparison of Radiation Codes in Climate Models (ICRCCM) case 62, which represents the averaged midlatitude Earth during the summer months (A. P. Lincowski et al. 2018), and (2) an abiotic Earth spectrum using the `VPLanet` atmospheric state after 4.5 Gyr, which includes only CO_2 and H_2O as greenhouse gases along with 1 bar of N_2. For both spectra, we input an expected surface albedo of 0.14 (without clouds) and include a cloud deck. We model clouds as a single gray deck extending from 0.6 to 0.7 bar with an optical depth of 10, a single-scattering albedo of 0.99, and an asymmetry parameter of 0.85. We compute both cloudy and cloud-free spectra and weight them by a cloud fraction of 50% to approximate Earth's observed cloud coverage. Both calculations assume solar illumination at quadrature (90° phase angle) and are binned to $R = 140$.

The ICRCCM Earth reference profile has been reinterpolated onto the `VPLanet` pressure grid to enable direct comparison. The `VPLanet` grid has a surface pressure of 1.016 bars compared to the ICRCCM value of 0.989 bar, representing a difference of approximately 0.03 bar, or 3% higher surface pressure. The TOA extends to 1.1×10^{-5} bar in the `VPLanet` grid versus 1×10^{-7} bar in the original ICRCCM profile. The number of atmospheric layers differs, as well, with 51 layers in the `VPLanet` grid compared to 63 layers in the original ICRCCM profile. These differences are minor—the 3% surface pressure difference causes negligible changes in atmospheric column density, and the higher TOA cutoff removes only the uppermost stratosphere and mesosphere, which are optically thin and contribute minimally to

Table 2
Initial Conditions and Constants of the Interior Earth Model

Parameter	Value
Initial ^{40}K power in the mantle	5.14×10^{13} W
Initial ^{40}K power in the core	4.05×10^{13} W
Initial ^{232}Th power in the mantle	7.01×10^{12} W
Initial ^{232}Th power in the core	1.30×10^{11} W
Initial ^{238}U power in the mantle	1.04×10^{13} W
Initial ^{238}U power in the core	1.0×10^{11} W
Initial ^{235}U power in the mantle	1.66×10^{13} W
Initial ^{235}U power in the core	4.68×10^{11} W
Initial mantle temperature	2700 K
Initial core temperature	5700 K
Melt eruption efficiency	0.01 [n.d.]
Core liquidus depression	4.04×10^{-4} K
Lower-/upper-mantle viscosity ratio	1.487 [n.d.]
Depression of mantle viscosity activation energy due to water	9.642×10^{6} K
Viscosity activation energy	2.64×10^{5} J mol^{-1}
Upper-mantle thermal conductivity	4.24 W/m/K

Note. Core radiogenic power includes BMO contribution (see Section 3.2).

the spectrum. The temperature–pressure profile, water-vapor distribution, and other trace-gas abundances have been linearly interpolated in log–pressure space to preserve the atmospheric structure of the original ICRCCM profile.

3.10. Initial Conditions

Our model requires the initialization of key parameters, including those describing the initial conditions of the interior and the surface volatile inventories. Here, we briefly describe how we initialized our model at 50 Myr, i.e., following the magma ocean phase. Most other initial values are calibrated to match the relevant measurements of the PIE. Though the model evolution is largely insensitive to the initial CO_2 and H_2O inventories, we base the total initial masses of volatiles on previous work.

To compute a plausible evolutionary model for Earth, we optimized 16 initial conditions and constants of the interior (given in Table 2) to reproduce Earth's present-day interior properties (given in Table 1). To perform the optimization, we assumed a Gaussian likelihood function based on the mean and uncertainty of each output parameter, and minimized the negative log-likelihood using the Nelder–Mead simplex algorithm (J. A. Nelder & R. Mead 1965) implemented in `SciPy` (E. Jones et al. 2001). Due to the multimodal nature of likelihood space, we initialized the optimization at 200 different starting locations uniformly sampled over a wide parameter range and selected the maximum-likelihood fit out of all runs that converged.

As in J. Seales & A. Lenardic (2020), we initialize our model with 2 TOs of water. From N. H. Sleep & K. Zahnle (2001), we assume that Earth's total initial CO_2 inventory is 1.1×10^{21} kg. Initially, to partition the volatiles between the interior and surface reservoirs, we follow estimations of the primordial Earth atmosphere immediately following the solidification of the magma ocean. L. T. Elkins-Tanton (2008) predicts primordial Earth CO_2–H_2O atmospheres ranging from 90 to 3350 bars. Consistent with the lower end of these model estimates, we initialize the surface with 5 bars of CO_2 and 530 bars of H_2O (2 TOs) for a combined primordial atmosphere of 535 bars.

Though the magma ocean phase may conclude with a higher surface inventory of CO_2, through initial model testing we found that the pCO_2 evolution is largely independent of the initial atmospheric carbon inventory. This model behavior occurs because our seafloor weathering flux (Equation (9)) is assumed to be directly dependent on plate speed and pCO_2 relative to the present day, which may be very large immediately following the magma ocean phase, though primordial Earth conditions remain uncertain. As a result, basaltic seafloor weathering is found to be efficient enough to draw nearly all of the CO_2 out of the atmosphere. Therefore, we initialize the model with 5 bars to maximize model stability —all CO_2 reservoirs must initially contain nonzero mass, and the remaining CO_2 is split between the plate and the mantle.

In summary, our model couples interior thermal evolution (`ThermInt`, `RadHeat`), volatile cycling (carbon and water), ocean chemistry, and climate (`Clima`) into a unified framework. We track CO_2 and H_2O masses across mantle, ocean, and atmospheric reservoirs with fluxes controlled by plate tectonics and weathering. Key model features include a radiogenically enriched BMO, water-dependent mantle viscosity, calcite-saturated ocean chemistry, and evolving planetary surface albedo from ground and cloud contributions. We initialize the model as described above, then evolve the system forward 4.5 Gyr to match PIE properties.

4. Results

In this section, we show that the whole-planet model successfully reproduces the PIE after 4.5 Gyr of model evolution. We also generate a corresponding reflected-light spectrum to compare against that of a realistic, cloudy Earth. In Table 2, we report the calibrated interior parameter values following our optimization procedure described in Section 3.10, and the model results and comparison to measured values within uncertainties are summarized in Table 3.

In Figure 3, we show the incoming solar flux at the planet as a function of time. Using the I. Baraffe et al. (2015) model, the evolving solar flux starts at 943 W m^{-2} ($\sim$0.7 $L_\odot$) and reaches 1370 W m^{-2} (1.0 $L_\odot$) by 4.5 Gyr. The final incoming stellar flux is thus consistent with its present-day value. Furthermore, the early stellar flux is consistent with predictions of other stellar evolution models used to model the faint young Sun (C. Sagan & G. Mullen 1972; M. J. Newman & R. T. Rood 1977; D. Gough 1981).

Figure 4 shows the evolution of bulk planetary parameters, including surface temperature, total albedo (ground and clouds), atmospheric pH_2O, and atmospheric pCO_2. By 4.5 Gyr, the planetary surface temperature reaches 286.9 K (a), the ground albedo (solid line) is 0.14, while the total albedo including clouds (dashed line) is 0.198 (b), the atmospheric pH_2O is 1600 Pa with an assumed relative humidity of 100% (c), and the atmospheric pCO_2 is 28.2 Pa (d). The atmospheric water-vapor abundance (c) shows a strong relationship with planetary temperature (a) due to the efficiency of OLR absorption and strong temperature dependence of saturation vapor pressure. After 4.5 Gyr, our model suggests that the total degassing flux of CO_2 is 9 Tmol yr^{-1} and that of H_2O is 85 Tmol yr^{-1}—both are reasonably close to

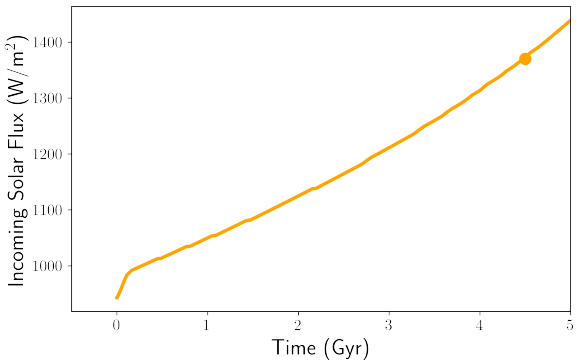


Figure 3. Incoming solar flux evolution with time, where the dot at 4.5 Gyr represents the present-day value.

Table 3
Abiotic Earth Model Values Compared to Preindustrial Earth Measurements

Properties	Target Value	Model Value
Atmospheric CO_2 ($p\,CO_2$)	28.4 ± 0.4 Pa	28.2 Pa
Atmospheric H_2O ($p\,H_2O$)	900 ± 700 Pa	1600 Pa
Surface temperature (T_{surf})	286.9 ± 0.1 K	286.9 K
Ground albedo (A_g)	0.14	0.14
Ocean mass (w_{ocean})	1.4×10^{21} kg	1.4×10^{21} kg
Oceanic (CO_2)aq	8 ± 2 μmol kg^{-1}	10.8 μmol kg^{-1}
Total dissolved inorganic carbon (DIC)	2000 ± 200 μmol kg^{-1}	1919 μmol kg^{-1}
pH	8.18 ± 0.05	8.28
Upper-mantle temperature (T_{UM})	1587^{+161}_{-34} K	1561 K
Core–mantle boundary temperature (T_{CMB})	4000 ± 200 K	3889 K
Upper-mantle heat flow (Q_{UM})	38 ± 3 TW	38 TW
Core–mantle boundary heat flow (Q_{CMB})	11 ± 6 TW	15 TW
Upper TBL viscosity (ν_{UM})	$10^{17.38\pm1}$ m^2 s^{-1}	$10^{17.46}$ m^2 s^{-1}
Lower TBL viscosity (ν_{LM})	$10^{17.28\pm1}$ m^2 s^{-1}	$10^{17.73}$ m^2 s^{-1}
Upper-mantle melt fraction (F_{UM})	11.5 ± 3.5%	10.0%
Melt flux	$(1.3 \pm 0.8) \times 10^6$ kg s^{-1}	1.9×10^6 kg s^{-1}
Inner-core radius (R_{IC})	1221 ± 1 km	1221 km
Magnetic moment	1.00 ± 0.05 E. Unit	1.01 E. Unit
Magnetopause radius	1.00 ± 0.02 E. Unit	1.00 E. Unit

Note. Model values are reported at 4.5 Gyr.
All measured values and uncertainties are detailed in Section 2 and summarized in Table 1.

the present-day observations of 7.5 and 95 Tmol yr^{-1}, respectively (D. C. Catling & J. F. Kasting 2017).

At the start of the evolution, following a brief (∼100 Myr) equilibration period, the planet is relatively warm, with $T_{surf} = 297$ K. The degassing flux dominates, allowing the atmospheric CO_2 abundance to rise to ∼1 bar 100,000 yr after model initialization. As the planet warms, weathering is enhanced and the carbon sinks begin to overwhelm the sources, resulting in a gradual decrease in pCO_2. Initial oscillations in CO_2 (<5 Myr) occur due to a disequilibrium between CO_2 partitioning and the rapidly cooling mantle and surface temperatures. The final state of the model is ultimately insensitive to these initial model conditions. Furthermore, the transition between magma ocean solidification and the onset of plate tectonics is poorly understood, so modeling this transition falls outside the scope of this work.

The total albedo includes contributions from the ground and clouds, and is therefore higher. Clouds are tuned to match the PIE temperature. From tuning the constant cloud opacity pressure, we find a total albedo of 0.198, corresponding to a cloud fraction of 8%. We note that this is likely an unrealistically small cloud fraction for the PIE, most likely due to our simplified cloud implementation (see Section 5.6).

Figure 5 shows the evolution of the surface and mantle water budgets (a), the aqueous CO_2 concentration (b), ocean pH (c), and the surface ocean's total DIC concentration (d). We initialize the surface with 2 TOs, resulting in 1 TO in the mantle after 4.5 Gyr. Using Henry's law, we calculate an aqueous CO_2 concentration of 10.8 μmol kg^{-1} by 4.5 Gyr (b). Assuming a constant carbonate concentration based on the abiotic calcite budget, we obtain a pH of 8.28 after 4.5 Gyr (c). Finally, the total DIC at the ocean surface is 1919 μmol kg^{-1} after 4.5 Gyr (d). Ocean pH exhibits strong temperature-dependent behavior, while the DIC evolution tracks closely with the atmospheric CO_2 evolution. When the atmospheric CO_2 abundance is initially high (Figure 4(d)), the aqueous CO_2 concentration is also high (Figure 4(b)). Following model equilibration, as atmospheric CO_2 abundance sharply increases prior to 1 Gyr, the aqueous CO_2 concentration rises to 2×10^{-2} mol kg^{-1}, and the ocean pH is ∼6.6, or 30× more acidic than present-day Earth oceans. As the atmospheric CO_2 content gradually wanes to PIE values, the aqueous CO_2 concentration and DIC follow suit, resulting in increasingly alkaline oceans.

Figure 6 shows the evolution of the mantle. In Figure 6(a), we show the evolution of the average temperature of the mantle (T_M), the evolving upper-mantle temperature T_{UM}, and the evolving lower-mantle temperature T_{LM}. In panel (b) of the same figure, we show the evolution of heat flow in the upper mantle (Q_{UM}) and the radiogenic heat flow in the mantle ($Q_{rad,M}$). Panel (c) shows the changing boundary-layer depths of the upper (δ_{UM}) and lower mantle (δ_{LM}). Note that the thickness of the assumed BMO always remains smaller than the thickness of the lower boundary layer (<60–100 km), preventing the radiogenically enriched BMO from mixing into the convecting mantle. Panel (d) shows the viscosity near the upper TBL (ν_{UM}) and near the lower TBL of the mantle (ν_{LM}) with time. Finally, panel (e) shows the upper-mantle melt fraction, and panel (f) shows the melt mass flux over geological time. By 4.5 Gyr, we confirm that T_{UM}, Q_{UM}, ν_{UM}, ν_{LM}, F_{melt}, and the mantle melt mass flux all match measured Earth properties within measurement uncertainties.

In Figure 7, we show the evolution of key core properties over time. Panel (a) shows the evolution of the core–mantle boundary (T_{CMB}) and core (T_C) temperatures, while panel (b) shows the evolution of the heat flow at the CMB and the heat flow in the core due to radiogenics ($Q_{rad,C}$). Panel (c) shows the radius of the inner core with time, and panel (d) shows the core buoyancy flux. Finally, panel (e) shows the magnetic moment in Earth units, and panel (f) shows the magnetopause radius in Earth units.

For all properties shown in this figure, we note a discontinuity that occurs at ∼4 Gyr. This feature represents inner-core nucleation in the model, when light elements begin to be rejected from the solidifying inner core (P. Driscoll & D. Bercovici 2014). The thermal buoyancy flux of the core

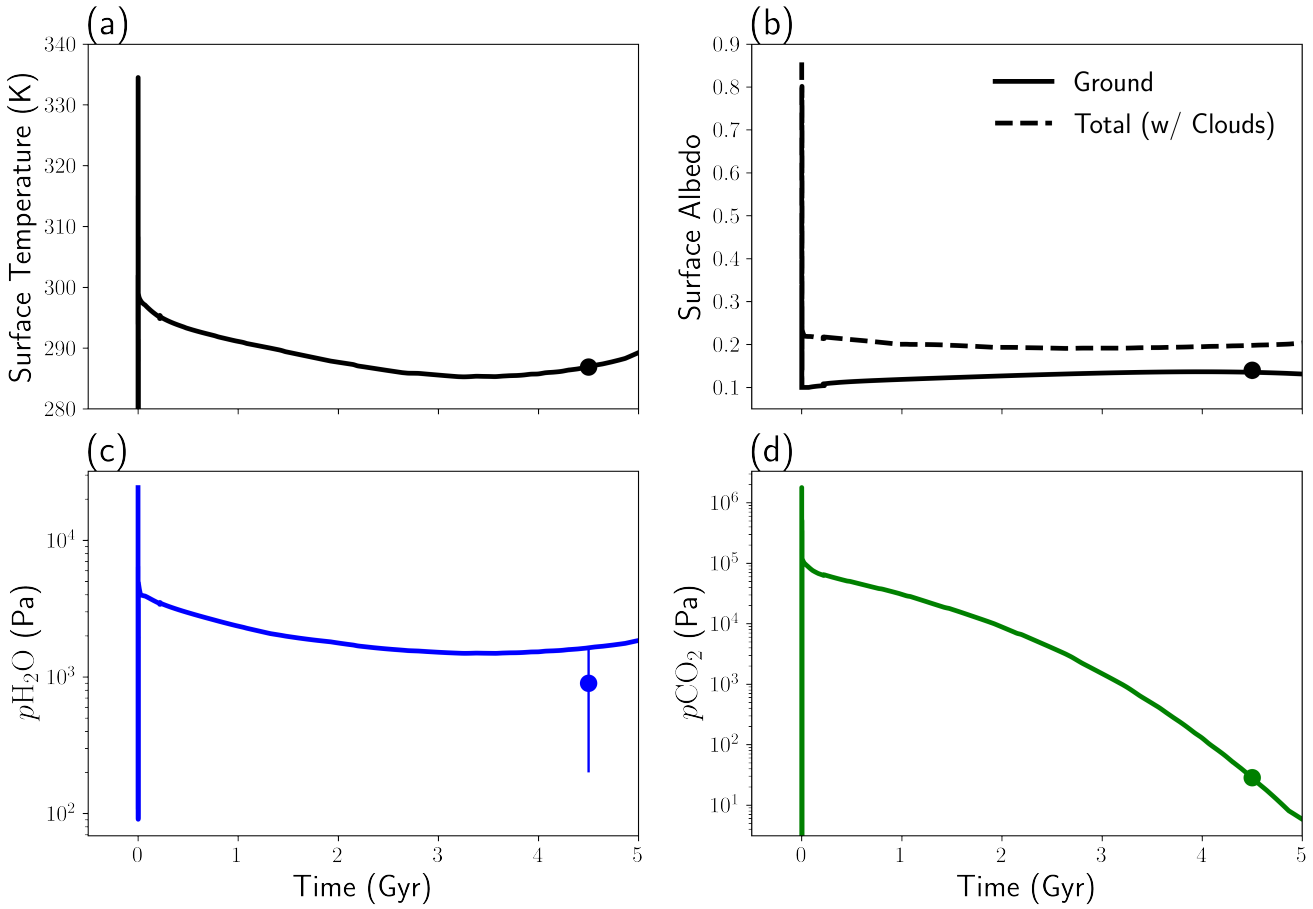


Figure 4. Some bulk properties of the abiotic Earth as a function of time. (a) The global average surface temperature warms as the star gradually brightens. (b) The ground albedo increases as dark ocean water subducts into the mantle and comparatively brighter land becomes exposed. The total albedo also increases as the warming planet's atmosphere can hold more water vapor and more clouds form. (c) As the planet warms, the atmosphere can hold more water and the H_2O partial pressure increases. (d) Finally, atmospheric CO_2 spikes early on when the planet is cold, and gradually decreases as weathering becomes more efficient on the warming planet. On all plots, dots represent measurements of PIE (4.5 Gyr) properties with uncertainties.

gradually decreases as the core cools (d). Once the inner core begins to solidify, light elements are injected into the base of the liquid outer core, generating compositional buoyancy and boosting the total core buoyancy flux (d). This buoyancy injection into the outer core boosts the magnetic moment and magnetopause radius (panels (e) and (f)). All core-related properties in Figure 7 match the final expected values within measurement uncertainties.

Table 3 summarizes our final model values for 19 preindustrial characteristics. For 17 out of 19 key parameters, our model results are within the reported measurement uncertainties, while oceanic $(CO_2)_{aq}$ and ocean pH fall slightly outside the measurement uncertainties. Our modeled $(CO_2)_{aq}$ of 10.8 μmol kg^{-1} slightly exceeds the measured range of 8 $\pm$ 2 μmol kg^{-1}, while our modeled ocean pH of 8.28 is marginally more alkaline than the measured value of 8.18 $\pm$ 0.05 (an offset of 0.10 pH units, or roughly twice the reported measurement uncertainty). Assuming the symmetric uncertainties of these measurements represent normal underlying distributions, our model is no more than 2σ offset from the mean measurements, and we take this to indicate sufficient model agreement. Nonetheless, this slight deviation from expectations for both ocean pH and $(CO_2)_{aq}$ can likely be attributed to our simplifying assumptions regarding calcite concentration. We discuss the implications of this assumption in Section 5.3.

Finally, as a proof of concept, in Figure 8 we compare reflected-light spectra of a realistic, cloudy Earth and a snapshot of the abiotic Earth after 4.5 Gyr (a), as well as their corresponding abundance profiles (b). Volume-mixing-ratio profiles are shown in log–log space as a function of decreasing pressure, with pressure in bars on the y-axis. While both atmospheres include CO_2, H_2O, and N_2, the abiotic atmosphere lacks O_2 (and therefore O_3) and CH_4. The lack of O_2 and O_3 contributes to the most significant differences in absorption between the two spectra. For example, in the near-UV at $\sim$0.25 μm, the true Earth spectrum shows absorption due to the O_3 Hartley band. In the visible, the Earth spectrum has absorption features at $\sim$0.6 μm due to the O_3 Chappuis band, and a prominent narrowband feature at $\sim$0.76 μm due to the O_2 *A* band. In the near-IR, the Earth spectrum shows absorption at $\sim$1.27 μm due to the weak O_2 feature. Finally, the true Earth spectrum has $\sim$2 ppm of CH_4, which produces an absorption feature at $\sim$1.69 μm in the near-IR, resulting in a relatively weak absorption feature that our abiotic planet lacks.

Figure 8(b) demonstrates some minor differences between the N_2, CO_2, and H_2O profiles. While the ICRCCM atmosphere is 79% N_2, the abiotic atmosphere has 1 bar to compensate for the lack of bulk O_2. Furthermore, the ICRCCM

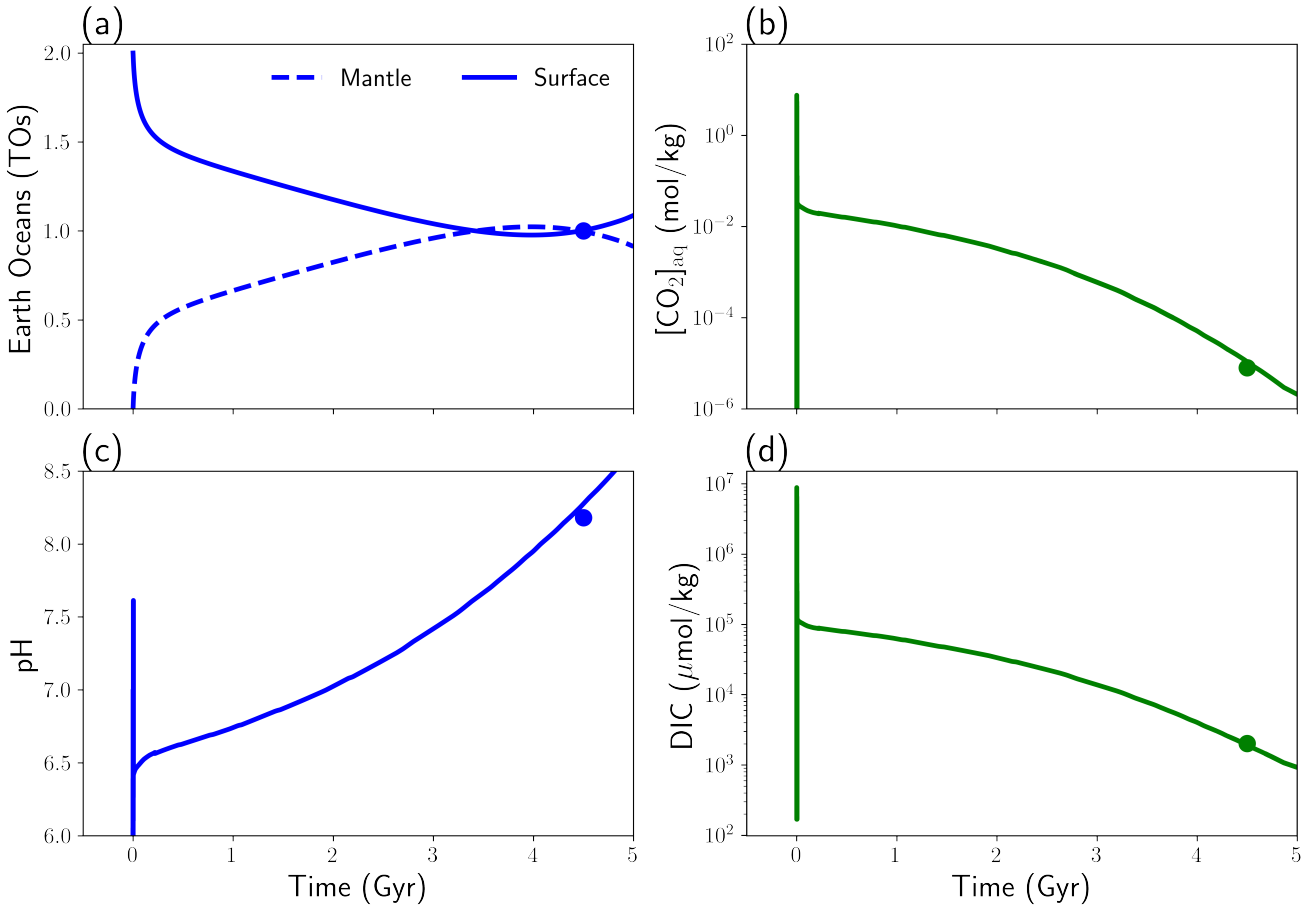


Figure 5. Properties of the ocean as a function of time. (a) After 4.5 Gyr, 1 TO has entered the mantle, ultimately leaving 1 TO on the surface. (b) The concentration of CO_2 in the oceans tracks closely with the atmospheric CO_2 inventory, following Henry's law. (c) Prior to equilibration, the pH initially spikes because the initial concentrations of carbonate and bicarbonate in the calcite-saturated oceans are also very high. Following equilibration, the pH gradually becomes more alkaline as the abundance of CO_2 in the atmosphere and ocean gradually decreases. (d) The total DIC at the ocean surface, which includes aqueous CO_2, carbonate, and bicarbonate, tracks closely with the atmospheric CO_2 budget. On all plots, dots represent measurements of PIE (4.5 Gyr) properties with uncertainties.

atmosphere was benchmarked to more recent terrestrial atmospheric abundances. As a result, the ICRCCM atmosphere has a higher CO_2 abundance of 330 ppm versus our 280 ppm. Lastly, though both water-vapor profiles have similar near-surface abundances, our tropopause appears at a slightly lower pressure (and higher altitude) than the ICRCCM profile. This difference occurs for two reasons. First, the ICRCCM profile represents an average midlatitude climate during the summer months, whereas our profile represents a globally averaged profile. Second, `Clima` estimates the location of the tropopause by calculating the atmospheric skin temperature rather than explicitly calculating the radiative–convective boundary. Nonetheless, these differences in the atmospheric profiles do not contribute to major differences in the resulting spectra—the weak CO_2 bands are insensitive to small differences in abundance, and most spectral water-vapor absorption occurs below the tropopause.

5. Discussion

We have presented a coupled core–mantle–crust–climate evolution model that reproduces 19 properties of the PIE within estimated measurement uncertainties, with two ocean chemistry parameters showing modest offsets attributable to our simplified treatment of calcite saturation. We have also shown that our model can be used to generate synthetic HWO-like reflected-light spectra. Our findings suggest that the abiotic Earth could evolve to a similar state (in terms of global geophysics and climate) to present-day Earth without life, but without abundant atmospheric oxygen. In this section, we discuss the implications of key assumptions in our model, such as neglecting CH_4 and abiotic calcite saturation in the oceans. Finally, we discuss our findings in the context of the Gaia hypothesis and forecast future research directions.

5.1. Spectroscopic Predictions for HWO Observations

The atmospheric states produced by our coupled evolution model can generate realistic reflected-light spectra suitable for comparison with future HWO observations (see Figure 8). The most significant spectral differences arise from the absence of biologically mediated gases: The modern Earth spectrum exhibits strong absorption features from O_2, O_3, and CH_4, none of which appear in our abiotic atmosphere.

This comparison validates that our model produces realistic atmospheric states that can be propagated through radiative-transfer codes to generate synthetic HWO observations. The abiotic spectrum represents the expected appearance of a habitable but lifeless Earth-like planet, establishing a null hypothesis against which to test biosignature detections. While both spectra show prominent H_2O and CO_2 features, only the biological Earth exhibits the O_2 (or O_3)/CH_4 disequilibrium

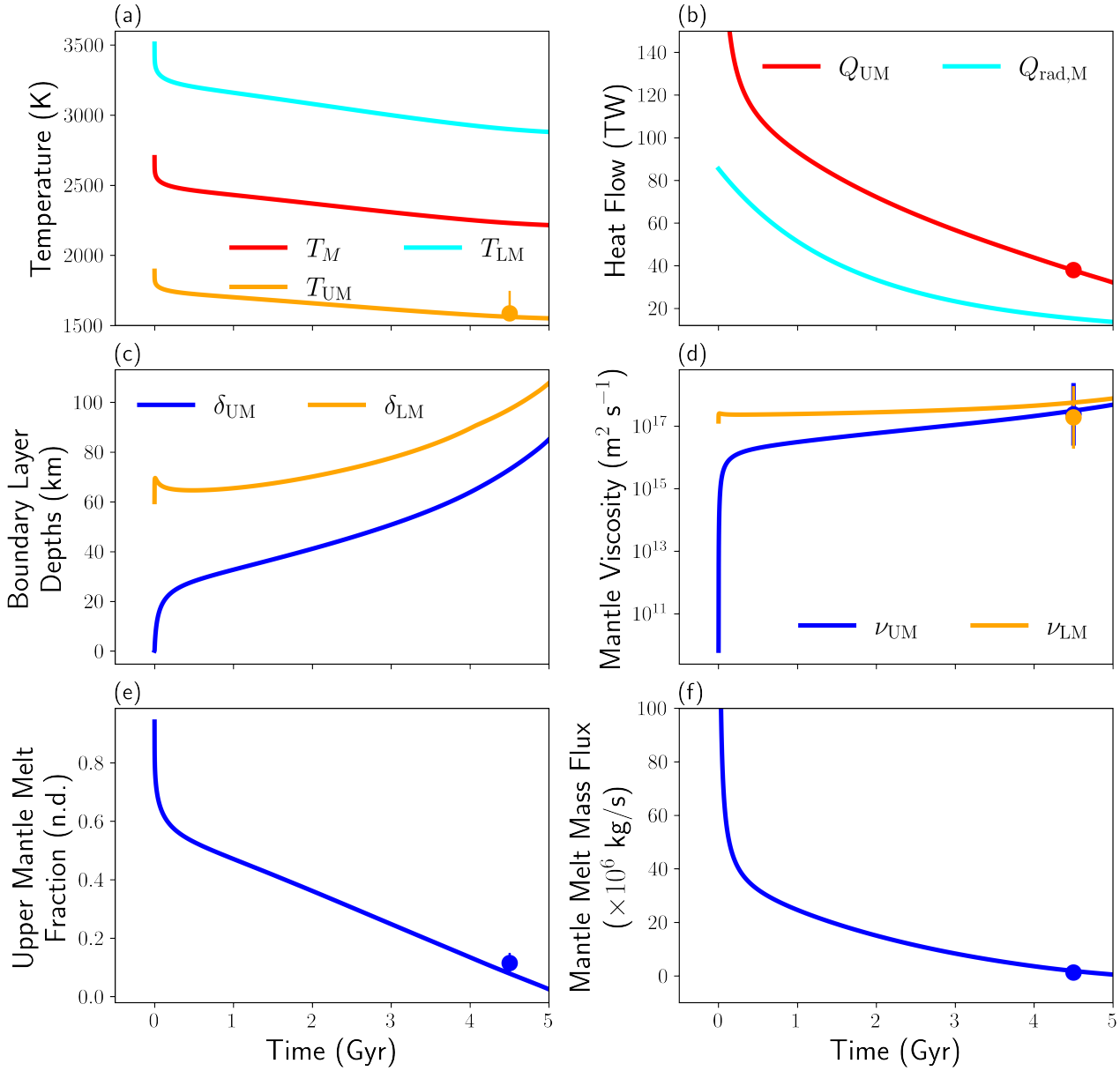


Figure 6. Key properties of the Earth's mantle through time. (a) The mantle and core gradually cool over time. (b) As the core and mantle cool, the heat flow across the upper mantle and the CMB and the heat flow due to radiogenics in the core and mantle decrease. (c) Both the upper- and lower-mantle boundaries grow deeper as the core–mantle system cools and the mantle solidifies downward. (d) The lower-mantle TBL is initially less viscous than the upper-mantle TBL. As water subducts into the cooling mantle, both the upper- and lower-mantle viscosities gradually increase. (e) As the interior cools, the upper-mantle melt fraction rapidly decreases. (f) Similarly, the melt flux from the mantle also decreases as the mantle cools. On all plots where applicable, dots represent measurements of PIE (4.5 Gyr) properties with uncertainties.

signature that would constitute compelling evidence for modern Earth-like life (V. S. Meadows et al. 2018). Future parameter-space explorations varying planetary properties and host-star types will reveal the diversity of reflected-light spectra representing abiotic habitable worlds, establishing the range of null-hypothesis scenarios that HWO must discriminate from life.

5.2. CH_4 as a Greenhouse Gas

Our model establishes that the carbonate–silicate cycle can operate effectively to maintain habitable surface temperatures over geological timescales using only CO_2 and H_2O as greenhouse agents, without requiring additional radiative forcing from trace gases like CH_4. This finding has important implications for understanding both Earth's climate history and the potential habitability of rocky exoplanets.

Abundant atmospheric CH_4 due to microbial life on the early Earth has been proposed as a solution to the faint young Sun paradox (A. A. Pavlov et al. 2000; P. Kharecha et al. 2005). A. A. Pavlov et al. (2000) showed that atmospheric CH_4 mixing ratios of 100–1000 ppmv, combined with elevated CO_2 levels, could maintain above-freezing temperatures despite 20%–30% lower solar luminosity. While biological fluxes of CH_4 may have warmed Earth's climate in certain epochs—with some models suggesting temperature increases of 5°C–10°C from elevated methane during the Archean (A. L. Roberson et al. 2011)—our results suggest that such

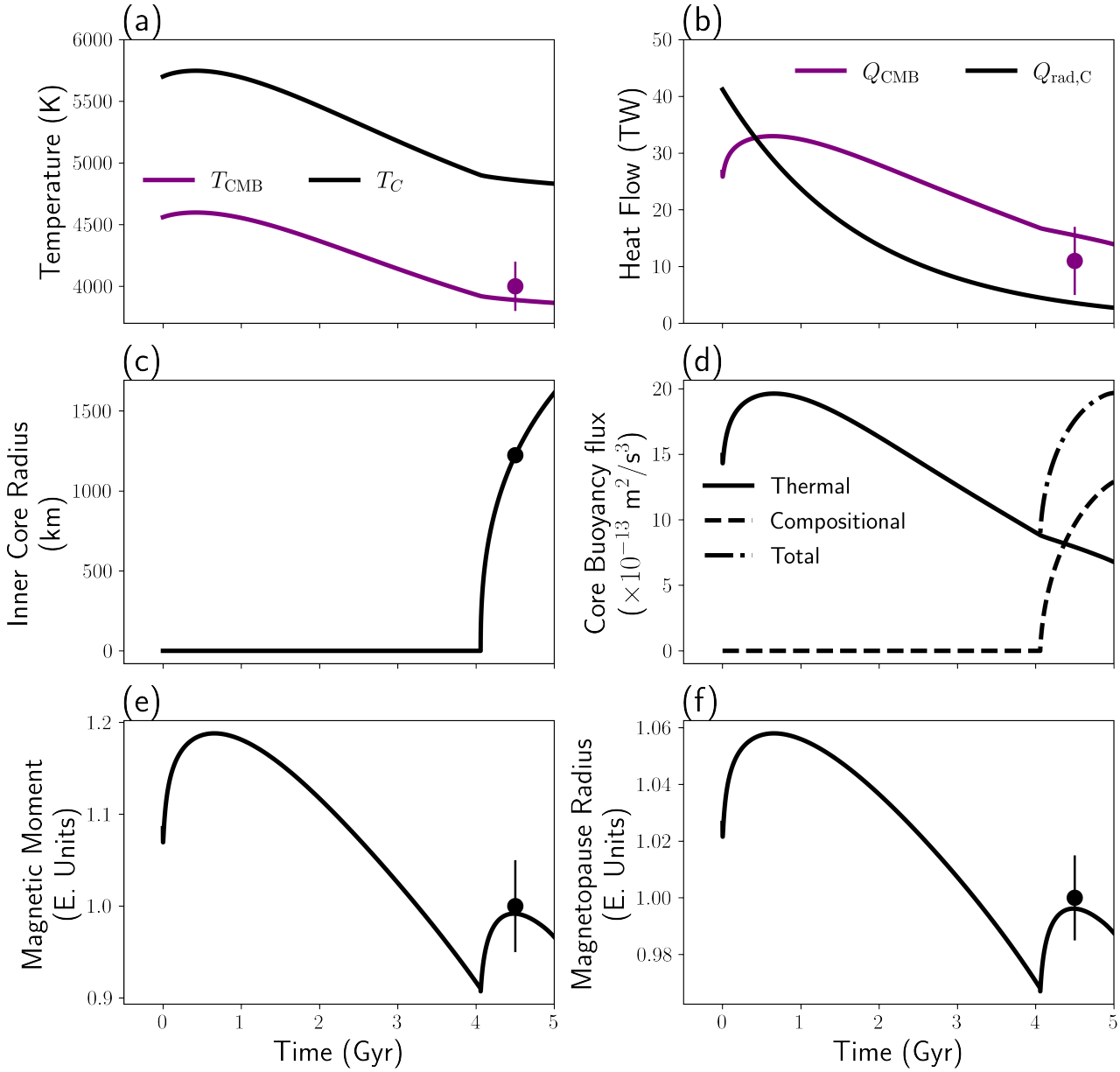


Figure 7. Key properties of the Earth's core through time. (a) and (b) The temperature and heat flows of the core and CMB secularly decrease with time. (c) Once the interior has sufficiently cooled, the inner core rapidly solidifies at ∼4 Gyr. (d) The thermal buoyancy flux of the core gradually decreases as the core cools. Once the inner core solidifies and exsolves light elements, the compositional changes inject energy into the outer core and boost the overall core buoyancy flux. (e) and (f) The late energy increase in the outer core due to inner-core solidification causes coinciding discontinuities in the magnetic moment and the magnetopause radius. On all plots where applicable, dots represent measurements of PIE (4.5 Gyr) properties with uncertainties.

biological enhancement is not necessary for maintaining habitability. An abiotic Earth may remain habitable through the CO_2–H_2O greenhouse alone, provided the carbonate–silicate cycle operates.

Future work should nevertheless explore the sensitivity of climate evolution to low levels of abiotic CH_4. Even modest trace-gas abundances could influence atmospheric photochemistry and oxidation state. The atmospheric lifetime of methane depends strongly on OH generated from water-vapor photolysis (A. A. Pavlov et al. 2001). In an unshielded atmosphere without oxygenic photosynthesis, extended methane lifetimes could potentially allow greater accumulation than our simplified analysis suggests. Additionally, planets orbiting M and K dwarf stars may experience different photochemical regimes due to their host stars' UV spectra, potentially affecting methane lifetimes and the viability of methane as a warming agent on abiotic worlds (A. Segura et al. 2005; G. Arney et al. 2016). Incorporating volcanic CH_4 outgassing coupled to mantle redox-state evolution would establish a more complete abiotic baseline for interpreting future observations of exoplanets orbiting different stars.

5.3. Abiotic Marine Calcite Budget

Tuning the calcite saturation and concentration to achieve the observed preindustrial ocean DIC and approximate pH represents an oversimplification of the terrestrial carbon cycle, as demonstrated by the larger model disagreement for

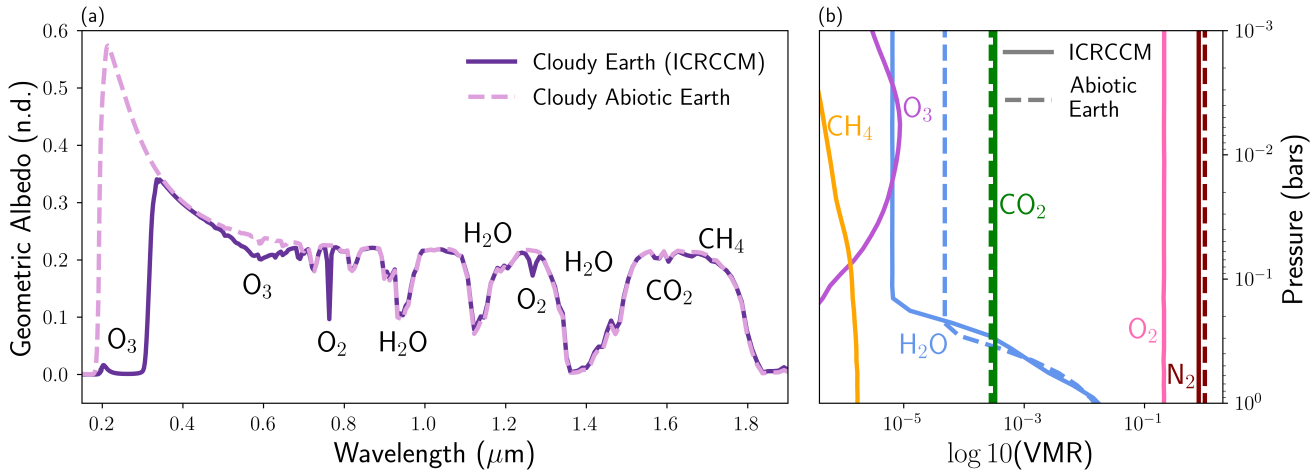


Figure 8. (a) A comparison of reflected-light spectra for a realistic, cloudy Earth and the abiotic atmospheric state after 4.5 Gyr. The abiotic atmosphere lacks O_2 (and therefore O_3) and CH_4, contributing to differences in absorption. (b) A comparison of the input molecular abundance profiles used to generate each reflected-light spectrum. We address minor differences between the CO_2, H_2O, and N_2 profiles in the accompanying text. Though the true profiles extend to a TOA pressure of 1×10^{-5} bars, we only show the surface to the upper stratosphere to better emphasize the differences in the water-vapor profiles given the logarithmic scale.

ocean pH and aqueous CO_2 concentration. We tune the calcite saturation and concentration to match the observed total DIC, but this choice then constrains the carbonate ion concentration via the calcite saturation equation (Equation (25)), which in turn determines the partitioning among carbonate species through equilibrium constants (Equations (26), (27), and (28)), and ultimately fixes the pH. This cascade of constraints means that solely tuning calcite concentration to match total DIC does not guarantee agreement with other observables that depend on the same carbonate chemistry, including pH and $(CO_2)_{aq}$.

The larger pH offset highlights a fundamental limitation of our simplified ocean chemistry model: We assume calcite saturation and do not explicitly track total alkalinity as an independent variable, such as in J. Krissansen-Totton et al. (2021). In a more complete carbonate system, total alkalinity and DIC jointly determine pH and carbonate speciation. By fixing calcite concentration to match DIC, we implicitly constrain alkalinity through the carbonate equilibrium, removing a degree of freedom that would otherwise allow independent adjustment of pH.

The primary distinction between our abiotic model and a biologically mediated carbon cycle lies in how carbon is packaged for gravitational transport from the surface to the seafloor. The biological pump creates heavier, rapidly sinking aggregates (marine snow, fecal pellets, shells) from organic and inorganic carbon (U. Passow & C. A. Carlson 2012), allowing more carbon to reach the deep ocean before remineralization. Life effectively enhances gravitational export of carbon and influences the depth at which remineralization occurs. Organisms migrating vertically through the water column also transport metabolized carbon (F. A. Le Moigne 2019), but gravitational sinking dominates in modern oceans (P. W. Boyd et al. 2019; M. Nowicki et al. 2022; D. A. Siegel et al. 2023). In an abiotic ocean, gravitational settling of inorganic precipitates would still occur, but the size distribution, sinking velocities, and spatial patterns of carbonate formation would likely differ from those of a biologically mediated system.

Furthermore, it is unclear whether abiotic calcite is less thermodynamically stable than its biogenic counterpart. D. Zhuang et al. (2018) suggest that abiotic calcite is less stable than biogenic calcite due to lower crystallinity and activation energy, but F. Stalport et al. (2005) found that biologically precipitated calcite thermally degrades at temperatures approximately 40°C cooler than abiotic calcite, suggesting greater thermal stability of abiotic crystals at elevated temperatures. Pessimistically, these differing material properties, combined with the orders-of-magnitude slower precipitation kinetics (S. J. Carpenter & K. C. Lohmann 1992), imply that achieving high calcite concentrations in an abiotic ocean may require either longer equilibration times or higher degrees of supersaturation than in living systems.

The extent to which an uninhabited planet could accumulate and maintain the calcite concentrations necessary to operate an effective carbonate–silicate thermostat remains an open question, with implications for the long-term habitability of abiotic, Earth-like exoplanets. The calcite concentration directly impacts carbonate chemistry and thus the efficiency of oceanic carbon sequestration and weathering feedbacks. Future work should incorporate a more complete carbonate system with total alkalinity as a prognostic variable, following approaches like J. Krissansen-Totton et al. (2021). Additionally, systematic parameter-space explorations should assess the sensitivity of ocean chemistry, atmospheric CO_2 regulation, and surface temperature to variations in calcite concentration and alkalinity. Such studies would help establish the range of abiotic carbonate cycling rates compatible with maintaining temperate surface conditions on terrestrial planets over billion-year timescales.

5.4. Implications for the Gaia Hypothesis

Since its introduction by J. E. Lovelock & L. Margulis (1974), the Gaia hypothesis has spurred long-running debates over life's role in long-term climate stability (i.e., habitability). In evaluating Lovelock's original theory, J. W. Kirchner (1989) argued for recategorizing Gaia into "weak" and "strong" variants—weak Gaia argues that interactions between living and abiotic processes have some stabilizing effect on the Earth; strong Gaia asserts that such interactions are the *most significant* process stabilizing Earth's climate. Strong Gaia proponents thus argue that life stabilizes the planetary

thermostat by regulating temperature, atmospheric composition, and ocean chemistry to maintain conditions favorable to its survival and propagation (J. E. Lovelock & L. Margulis 1974; J. E. Lovelock 1983; J. Lovelock 2000, 2016).

Generally, criticisms of the Gaia hypothesis acknowledge that life alters its environment, but point out that, despite some compelling examples, life's activities are not always favorable to its long-term survival. For instance, on the modern Earth, marine plankton "plunder" surface ocean nutrients, creating widespread biological deserts (T. Volk 2002; J. W. Kirchner 2003). Furthermore, anthropogenic climate change is a salient contemporary example of how biological activity can *disrupt* rather than stabilize the climate system (J. W. Kirchner 2002, 2003). These examples demonstrate that biological feedbacks are not intrinsically homeostatic.

More recently, modeling studies have investigated whether life can actively contribute to maintaining long-term planetary habitability. A. E. Nicholson et al. (2018) developed the ExoGaia model, which simulates how abiotic geochemistry and microbial metabolisms interact to influence surface temperature. They found that, under stable conditions, microbial metabolisms can prevent planets from reaching inhospitable temperatures that would otherwise occur on their lifeless counterparts. O. D. Alcabes et al. (2020) extended this work by subjecting planets to three types of global climate perturbations, finding that planets with Gaian feedbacks are most resilient to global climate change, especially when the changes are gradual. Together, these ExoGaia studies suggest that if life does emerge on a planet, it may under certain conditions evolve stabilizing feedbacks that enhance the long-term habitability of the host planet.

However, these models investigate whether life *can* stabilize planetary climate under a weak Gaia hypothesis, not whether life is *necessary* for climate stability as in the strong Gaia hypothesis. As further evidence against a strong Gaia mechanism, J. W. Kirchner (1989) identified purely geophysical models that produce long-term climate stability without invoking life at all (J. C. Walker et al. 1981; R. A. Berner et al. 1983). Our results are in agreement with these models. We demonstrate that an Earth-like planet can maintain habitable surface temperatures over 4.5 Gyr of evolution (and longer) through abiotic processes alone, without requiring biological feedbacks for climate regulation.

The carbonate–silicate cycle, driven by the interplay between silicate weathering, volcanic outgassing, and ocean chemistry, provides a robust negative feedback that keeps atmospheric CO_2 and surface temperature within habitable bounds despite the Sun's luminosity increasing by approximately 30% over 4.5 Gyr. Critically, our model demonstrates this climate stability while self-consistently evolving all major planetary subsystems: the interior cools and outgassing rates decline; the magnetic dynamo weakens and the magnetopause contracts; ocean chemistry adjusts to changing atmospheric CO_2; and the incoming stellar flux steadily increases. Despite these dramatic changes, the coupled system maintains surface temperatures between 285 and 297 K throughout the evolution. This represents a more complete test of climate stability than previous models that considered the carbon cycle in isolation, as it demonstrates that the carbonate–silicate thermostat functions robustly even when embedded within a fully evolving planetary system with realistic feedbacks between interior, surface, atmosphere, and external forcing from the brightening Sun.

As discussed above, our model does simplify ocean chemistry, which biology enhances on the modern Earth (Section 5.3). However, the fundamental mechanism of climate stabilization—the temperature and CO_2 dependence of silicate weathering coupled to carbonate precipitation and subduction—operates independently of life. While life may affect the *spatial distribution* and *kinetics* of carbonate precipitation, these biological enhancements may not be necessary for long-term climate stability.

That life may not be a requirement of a habitable planet has important implications for understanding Earth's habitability and for predicting conditions on rocky exoplanets. The persistence of habitable conditions over geological time may not require life to actively regulate the climate, rather potentially emerging from volatile cycling between planetary reservoirs. Habitable conditions may have been created on the early Earth by the abiotic carbonate–silicate cycle. Once life emerged, it may have developed stabilizing feedbacks, as suggested by ExoGaia-type models (A. E. Nicholson et al. 2018; O. D. Alcabes et al. 2020), potentially altering weathering rates, ocean chemistry, and atmospheric composition. However, our results suggest that the underlying abiotic stabilization mechanism provided by the carbonate–silicate cycle can maintain habitability independently. While we cannot rule out that life enhances climate stability (weak Gaia), our results suggest that life may not be a requirement of a habitable planet.

The implication that life may not be a requirement of a habitable planet raises a complementary question: Given a habitable planet, how long does it take for life to emerge? On Earth, mineralogical evidence confirms that liquid-water oceans existed as early as 4.4 Ga (E. M. Cameron et al. 2024), while the oldest widely accepted evidence for life—stromatolites from the Pilbara Craton—dates to 3.5 Ga (M. Walter et al. 1980). Though more ancient biogenic signatures have been proposed (and continue to be highly disputed), the stromatolite evidence provides a conservative estimate that life emerged within approximately 900 Myr of ocean formation. It has been suggested that this relatively rapid emergence of life on Earth implies that life may also rapidly emerge on habitable exoplanets (D. Kipping 2025). Our results support this conjecture by showing how Earth could have been habitable but abiotic for billions of years, yet life still appeared relatively shortly after the appearance of habitable conditions. On the other hand, our model suggests that habitable surface conditions can persist for billions of years through purely abiotic mechanisms, potentially providing a prolonged "prebiotic window" during which the chemical building blocks of life could accumulate and undergo the reactions necessary for creating life.

Potentially habitable exoplanets observed by future missions may be captured at various stages of their prebiotic evolution: Some may harbor early life similar to Earth at 3.5 Ga, while others could still be accumulating prebiotic chemistry despite having maintained habitable conditions for comparable or even longer durations. Indeed, our results suggest that rocky planets with plate tectonics, liquid-water oceans, and silicate weathering can maintain habitable surface conditions over billion-year timescales without requiring biology. Thus, the mere presence of habitable conditions is not sufficient evidence that

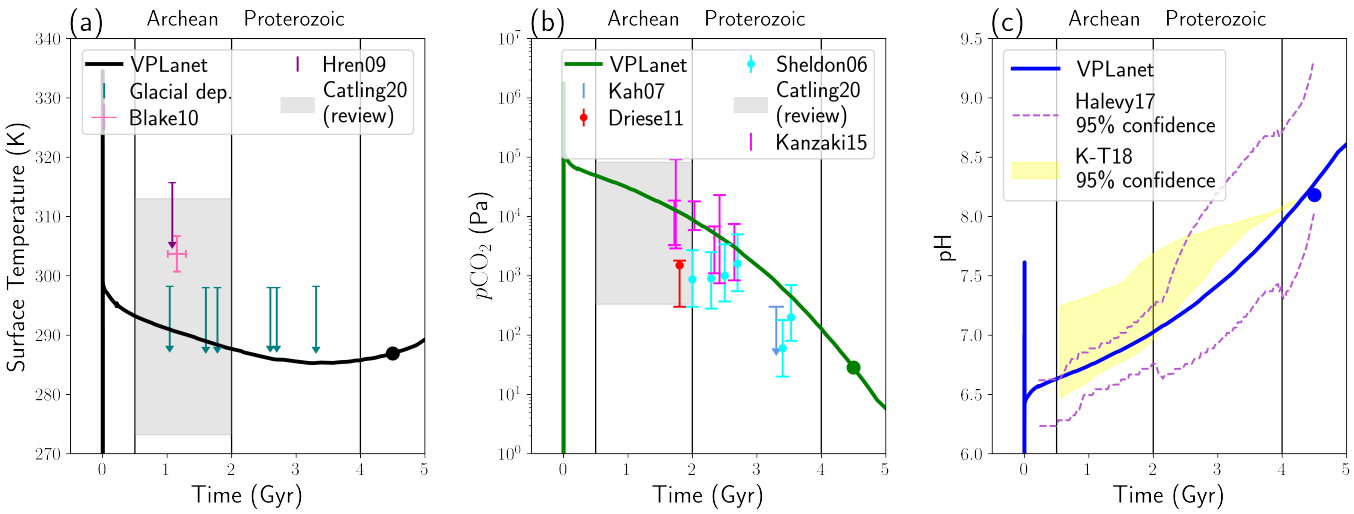


Figure 9. Comparison of the `VPLanet` abiotic Earth model evolution (solid curves) against paleoclimate proxy reconstructions from the literature, following the framework of J. Krissansen-Totton et al. (2018). Vertical black lines demarcate the Archean (∼0.5–2.0 Gyr) and Proterozoic (∼2.0–4.0 Gyr) eons. Filled black, green, and blue circles mark PIE values. (a) Surface temperature evolution compared with glacial deposit occurrences (teal arrows; G. M. Young et al. 1998; G. E. Williams 2005; N. J. Geboy et al. 2013; G. Kuipers et al. 2013; R. W. Ojakangas et al. 2014; M. J. de Wit & H. Furnes 2016), δ^{18}O and organic phosphate constraints (R. E. Blake et al. 2010; Blake10), δ^{18}O and deuterium isotopes in 3.42 Ga cherts (M. Hren et al. 2009; Hren09), and the habitable temperature range reviewed in D. C. Catling & K. J. Zahnle (2020; Catling20). Downward arrows denote upper limits. (b) Atmospheric pCO$_2$ evolution compared with cyanobacterial sheath calcification upper bounds (L. C. Kah & R. Riding 2007; Kah07), paleosol-based estimates from S. G. Driese et al. (2011; Driese11) and N. D. Sheldon (2006; Sheldon06), aqueous soil chemistry models (Y. Kanzaki & T. Murakami 2015; Kanzaki15), and the habitable range reviewed in D. C. Catling & K. J. Zahnle (2020). (c) Ocean pH evolution compared with 95% confidence intervals from the carbonate-alkalinity model of I. Halevy & A. Bachan (2017; Halevy17) and the coupled carbon-cycle model of J. Krissansen-Totton et al. (2018; K-T18).

a planet is inhabited. Some worlds may remain prebiotic for prolonged periods, or never give rise to life at all. Distinguishing inhabited from uninhabited-but-habitable worlds will therefore require (1) detecting disequilibrium biosignature gases (J. E. Lovelock & L. Margulis 1974; V. S. Meadows et al. 2018) or surface features directly attributable to biological activity (E. W. Schwieterman et al. 2018), but also (2) a well-quantified abiotic baseline for the potential mimics of biosignature gases and surface biosignatures (e.g., N. Wogan et al. 2020; J. Krissansen-Totton et al. 2021).

5.5. Comparison to Earth Evolution

While we did not aim to validate our results on the early Earth, we can broadly compare our model predictions to measurements of global average paleoclimate conditions in the literature. Following J. Krissansen-Totton et al. (2018), we compare the evolution of surface temperature, atmospheric pCO$_2$, and ocean pH against paleoclimate proxy data in Figures 9(a), (b), and (c), respectively. We also qualitatively compare our interior thermal evolution to previous work. Overall, we find that our abiotic model largely reproduces paleo pCO$_2$ and ocean pH estimates across much of Earth's history and yields a mantle thermal history that is consistent with most previous models, while predicting systematically cooler surface temperatures than biotic proxy reconstructions suggest.

Across the Archean (∼0.5–2.0 Gyr) and Proterozoic (∼2.0–4.0 Gyr) eons, we find that our predicted pCO$_2$ remains broadly consistent with measurements established via mass-balance models of weathering (N. D. Sheldon 2006) and with the higher CO$_2$ abundances predicted by Y. Kanzaki & T. Murakami (2015) based on modeling of aqueous soil chemistry. Our predicted pCO$_2$ is several times higher than a Precambrian upper bound estimated from calcification of cyanobacterial sheaths (L. C. Kah & R. Riding 2007). Our model also predicts global Archean surface temperatures that are consistent with the lower end of estimates based on measurements of glacial deposits (G. M. Young et al. 1998; G. E. Williams 2005; N. J. Geboy et al. 2013; G. Kuipers et al. 2013; R. W. Ojakangas et al. 2014; M. J. de Wit & H. Furnes 2016), but several kelvins cooler than estimates from measurements of δ^{18}O and deuterium isotopes in 3.42 Ga cherts (M. Hren et al. 2009) and δ^{18}O and organic phosphate (R. E. Blake et al. 2010). During the Proterozoic, our model predicts consistently cooler surface temperatures from measurements of glacial deposits. Lastly, our ocean pH throughout the evolution is consistent with estimates from I. Halevy & A. Bachan (2017), but is consistently more acidic than estimates from J. Krissansen-Totton et al. (2018). The offset in pH likely reflects our simplified treatment of ocean alkalinity (see Section 5.6), while our somewhat cooler surface temperatures are in line with prior work identifying biogenic CH$_4$ from methanogens as an important greenhouse contributor on the early Earth (A. A. Pavlov et al. 2000; P. Kharecha et al. 2005). An abiotic world would lack such elevated CH$_4$ abundances and, under a faint young Sun, may evolve along a colder trajectory.

While proxy evidence gives a validation baseline for paleo-Earth climate, Earth's early interior evolution is harder to constrain. C. Herzberg et al. (2010) compiled petrologic estimates of mantle temperature over Earth history, which reveal more or less monotonic mantle cooling since the Archean. However, there is significant uncertainty in mantle temperature and cooling rates in the Archean and Hadean, with models predicting either early heating periods (J. Korenaga 2008a, 2008b) either/or monotonic cooling (P. Driscoll & D. Bercovici 2014).

Earth's noble gas record provides specific evidence that past escape may have been significant. Atmospheric xenon is strongly depleted and isotopically fractionated relative to other noble gases, and one plausible explanation is enhanced escape in Earth's past: Vigorous hydrogen escape fueled by the young Sun's elevated X-ray and ultraviolet (XUV) flux could have dragged along ionized xenon (K. J. Zahnle et al. 2019). Such vigorous atmospheric escape early in Earth's history potentially contributed to the permanent oxidation of our atmosphere (D. C. Catling et al. 2001). If xenon fractionation represents continuous escape, Earth may have lost the hydrogen from at least one ocean of water across the Hadean and Archean (K. J. Zahnle et al. 2019), which would make our assumption of a fixed volatile inventory unreasonable (Section 3.1). However, translating the xenon record into a well-constrained escape history remains difficult. The duration and continuity of xenon escape mechanisms are uncertain (K. J. Zahnle et al. 2019), and alternative explanations, like trapping of heavy xenon isotopes in organic hazes (E. Hébrard & B. Marty 2014; G. Avice et al. 2018) and sequestration in the crust (R. Parai & S. Mukhopadhyay 2018), may explain the observed fractionation without requiring enhanced atmospheric escape rates (G. Gronoff et al. 2020). Given these open questions, we acknowledge that an explicit treatment of atmospheric escape should be included in future work (Section 5.6).

A subtler tension in this comparison is that the present-day Earth system parameters against which we tune and validate our model are themselves the product of ∼4 Gyr of coupled biological and geological evolution. In calibrating an abiotic model to reproduce these end-point values, we are implicitly asking whether an abiotic Earth *could* have arrived at a state quantitatively similar to the present-day Earth. Our results indicate that such a solution is achievable in principle, but the broader question of which global properties depend on biotic versus abiotic processes requires future work.

Nonetheless, our model demonstrates that many of the present-day global geophysical conditions remain achievable along an abiotic pathway. We emphasize that this solution is not necessarily unique: Other plausible evolutionary trajectories could also reproduce modern conditions, and our results likely represent one of a suite of Earth-like solutions. More broadly, our findings suggest that the presence or absence of life may meaningfully contribute to the thermal trajectory of an Earth-like planet—an abiotic Earth plausibly evolves through a substantially cooler climate history than the biotic Earth inferred from proxy data, even while converging on the same present-day state. This work is a step toward systematically mapping the broader space of both biotic and abiotic evolutionary histories consistent with present-day Earth.

5.6. Future Work

Our core–mantle–crust–climate model reproduces the conditions of the PIE without life, and provides a foundation for future studies aiming to simulate the evolving habitability of rocky exoplanets as well as the observable signatures of these states. However, we found that our simple cloud parameterization is likely insufficient to model realistic radiative forcing from clouds. We tuned a wavelength-independent cloud opacity pressure to match PIE surface temperature, resulting in an unrealistically low cloud fraction of 8% compared to Earth's observed 67% average cloud coverage (B. A. Wielicki et al. 1996). This discrepancy arises because we "paint" clouds onto the surface rather than self-consistently calculate cloud formation and radiative effects within the atmospheric column (T. Fauchez et al. 2018). Future work should reconcile this inconsistency.

Our treatment of atmospheric processes spans a spectrum of physical fidelity. For surface temperature, atmospheric water-vapor partitioning, and radiative transfer, we employ first-principles physics: `Clima` solves the radiative-transfer equations with wavelength-dependent opacities, while water vapor is constrained by the Clausius–Clapeyron relation at each atmospheric level. By contrast, clouds are parameterized—the cloud opacity scale and reflectance parameters are calibrated to reproduce the PIE's cloud radiative effect, and are not derived from first-principles cloud microphysics.

While more sophisticated 1D cloud treatments exist (A. S. Ackerman & M. S. Marley 2001; A. Zsom et al. 2012; T. Fauchez et al. 2018; C. Helling 2019; J. D. Windsor et al. 2023), implementing them would largely trade our current free parameters for others (e.g., sedimentation efficiency in microphysical models), without fundamentally resolving the uncertainties inherent to representing 3D cloud processes in 1D globally averaged models. Clouds remain the dominant source of uncertainty in 3D general circulation models (GCMs) due to the complex interplay of microphysics, planet-wide dynamics, and radiative transfer (T. Mauritsen et al. 2012; J. Vial et al. 2013; M. J. Way et al. 2018). For the purposes of investigating long-term planetary evolution across diverse parameter spaces, a more pragmatic approach is to acknowledge this uncertainty explicitly and marginalize over plausible cloud parameter ranges when conducting broad explorations of Earth-like exoplanets. By varying our cloud opacity pressure and cloud albedo parameters across physically motivated ranges in future studies, we can assess how cloud radiative forcing uncertainties affect predicted habitability outcomes without requiring self-consistent calculations of cloud microphysics.

Further improvements to the model would ensure that it can capture additional feedback mechanisms of planets on diverse evolutionary paths. These improvements include incorporating additional volatile cycles and early Earth processes that affect the planet's initial conditions. Below, we discuss potential model improvements and describe applications to exoplanet studies, which may include coupling our model outputs to 3D GCMs to better capture the complexity of surface processes like clouds and ice coverage.

Our model currently only handles CO_2 and H_2O cycling, which is a subset of Earth's geologically active volatiles. Following J. Krissansen-Totton et al. (2021), we assume that N_2 remains a bulk gas by setting it to a constant of 1 bar throughout the evolution. Future work should incorporate abiotic nitrogen cycling into our whole-planet model, as the abundance of atmospheric N_2 affects surface pressure and impacts the surface temperature of the planet via CIA (E. W. Schwieterman et al. 2015) and pressure broadening of CO_2 and H_2O (C. Goldblatt et al. 2009). Furthermore, M. Laneuville et al. (2018) showed that, in an abiotic context, the abundance of atmospheric nitrogen is highly dependent on surface and interior processes, suggesting this form of volatile cycling is ripe for inclusion in a whole-planet modeling framework.

Future work should explore the sensitivity of long-term climate evolution to different assumptions about the efficiency of continental weathering on an abiotic planet without land vegetation. Previous habitability studies have suggested that land plants enhance continental weathering rates beyond purely abiotic levels, potentially driving abiotic planets to equilibrate at a higher pCO_2 (J. Haqq-Misra et al. 2016) and enhancing the likelihood of living planets experiencing global glaciation events (S. Kadoya & E. Tajika 2019). However, the quantitative contribution of biology to silicate weathering rates remains poorly constrained. Field estimates of the biotic enhancement factor span nearly 2 orders of magnitude (e.g., M. Ford Cochran & R. A. Berner 1996; C. Dessert et al. 2003), and no true abiotic control site exists on Earth today (B. Wild et al. 2022). Marginalizing over a range of weathering assumptions would help quantify the effect of this uncertainty and bracket the range of plausible pCO_2 trajectories and surface temperatures for abiotic Earth-like planets, establishing more robust predictions for HWO observations.

While low abiotic CH_4 abundances likely do not directly contribute to greenhouse warming, methane nevertheless plays an important role in atmospheric chemistry and redox balance (A. A. Pavlov et al. 2001). The atmospheric abundance and lifetime of CH_4 depends on the availability of photochemically generated oxidants, which in turn depends on the planet's oxidation state, which is itself influenced by hydrogen escape to space (D. C. Catling et al. 2001; K. J. Zahnle et al. 2019). Atmospheric escape is therefore critical for determining both the feasibility of detecting abiotic methane and for interpreting CH_4 observations as potential biosignatures.

More broadly, atmospheric escape processes—particularly XUV-driven hydrodynamic and thermal escape—can substantially alter volatile inventories, atmospheric composition, and planetary oxidation state over billion-year timescales (D. C. Catling et al. 2001; R. Luger & R. Barnes 2015; M. T. Gialluca et al. 2024). On Earth itself, predictive models suggest that as the Sun brightens by $\sim$10% over $\sim$1 Gyr, hydrogen escape will effectively desiccate the surface, leaving small habitable oases only at the poles (J. F. Kasting 1988; D. C. Catling & K. J. Zahnle 2009). This possibility is especially important for planets orbiting lower-mass stars like M and K dwarfs, which experience extended pre-main-sequence phases compared to G and F dwarfs, with high XUV fluxes that can drive significant atmospheric loss (J. Chadney et al. 2015; D. Atri & S. R. C. Mogan 2021). For example, on M dwarf planets, preferential hydrogen escape oxidizes the atmosphere and potentially the mantle, affecting volcanic outgassing composition (the CH_4/CO_2 ratio), ocean chemistry, and the operation of the carbonate–silicate cycle (L. Schaefer et al. 2016; F. Gaillard et al. 2022).

The planetary magnetic field also helps determine which atmospheric escape channels operate. While a magnetosphere shields the atmosphere from stellar-wind sputtering and ion pickup, it simultaneously enables ion outflow through the polar caps and cusps, and models spanning a range of magnetizations find that intermediate magnetic moments can enhance, rather than suppress, total escape (H. Gunell et al. 2018; G. Gronoff et al. 2020). Furthermore, some atmospheric constituents may be more amenable to magnetic-limited escape, which would imply that certain types of atmospheres (e.g., low molecular mass) are more vulnerable to escape (G. Gronoff et al. 2020). Coupling such magnetization-dependent, nonthermal escape processes to the dynamo evolution predicted by interior thermal models in a whole-planet framework like ours would offer a path toward addressing this question self-consistently.

Giant impacts during planetary formation and early bombardment can also drive atmospheric loss while simultaneously creating transient, reduced atmospheres enriched in H_2 and potentially CH_4 (K. J. Zahnle et al. 2020). Future work should couple atmospheric escape and impact-driven atmospheric evolution to our model to track how early volatile loss shapes long-term habitability, particularly for planets around active K dwarfs, which will be prime targets for atmospheric characterization with HWO (G. N. Arney 2019; E. Mamajek & K. Stapelfeldt 2023). Incorporating volcanic CH_4 outgassing, escape-driven oxidation, and impact-driven reducing conditions will establish a complete abiotic baseline against which to interpret methane detections in exoplanet atmospheres.

Our model is initialized after the magma ocean has crystallized. However, the magma ocean phase shapes the atmospheric composition and surface temperature of the early Earth. Volatiles incompatible with the magma ocean are released into the atmosphere (L. T. Elkins-Tanton 2012), and the rate at which the magma ocean cools may also contribute to whether or not a planet develops plate tectonics (L. Schaefer & L. T. Elkins-Tanton 2018). Thus, our model potentially underestimates the initial surface temperature and atmospheric volatile inventory of the planet, and does not account for how this early evolutionary process ultimately shapes Earth's habitability.

Though this work does not couple to the magma ocean, `VPLanet` already includes a magma ocean model. L. Carone et al. (2025) updated `MagmOc`, `VPLanet`'s magma ocean module, demonstrating good agreement with previous magma ocean models (L. T. Elkins-Tanton 2008; A. Nikolaou et al. 2019; T. Lichtenberg et al. 2021). Future work could integrate the `MagmOc` module into this whole-planet modeling framework and model the planet continuously from the magma ocean phase into the solid-mantle phase (e.g., J. Krissansen-Totton et al. 2021).

Finally, our 1D model is not designed to account for complicated 3D planetary phenomena like transitions to global glaciation states. Modeling a realistic ice-albedo feedback and snowball Earth transitions likely requires latitude-dependent insolation and heat transport that 1D globally averaged models cannot wholly capture (D. S. Abbot et al. 2013; P. F. Hoffman et al. 2017; B. E. Rose et al. 2017; C. Wilhelm et al. 2022). Similarly, substantial discrepancies exist between 1D and 3D models regarding the height of cloud formation, cloud optical properties, and the climate impacts of clouds (J. Yang et al. 2016; M. J. Way et al. 2018; C. Helling 2019; T. D. Komacek & D. S. Abbot 2019).

Rather than attempting to fully incorporate these 3D phenomena into our 1D framework, we envision a complementary modeling approach. Our evolutionary model provides realistic time-dependent boundary conditions for GCM simulations: atmospheric composition, volatile inventories, interior heat flux, and incoming stellar flux at snapshots throughout planetary evolution. GCMs can then simulate the spatial climate patterns, ice coverage, cloud distributions, and circulation for these evolved atmospheric states (E. T. Wolf et al. 2022). Conversely, GCM-derived quantities—such as a spatially averaged albedo that includes realistic cloud

distributions, ice surface fractions, and meridional heat-transport efficiencies—can inform improved parameterizations in 1D evolutionary models without sacrificing the computational speed required to cover large parameter sweeps over billion-year timescales. This iterative dialog between complementary modeling approaches leverages the strengths of each: 1D models are appropriate for long-term interior-atmosphere coupling, while 3D models are useful for simulating spatially resolved climate states with realistic cloud and ice feedbacks. The integration of different modeling techniques will likely be essential for interpreting future observations of exoplanet atmospheres and for predicting which planets are most likely to maintain habitable conditions over geological time.

With the additional model developments described above, a whole-planet framework could be used to assess abiotic mimics of life on Earth-like exoplanets. For example, an improved version of the model could build on the work of J. Krissansen-Totton et al. (2021) by assessing the evolution of abiotic O_2 in the atmospheres of exoplanets around Sun-like stars with a fully coupled core model. Our model would include the effect of an evolving core on the planet's magnetosphere and the efficiency of hydrogen escape, which regulates the accumulation of abiotic O_2. The improved model could also be used to investigate the abiotic generation of other biosignature gases, like CH_4. This would expand on previous investigations of abiotic mimics by considering the evolution of the core–mantle system in addition to the star and planetary atmosphere.

In its current form, our model is well poised for large parameter-sweep explorations of Earth-like exoplanets throughout the HZs of FGK stars, both for the exploration of habitable planet properties and for the simulation of variations in observable signatures of habitability. For this Earth validation study, we solely show our model coupled to solar evolution, but the `VPLanet` stellar model can simulate main-sequence stars with masses up to 1.4 $M_\odot$. This mass range encompasses Sun-like FGK stars that HWO will eventually target for observation.

Using preliminary HWO stellar target lists from E. Mamajek & K. Stapelfeldt (2023) and N. W. Tuchow et al. (2025), future work could simulate planets with the mass, radius, and tectonic regime of the Earth at various separations from FGK host stars. Since our coupled climate model performs full ASR and OLR calculations, it can be used to simulate the conditions at both the inner and outer edges of the HZ. At the inner edge, planets cease to be habitable when they enter the runaway greenhouse phase, and at the outer edge, CO_2 scattering sets the maximum greenhouse limit (R. K. Kopparapu et al. 2013). To explore a wide range of planets, we can vary the initial CO_2 and H_2O inventories, as well as interior parameters like the radiogenics budget and the initial mantle and core temperatures. The unique luminosity evolution of each target star, combined with various model parameters, will shape the climate of a given planet over time, ultimately determining its potential long-term habitability.

Importantly, our evolutionary framework allows us to generate atmospheric states and synthetic HWO observations not just at a single end point, but at multiple snapshots throughout a planet's history. A single Earth-like planet may exhibit dramatically different spectroscopic signatures at 1, 3, and 5 Gyr as its atmosphere, interior, and surface evolve in response to changing stellar forcing and volatile cycling. This application of our model could reveal how the stability of the Earth system is affected by different stellar types. For example, the comparatively slow luminosity evolution of K dwarfs may promote long-term climate stability over the extended main-sequence lifetime of these stars, while the relatively rapid brightening of F dwarfs may challenge the climate stability of Earth-like exoplanets. The time-resolved atmospheric states across different evolutionary epochs can then be used to produce simulated HWO observations, providing insight into the range of spectral characteristics consistent with purely abiotic planetary conditions. This temporal dimension is crucial: The diversity of abiotic habitable worlds HWO will sample reflects not only variations in initial conditions and host-star properties, but also the natural evolution of planetary systems captured at different ages.

6. Conclusions

Here, we have presented a coupled core–mantle–crust–climate model that reproduces geophysical, climate, and ocean properties of the PIE. Our model predicts that life may not be required to maintain a habitable planet resembling Earth-like conditions. This work thus contributes to the ongoing debate regarding the Gaia hypothesis by suggesting that life and habitability may be somewhat decoupled.

In terms of future applications, our model is intended to be applied to the evolution of rocky exoplanets. Our model shows that the evolution of the planetary interior plays an important role in determining the long-term habitability of Earth-like exoplanets. Thus, including realistically evolving planetary interiors is a crucial aspect of whole-planet modeling and should account for potentially non-Earth-like compositions in order to illuminate the potential equilibrium states of rocky planets.

Though exoplanet interiors themselves will likely never be directly observable, the effects of interior evolution are apparent in the composition of the atmosphere and the albedo of the surface environment, both of which HWO will observe on Earth-like planets around Sun-like stars via reflected-light spectroscopy. We have demonstrated that atmospheric states from our model can generate realistic reflected-light spectra that capture the key differences between inhabited and uninhabited worlds, establishing an abiotic baseline for biosignature interpretation. The model presented here is compatible with modeling the long-term habitability of theoretical exoplanets around key HWO targets. For quantifying the null hypothesis and establishing an abiotic baseline, additional model development is required. Nevertheless, our core–mantle–crust–ocean–atmosphere–stellar model represents significant progress toward the ambitious goal of whole-planet modeling, which itself is a key step toward advancing our search for life in the Universe.

Acknowledgments

We thank Joshua Krissansen-Totton, Jacob Lustig-Yaeger, Thomas Quinn, and two anonymous reviewers for their helpful comments, which improved this manuscript. Funding for S.G.-J. and A.M.M. was provided by the Exoplanet Spectroscopy Technologies Team at NASA Goddard, which is supported through the NASA Astrophysics Division Internal

Scientist Funding Model. S.G.-J. was also supported by NASA award No. 80NSSC24M0049. R.K.B. was supported by NASA award No. 80NSSC24K0856, and R.G. was supported by NASA award No. 80NSSC23K0261. N.F.W. was supported by the NASA Postdoctoral Program. L.C. acknowledges support by the DFG priority program SP1833, "Building a habitable Earth," grant CA 1795/3.

Software: `VPLanet` (R. Barnes et al. 2020), `Clima` (N. F. Wogan et al. 2025b), `SciPy` (P. Virtanen et al. 2020).

Appendix A
Constants

Table A1 provides the values of constants used in the model.

Table A1
All Constants Appear Here in Alphabetical Order, with Greek Letters Appearing Last

Symbol	Parameter	Value
$a_{\rm grad}$	Best-fit deep-ocean temperature/global mean surface temperature gradient	1.02 [n.d.]
a_1	Saturation vapor pressure scaling parameter for silicate weathering	0.3 [n.d.]
a_2	Plate velocity scaling parameter	35.0 [n.d.]
$A_{\rm B}$	Bond albedo	0.29 [n.d.]
$A_{\rm i}$	Ice albedo	0.6 [n.d.]
$A_{\rm oc}$	Ocean albedo	0.1 [n.d.]
$A_{\rm r}$	Rock albedo	0.17 [n.d.]
$A_{\rm Earth}$	Surface area of the Earth	5.1×10^{14} m^2
$b_{\rm int}$	Best-fit deep-ocean temperature/global mean surface temperature intercept	−16.7 [n.d.]
B	Viscosity-melt reduction coefficient	2.5 [n.d.]
$D_{\rm H_2O}$	Bulk H_2O distribution coefficient	0.01 [n.d.]
$E_{\rm a}$	Silicate weathering activation energy	42×10^3 J mol^{-1}
$E_{\rm a,man}$	Mantle viscosity activation energy	3×10^5 J mol^{-1}
$E_{\rm bas}$	Basalt weathering activation energy	92×10^3 J mol^{-1}
$E_{\rm max}$	Maximum erosion rate	3.2×10^{-10} m s^{-1}
$f_{\rm cc}$	Fraction of Mg, Ca, K, and Na in the continental crust	0.08 [n.d.]
f_h	Mass fraction of water in the serpentinized layer	0.03 [n.d.]
$F_{\rm sfw,0}$	Present-day seafloor weathering flux	55, 454 mol s^{-1}
$F_{\rm weather,0}$	Present-day silicate weathering flux	380, 257 mol s^{-1}
g	Surface gravity of the Earth	9.8 m s^{-2}
k	Thermal conductivity	4.2 W m^{-1} K^{-1}
L	Present-day length of ocean trenches	6×10^7 m
$L_{\rm w}$	Latent heat of water	2.469×10^6 J kg^{-1}
$\bar{m}_c$	Molar mass of CO_2	44×10^{-3} kg mol^{-1}
$\bar{m}_{\rm cc}$	Average molar mass of Mg, Ca, K, and Na	32×10^{-3} kg mol^{-1}
$\bar{m}_{\rm w}$	Molar mass of water	18×10^{-3} kg mol^{-1}
$M_{\rm man}$	Mass of the mantle	4×10^{24} kg
$pCO_{2\ ,0}$	Present-day partial pressure of atmospheric CO_2	33 Pa
$P_{\rm sat,0}$	Present-day saturation vapor pressure	1391 Pa
$P_{\rm sat,ref}$	Reference saturation vapor pressure	610 Pa
$R_{\rm c}$	Radius of Earth's core	3481×10^3 m
$R_{\rm g}$	Universal gas constant	8.314 J K^{-1} mol^{-1}
RH	Relative humidity	100%
$R_{\rm man}$	Radius of Earth's mantle	6371×10^3 m
$\rm Ra_{crit}$	Critical Rayleigh number	660 [n.d.]
S	Salinity	35 ppt
S_0	Solar constant	1369 W m^{-2}
$T_{\rm pore,0}$	Present-day pore-space temperature	283.03 K
$T_{\rm sat,ref}$	Reference saturation vapor temperature	273 K
$T_{\rm surf,0}$	Present-day surface temperature	285 K
v_0	Present-day plate speed	1.58×10^{-9} m s^{-1}
$V_{\rm man}$	Volume of Earth's mantle	9.1×10^{20} m^3
$\nu_{\rm ref}$	Reference kinematic mantle viscosity	4.8272×10^9 m^2 s^{-1}
$x_{\rm i,max}$	Maximum ice surface fraction	0.12 [n.d.]
$x_{\rm l,0}$	Present-day land fraction	0.29 [n.d.]
$x_{\rm oc,0}$	Present-day ocean fraction	0.71 [n.d.]
α	Strength of dependence of basalt carbonation on atmospheric CO_2	0.25 [n.d.]
β_1	Partial pressure of CO_2 scaling parameter for silicate weathering	0.55 [n.d.]
β_2	Scaling exponent of Rayleigh number for plate speed	1/3 [n.d.]
γ	Viscosity-melt reduction coefficient	6.0 [n.d.]
δ	Viscosity-melt reduction exponent	6.0 [n.d.]
$\Delta E_{\rm H_2O}$	Depression of mantle viscosity activation energy due to water	2.22×10^6 K/wt. frac.
κ	Thermal diffusivity	1×10^{-6} m^2 s^{-1}
ξ	Viscosity-melt reduction coefficient	5×10^{-4} [n.d.]
$\rho_{\rm man}$	Density of the mantle ($M_{\rm man}/V_{\rm man}$)	4395 kg m^{-3}
ρ_r	Density of regolith	2500 kg m^{-3}
$\sigma_{\rm SB}$	Stefan–Boltzmann constant	5.67×10^{-8} W m^{-2} K^{-1}
τ_{cl}	Cloud opacity pressure	4050 Pa
$\chi_{\rm degas,c}$	CO_2 degassing efficiency	0.3 [n.d.]
$\chi_{\rm sub,c}$	CO_2 subduction efficiency	0.2868 [n.d.]
$\chi_{\rm degas,w}$	Water degassing efficiency	1.0 [n.d.]
$\chi_{\rm regas,w}$	Water regassing efficiency	0.15508 [n.d.]
$\Omega_{\rm cal}/[Ca^{2+}]$	Marine calcite concentration	408.1 kg mol^{-1}

Note. Values without units are denoted as nondimensional (n.d.).

Appendix B
BMO Radiogenic Heating Calculation

Here, we provide a detailed derivation of the effective core radiogenic heating rate, which includes contributions from an enriched BMO layer. We calculate the ^{40}K enrichment needed to generate up to 3.5 TW of heat in the core, which our model requires to match the observed upper-mantle heat flow.

B.1. Derivation of the Effective Core Heating Rate

The core and BMO energy balances may be written as

$$M_{\rm C} c_{\rm C} \dot{T_{\rm C}} = Q_{\rm rad,C} + Q_{\rm IC} - Q_{\rm CMB}$$

and

$$M_{\rm BMO} c_{\rm BMO} \dot{T_B} = Q_{\rm CMB} + Q_{\rm rad,BMO} - Q_{\rm BMO},$$

respectively, where M denotes mass, c denotes specific heat, $\dot{T}$ denotes the time derivative of reservoir temperature, and Q denotes heat flow. The subscripts indicate the relevant reservoir: "C" and "IC" denote the core and inner core, respectively, "CMB" gives the core–mantle boundary, and

"BMO" is the basal magma ocean layer. Thus, $Q_{\mathrm{rad,BMO}}$ represents the radiogenic heat flow in the BMO, and $Q_{\mathrm{rad,C}}$ represents the radiogenic heat flow in the core. We neglect tidal heating, as it is not a significant source of internal heating for Earth (R. D. Ray et al. 1996). The negative sign on the left-hand side represents secular cooling. Adding these equations yields

$$M_{\mathrm{C}}c_{\mathrm{C}}\dot{T_{\mathrm{C}}} + M_{\mathrm{BMO}}c_{\mathrm{BMO}}\dot{T_{\mathrm{BMO}}} = Q_{\mathrm{rad,BMO}} + Q_{\mathrm{rad,C}} + Q_{\mathrm{IC}} - Q_{\mathrm{BMO}}.$$

We assume that the core and BMO cool at the same rate such that $\dot{T_{\mathrm{C}}} \approx \dot{T_{\mathrm{BMO}}}$. This assumption is justified if the more viscous solid mantle regulates the cooling rate of both reservoirs. This allows us to write

$$\dot{T_{\mathrm{C}}}(M_{\mathrm{C}}c_{\mathrm{C}} + M_{\mathrm{BMO}}c_{\mathrm{BMO}}) = Q_{\mathrm{rad,BMO}} + Q_{\mathrm{rad,C}} + Q_{\mathrm{IC}} - Q_{\mathrm{BMO}}. \quad \text{(B1)}$$

The heat released at the ICB is given by

$$Q_{\mathrm{IC}} = \dot{T_{\mathrm{C}}}\frac{dM_{\mathrm{IC}}}{dT_{\mathrm{C}}}(L_{\mathrm{H}} + E_{\mathrm{G}}), \quad \text{(B2)}$$

where $dM_{\mathrm{IC}}/dT_{\mathrm{C}}$ represents the change in inner-core mass with temperature, and L_{H} and E_{G} are the latent and gravitational energy released per unit mass at the ICB. Substituting into Equation (B1) yields

$$\dot{T_{\mathrm{C}}} = \frac{(Q_{\mathrm{rad,BMO}} + Q_{\mathrm{rad,C}}) - Q_{\mathrm{BMO}}}{\left(M_{\mathrm{BMO}}c_{\mathrm{BMO}} + M_{c}c_{\mathrm{C}}) - \frac{dM_{\mathrm{IC}}}{dT_{\mathrm{C}}}(L_{\mathrm{H}} + E_{\mathrm{G}}\right)}. \quad \text{(B3)}$$

The mass of the BMO is likely much smaller than that of the core. To show this, we can compare the density of each, finding that

$$\frac{M_{\mathrm{BMO}}}{M_{\mathrm{C}}} = \left[\left(\frac{R_{\mathrm{BMO}}}{R_{\mathrm{C}}}\right)^3 - 1\right]\frac{\rho_{\mathrm{BMO}}}{\rho_{\mathrm{C}}}, \quad \text{(B4)}$$

where $R_{\mathrm{BMO}} = R_{\mathrm{C}} + L_{\mathrm{BMO}}$, with $R_{\mathrm{C}} = R_{\mathrm{CMB}} = 3481$ km the radius of the core–mantle boundary (i.e., the outer surface of the core), and L_{BMO} the thickness of the BMO layer. Consistent with seismic observations of the density jump at the CMB (A. M. Dziewonski & D. L. Anderson 1981) and with high-pressure constraints showing that iron-enriched silicate melts are less dense than the metallic core (S. Labrosse et al. 2007), we assume that the BMO is half as dense as the core, $\rho_{\mathrm{BMO}}/\rho_{\mathrm{C}} \approx 0.5$. Using this conservative estimate of the density ratio, we find that M_{BMO} is maximally 20% that of the core for an initial BMO thickness of 400 km, as in S. Labrosse et al. (2007). The rapidly thinning BMO is even less massive than the core; for example, $M_{\mathrm{BMO}}/M_{\mathrm{C}} \approx 0.044$ for a 100 km-thick BMO, and $M_{\mathrm{BMO}}/M_{\mathrm{C}} \approx 0.009$ for a 20 km-thick BMO layer. Thus, for the majority of the evolution $M_{\mathrm{BMO}} \ll M_{\mathrm{C}}$, and we neglect the $M_{\mathrm{BMO}}c_{\mathrm{BMO}}$ term in Equation (B3). Combining the radiogenic heat from the BMO and core into one term, we find the final expression given in Equation (1) in Section 3.2:

$$\dot{T_{\mathrm{C}}} = \frac{Q_{\mathrm{rad,BMO+C}} - Q_{\mathrm{BMO}}}{M_{\mathrm{C}}c_{\mathrm{C}} - \frac{dM_{\mathrm{IC}}}{dT_{\mathrm{C}}}(L_{\mathrm{H}} + E_{\mathrm{G}})}. \quad \text{(B5)}$$

B.2. Required Radiogenic Enrichment

To estimate the possible heating power generated by a radiogenically enriched BMO, we account for heating from the four radioactive isotopes included in our model: ^{40}K, ^{232}Th, ^{235}U, and ^{238}U. We define the present-day heating contribution from each isotope as

$$Q_{\mathrm{rad,BMO,i,0}} = M_{\mathrm{BMO}}x_{\mathrm{BMO}}c_{\mathrm{i}}h_{\mathrm{i}}, \quad \text{(B6)}$$

where M_{BMO} is the mass of the BMO, x_{BMO} is the concentration of the parent species in the BMO, c_{i} is the relative abundance of each isotope, and h_{i} is the total radiogenic heating power per unit mass of the isotope. Table B1 provides the values of x_{BMO}, c_{i}, and h_{i} for each species. To solve for the mass of the BMO, we can write

$$M_{\mathrm{BMO}} = \rho_{\mathrm{BMO}}\frac{4\pi}{3}((R_{\mathrm{CMB}} + L_{\mathrm{BMO}})^3 - (R_{\mathrm{CMB}})^3), \quad \text{(B7)}$$

where ρ_{BMO} is the density of the BMO, and we solve for the volume of a L_{BMO}-thick BMO using the radius of the core–mantle boundary, $R_{\mathrm{CMB}} \approx 3481$ km.

S. Labrosse et al. (2007) modeled a primordial BMO of $L_{\mathrm{BMO}} \sim 400$ km that fractionally crystallizes to ~8 km over 4.5 Gyr. However, as the BMO solidifies and thins, incompatible elements are continuously expelled into the residual liquid, such that a thinner present-day BMO is expected to be more concentrated than a thicker earlier one. We assume a present-day BMO thickness of $L_{\mathrm{BMO}} = 4$ km, which we interpret as the highly enriched residual of a larger primordial BMO. Finally, we assume a BMO density of $\rho_{\mathrm{BMO}} = 6000$ kg m^{-3}, which is slightly denser than the solid mantle due to higher pressures. Substituting into Equation (B6) to solve for the individual radiogenic heat contributions for each of the four species, we find that the present-day total $Q_{\mathrm{rad,BMO,0}} = 3.67$ TW for a 4 km-thick BMO. This calculation demonstrates that attributing 3.5 TW of core heating to a radiogenically enriched, thin present-day BMO is physically plausible.

Table B1
Physical and Earth Properties Used for Radiogenic Heating Calculations in the BMO

Parameter	Species	Value	References
Bulk silicate Earth (BSE) concentration	K	260 ppmw	W. F. McDonough (2025)
	Th	77.6 ppbw	
	U	20.6 ppbw	
BMO enrichment factor (x_{BMO})	All	200 × BSE	S. Labrosse et al. (2007, their Figure 4)
Isotopic abundance (c_{i})	^{40}K	1.28×10^{-4}	J. Korenaga (2006)
	^{232}Th	1	
	^{235}U	7.2×10^{-3}	
	^{238}U	0.9927	
Radiogenic heat per unit mass (h_{i}, μW kg^{-1})	^{40}K	27.9	D. L. Turcotte & G. Schubert (2002)
	^{232}Th	26.9	
	^{235}U	569	
	^{238}U	93.7	

ORCID iDs

Samantha Gilbert-Janizek https://orcid.org/0009-0004-8402-9608
Rory K. Barnes https://orcid.org/0000-0001-6487-5445
Peter E. Driscoll https://orcid.org/0000-0001-6241-3925
Nicholas F. Wogan https://orcid.org/0000-0002-0413-3308
Avi M. Mandell https://orcid.org/0000-0002-8119-3355
Jessica L. Birky https://orcid.org/0000-0002-7961-6881
Ludmila Carone https://orcid.org/0000-0001-9355-3752

References

Abbot, D. S., Voigt, A., Li, D., et al. 2013, JGRD, 118, 6017
Ackerman, A. S., & Marley, M. S. 2001, ApJ, 556, 872
Al Asad, M., & Lau, H. C. 2024, SciA, 10, eadp1991
Alcabes, O. D., Olson, S., & Abbot, D. S. 2020, MNRAS, 492, 2572
Alfè, D., Gillan, M., & Price, G. D. 2002, E&PSL, 195, 91
Allan, R. P., Willett, K. M., John, V. O., & Trent, T. 2022, JGRD, 127, e2022JD036728
Armann, M., & Tackley, P. J. 2012, JGRE, 117, E12003
Arney, G., Domagal-Goldman, S. D., Meadows, V. S., et al. 2016, AsBio, 16, 873
Arney, G. N. 2019, ApJL, 873, L7
Arney, G. N., Meadows, V. S., Domagal-Goldman, S. D., et al. 2017, ApJ, 836, 49
Atri, D., & Mogan, S. R. C. 2021, MNRAS: Letters, 500, L1
Avice, G., Marty, B., Burgess, R., et al. 2018, GeCoA, 232, 82
Baldridge, A. M., Hook, S. J., Grove, C. I., & Rivera, G. 2009, RSEnv, 113, 711
Baraffe, I., Homeier, D., Allard, F., & Chabrier, G. 2015, A&A, 577, A42
Barley, M. E., Bekker, A., & Krapež, B. 2005, E&PSL, 238, 156
Barnes, R., Luger, R., Deitrick, R., et al. 2020, PASP, 132, 024502
Bartman, F. L. 1980, A Time Variable Model of Earth's Albedo Tech. Rep. NASA-CR-159259, NASA
Batalha, N. E., Marley, M. S., Lewis, N. K., & Fortney, J. J. 2019, ApJ, 878, 70
Berner, R. A., Lasaga, A. C., & Garrels, R. M. 1983, AmJS, 283, 641
Bialik, O. M., Sisma-Ventura, G., Vogt-Vincent, N., Silverman, J., & Katz, T. 2022, NatSR, 12, 15970
Blake, R. E., Chang, S. J., & Lepland, A. 2010, Natur, 464, 1029
Blanchard, I., Siebert, J., Borensztajn, S., & Badro, J. 2017, GChPL, 5, 1
Boehler, R. 1996, AREPS, 24, 15
Boukaré, C.-É., Badro, J., & Samuel, H. 2025, Natur, 640, 114
Boyd, P. W., Claustre, H., Levy, M., Siegel, D. A., & Weber, T. 2019, Natur, 568, 327
Brent, R. P. 2013, Algorithms for Minimization without Derivatives (Courier Corporation)
Brewer, A. 1949, QJRMS, 75, 351
Cameron, E. M., Blum, T. B., Cavosie, A. J., et al. 2024, AmMin, 109, 1670
Campbell, I. H., & O'Neill, H. S. C. 2012, Natur, 483, 553
Carlson, R. W., Garnero, E., Harrison, T. M., et al. 2014, AREPS, 42, 151
Carone, L., Barnes, R., Noack, L., et al. 2025, A&A, 693, A303
Carpenter, S. J., & Lohmann, K. C. 1992, GeCoA, 56, 1837
Carroll, D., Menemenlis, D., Dutkiewicz, S., et al. 2022, GBioC, 36, e2021GB007162
Catling, D. C., & Kasting, J. F. 2017, Atmospheric Evolution on Inhabited and Lifeless Worlds (Cambridge Univ. Press)
Catling, D. C., & Zahnle, K. J. 2009, SciAm, 300, 36
Catling, D. C., & Zahnle, K. J. 2020, SciA, 6, eaax1420
Catling, D. C., Zahnle, K. J., & McKay, C. P. 2001, Sci, 293, 839
Chadney, J., Galand, M., Unruh, Y., Koskinen, T., & Sanz-Forcada, J. 2015, Icar, 250, 357
Chao, K.-H., deGraffenried, R., Lach, M., et al. 2021, ChEG, 81, 125735
Charette, M. A., & Smith, W. H. 2010, Ocgpy, 23, 112
Charnay, B., Forget, F., Wordsworth, R., et al. 2013, JGRD , 118, 10414
Chave, K. E., & Suess, E. 1970, LimOc, 15, 633
Chu, D. 2019, Remote Sensing of Land Use and Land Cover in Mountain Region: a Comprehensive Study at the Central Tibetan Plateau (Springer), 195
Clark, R. N., Swayze, G. A., Wise, R., et al. 2003, USGS Digital Spectral Library splib05a, Open File Report 03-395 (U.S. Geological Survey), http://pubs.usgs.gov/of/2003/ofr-03-395/datatable.html
Cockell, C. S. 2014, RSPTA, 372, 20130082
Cogné, J.-P., & Humler, E. 2004, E&PSL, 227, 427
Condie, K. C., Aster, R. C., & Van Hunen, J. 2016, GeoFr, 7, 543
Constantinou, T., Shorttle, O., Cranmer, M., & Rimmer, P. B. 2026, MNRAS, 547, stag316
Coogan, L. A., & Dosso, S. E. 2015, E&PSL, 415, 38
Costa, A., Caricchi, L., & Bagdassarov, N. 2009, GGG, 10, Q03010
de Pater, I., & Lissauer, J. 2010, Planetary Sciences (Cambridge Univ. Press)
de Wit, M. J., & Furnes, H. 2016, SciA, 2, e1500368
Dessert, C., Dupré, B., Gaillardet, J., François, L. M., & Allègre, C. J. 2003, ChGeo, 202, 257
Dole, S. H., & Asimov, I. 1964, Planets for man (Random House)
Driese, S. G., Jirsa, M. A., Ren, M., et al. 2011, PreR, 189, 1
Driscoll, P., & Bercovici, D. 2013, Icar, 226, 1447
Driscoll, P., & Bercovici, D. 2014, PEPI, 236, 36
Driscoll, P. E., & Barnes, R. 2015, AsBio, 15, 739
Dziewonski, A. M., & Anderson, D. L. 1981, PEPI, 25, 297
Eide, M., Olsen, A., Ninnemann, U. S., & Johannessen, T. 2017, GBioC, 31, 515
Elkins-Tanton, L. T. 2008, E&PSL, 271, 181
Elkins-Tanton, L. T. 2012, AREPS, 40, 113
Etheridge, D. M., Steele, L., Langenfelds, R. L., et al. 1996, JGRD , 101, 4115
Etiope, G., & Sherwood Lollar, B. 2013, RvGeo, 51, 276
Fan, S., Li, C., Li, J.-Z., et al. 2019, ApJL, 882, L1
Farquhar, J., Zerkle, A. L., & Bekker, A. 2011, PhoRe, 107, 11
Fauchez, T., Arney, G., Kopparapu, R. K., & Goldman, S. D. 2018, AIMSG, 4, 180
Faure, P., Bouhifd, M. A., Boyet, M., et al. 2020, GeCoA, 275, 83
Feely, R. A., Sabine, C. L., Takahashi, T., Wanninkhof, R., et al. 2001, Ocgpy, 14, 18
Feinberg, L. D., Sitarski, B. N., McElwain, M. W., et al. 2026, arXiv:2601.11803
Fleming, J. R. 1998, Historical Perspectives on Climate Change (Oxford Univ. Press)
Foley, B. J. 2015, ApJ, 812, 36
Foley, B. J., & Driscoll, P. E. 2016, GGG, 17, 1885
Ford Cochran, M., & Berner, R. A. 1996, ChGeo, 132, 71
Frank, E. A., Meyer, B. S., & Mojzsis, S. J. 2014, Icar, 243, 274
Gaillard, F., Bernadou, F., Roskosz, M., et al. 2022, E&PSL, 577, 117255
Gale, A., Dalton, C. A., Langmuir, C. H., Su, Y., & Schilling, J.-G. 2013, GGG, 14, 489
Garcia, R., Barnes, R., Driscoll, P. E., Meadows, V. S., & Gialluca, M. 2026, PSJ, 7, 120
Gebauer, S., Grenfell, J., Stock, J. W., et al. 2017, AsBio, 17, 27
Geboy, N. J., Kaufman, A. J., Walker, R. J., et al. 2013, PreR, 238, 199
Genda, H. 2016, GeocJ, 50, 27
Gialluca, M. T., Barnes, R., Meadows, V. S., et al. 2024, PSJ, 5, 137
Gillmann, C., Way, M. J., Avice, G., et al. 2022, SSRv, 218, 56
Godolt, M., Grenfell, J., Kitzmann, D., et al. 2016, A&A, 592, A36
Godolt, M., Grenfell, J., Hamann-Reinus, A., et al. 2015, P&SS, 111, 62
Goldblatt, C., Claire, M. W., Lenton, T. M., et al. 2009, NatGe, 2, 891
Gordon, I. E., Rothman, L. S., Hill, C., et al. 2017, JQSRT, 203, 3
Gough, D. 1981, SoPh, 74, 21
Grießmeier, J.-M., Stadelmann, A., Penz, T., et al. 2004, A&A, 425, 753
Gronoff, G., Arras, P., Baraka, S., et al. 2020, JGRA, 125, e2019JA027639
Grotzinger, J. P. 1989, in Controls on Carbonate Platforms and Basin Development, ed. P. D. Crevello, Vol. 44 (SEPM Society for Sedimentary Geology), 79
Grotzinger, J. P., & James, N. P. 2000, in Carbonate Sedimentation and Diagenesis in the Evolving Precambrian World, ed. J. P. Grotzinger & N. P. James, Vol. 67 (SEPM Society for Sedimentary Geology), 3
Grotzinger, J. P., & Kasting, J. F. 1993, JG, 101, 235
Gunell, H., Maggiolo, R., Nilsson, H., et al. 2018, A&A, 614, L3
Halevy, I., & Bachan, A. 2017, Sci, 355, 1069
Hamano, K., Abe, Y., & Genda, H. 2013, Natur, 497, 607
Haqq-Misra, J., Kopparapu, R. K., Batalha, N. E., Harman, C. E., & Kasting, J. F. 2016, ApJ, 827, 120
Harrison, E. F., Minnis, P., Barkstrom, B., et al. 1990, JGRD , 95, 18687
Hashimoto, G. L., & Abe, Y. 2001, JGRE, 106, 14675
Hawkins, E., & Sutton, R. 2016, BAMS, 97, 963
Hawkins, E., Ortega, P., Suckling, E., et al. 2017, BAMS, 98, 1841
Hébrard, E., & Marty, B. 2014, E&PSL, 385, 40
Held, I. M., & Soden, B. J. 2000, Annu. Rev. Energy, 25, 441
Helling, C. 2019, AREPS, 47, 583
Herzberg, C., Condie, K., & Korenaga, J. 2010, E&PSL, 292, 79

Hirose, K., Labrosse, S., & Hernlund, J. 2013, AREPS, 41, 657
Hirth, G., & Kohlstedt, D. 2003, in Inside the Subduction Factory, ed. J. Eiler, Vol. 138 (AGU), 83
Hoffman, P. F., Abbot, D. S., Ashkenazy, Y., et al. 2017, SciA, 3, e1600983
Hren, M., Tice, M., & Chamberlain, C. 2009, Natur, 462, 205
Jackson, M. G., Carlson, R. W., Kurz, M. D., et al. 2010, Natur, 466, 853
Jaupart, C., Labrosse, S., Lucazeau, F., & Mareschal, J. 2015, in Treatise on Geophysics. Temperatures, Heat and Energy in the Mantle of the Earth, ed. G. Schubert (2nd ed.; Elsevier), 223
Jeanloz, R., & Morris, S. 1986, AREPS, 14, 377
Jiang, L.-Q., Carter, B. R., Feely, R. A., Lauvset, S. K., & Olsen, A. 2019, NatSR, 9, 18624
Jones, E., Oliphant, T., Peterson, P., et al. 2001, SciPy: Open Source Scientific Tools for Python, https://www.scipy.org
Kadoya, S., & Tajika, E. 2019, ApJ, 875, 7
Kah, L. C., & Riding, R. 2007, Geo, 35, 799
Kaltenegger, L., Traub, W. A., & Jucks, K. W. 2007, ApJ, 658, 598
Kanzaki, Y., & Murakami, T. 2015, GeCoA, 159, 190
Kargel, J. S., Leonard, G. J., Bishop, M. P., Kääb, A., & Raup, B. H. 2014, Global Land Ice Measurements from Space (Springer)
Kasting, J. F. 1988, Icar, 74, 472
Kasting, J. F., Pollack, J. B., & Ackerman, T. P. 1984, Icar, 57, 335
Kasting, J. F., Whitmire, D. P., & Reynolds, R. T. 1993, Icar, 101, 108
Katsura, T., Yamada, H., Shinmei, T., et al. 2003, PEPI, 136, 11
Katsura, T., Yamada, H., Nishikawa, O., et al. 2004, JGRB , 109, B02209
Keller, T., & Suckale, J. 2019, GeoJI, 219, 185
Kharecha, P., Kasting, J., & Siefert, J. 2005, Gbio, 3, 53
Kinzler, R. J., & Grove, T. L. 1992, JGRB, 97, 6885
Kipping, D. 2025, AsBio, 25, 323
Kirchner, J. W. 1989, RvGeo, 27, 223
Kirchner, J. W. 2002, ClCh, 52, 391
Kirchner, J. W. 2003, ClCh, 58, 21
Kivelson, M. G., & Bagenal, F. 2014, in Encyclopedia of the Solar System, ed. T. Spohn (3rd ed.; Elsevier), 137
Klein, E. M., & Langmuir, C. H. 1987, JGRB, 92, 8089
Komacek, T. D., & Abbot, D. S. 2019, ApJ, 871, 245
Kopparapu, R. K., Ramirez, R., Kasting, J. F., et al. 2013, ApJ, 765, 131
Korenaga, J. 2006, in Archean Geodynamics and Environments, ed. K. Benn, Vol. 164 (AGU), 7
Korenaga, J. 2008a, TeNov, 20, 419
Korenaga, J. 2008b, RvGeo, 46, RG2007
Krissansen-Totton, J., Arney, G. N., & Catling, D. C. 2018, PNAS, 115, 4105
Krissansen-Totton, J., Fortney, J. J., Nimmo, F., & Wogan, N. 2021, AGUA, 2, e2020AV000294
Kuipers, G., Beunk, F. F., & van der Wateren, F. M. 2013, GeolT, 29, 218
Kump, L. R. 2008, Natur, 451, 277
Labrosse, S. 2003, PEPI, 140, 127
Labrosse, S., Hernlund, J., & Coltice, N. 2007, Natur, 450, 866
Lacis, A. A., Schmidt, G. A., Rind, D., & Ruedy, R. A. 2010, Sci, 330, 356
Lammer, H., Zerkle, A. L., Gebauer, S., et al. 2018, A&ARv, 26, 2
Laneuville, M., Kameya, M., & Cleaves, H. J. 2018, AsBio, 18, 897
Lau, H. C., Mitrovica, J. X., Austermann, J., et al. 2016, JGRB, 121, 6991
Le Moigne, F. A. 2019, FrMaS, 6, 634
Li, J., Jian, H., Chen, Y. J., et al. 2015, GeoRL, 42, 2656
Lichtenberg, T., Bower, D. J., Hammond, M., et al. 2021, JGRE, 126, e2020JE006711
Lincowski, A. P., Meadows, V. S., Crisp, D., et al. 2018, ApJ, 867, 76
Loeb, N. G., Wielicki, B. A., Doelling, D. R., et al. 2009, JCli, 22, 748
López-Morales, M., Currie, T., Teske, J., et al. 2019, BAAS, 51, 162
Lovelock, J. 2000, The Ages of Gaia: A Biography of Our Living Earth (Oxford Univ. Press)
Lovelock, J. 2016, Gaia: A New Look at Life on Earth (Oxford Univ. Press)
Lovelock, J. E. 1983, in Biomineralization and Biological Metal Accumulation, ed. P. Westbroek (Springer), 15
Lovelock, J. E., & Margulis, L. 1974, Tell, 26, 2
Luger, R., & Barnes, R. 2015, AsBio, 15, 119
Lustig-Yaeger, J., Meadows, V. S., Crisp, D., Line, M. R., & Robinson, T. D. 2023, PSJ, 4, 170
Lyons, T. W., Reinhard, C. T., & Planavsky, N. J. 2014, Natur, 506, 307
Mamajek, E., & Stapelfeldt, K. 2023, NASA ExEP Mission Star List for the Habitable Worlds Observatory Tech. Rep., NASA Jet Propulsion Laboratory and California Institute of Technology
Maruyama, S., Santosh, M., & Azuma, S. 2018, GeoFr, 9, 1033
Mauritsen, T., Stevens, B., Roeckner, E., et al. 2012, JAMES, 4, M00A01
McDonough, W. F. 2025, arXiv:2505.02641
Meadows, V. S., & Crisp, D. 1996, JGRE, 101, 4595
Meadows, V. S., Reinhard, C. T., Arney, G. N., et al. 2018, AsBio, 18, 630
Millero, F. J. 2005, Chemical Oceanography, 30 (3rd ed.; CRC Press)
Mitrovica, J., & Forte, A. 2004, E&PSL, 225, 177
Mockler, S. 1995, Water Vapor in the Climate System Special Report, American Geophysical Union
Nakagawa, T., & Tackley, P. J. 2012, E&PSL, 329, 1
National Academies of Sciences, Engineering, and Medicine 2021, Pathways to Discovery in Astronomy and Astrophysics for the 2020s (The National Academies Press)
Nelder, J. A., & Mead, R. 1965, CompJ, 7, 308
Newman, M. J., & Rood, R. T. 1977, Sci, 198, 1035
Nicholson, A. E., Wilkinson, D. M., Williams, H. T., & Lenton, T. M. 2018, MNRAS, 477, 727
Nikolaou, A., Katyal, N., Tosi, N., et al. 2019, ApJ, 875, 11
Nimmo, F. 2002, Geo, 30, 987
Nowicki, M., DeVries, T., & Siegel, D. A. 2022, GBioC, 36, e2021GB007083
Ojakangas, R. W., Srinivasan, R., Hegde, V., Chandrakant, S., & Srikantia, S. 2014, CSci, 106, 387
O'Leary, M. H. 1981, PChem, 20, 553
Parai, R., & Mukhopadhyay, S. 2018, Natur, 560, 223
Passow, U., & Carlson, C. A. 2012, MEPS, 470, 249
Patel, V. K., & Kuttippurath, J. 2023, OLAR, 2, 0015
Patočka, V., Šrámek, O., & Tosi, N. 2020, PEPI, 305, 106457
Paulson, A., Zhong, S., & Wahr, J. 2005, GeoJI, 163, 357
Pavlov, A. A., Brown, L. L., & Kasting, J. F. 2001, JGRE, 106, 23267
Pavlov, A. A., Kasting, J. F., Brown, L. L., Rages, K. A., & Freedman, R. 2000, JGRE , 105, 11981
Pilson, M. E. 2012, An Introduction to the Chemistry of the Sea (2nd ed.; Cambridge Univ. Press)
Quay, P., Sonnerup, R., Westby, T., Stutsman, J., & McNichol, A. 2003, GBioC, 17, 1004
Ramanathan, V., Cess, R., Harrison, E., et al. 1989, Sci, 243, 57
Randel, W., & Park, M. 2019, GRD, 124, 7018
Ray, R. D., Eanes, R., & Chao, B. F. 1996, Natur, 381, 595
Roberson, A. L., Roadt, J., Halevy, I., & Kasting, J. 2011, Gbio, 9, 313
Robinson, T. D. 2018, in Handbook of Exoplanets, ed. H. J. Deeg & J. A. Belmonte (Springer), 3137
Robinson, T. D., Meadows, V. S., Crisp, D., et al. 2011, AsBio, 11, 393
Rodler, F., & López-Morales, M. 2014, ApJ, 781, 54
Rose, B. E., Cronin, T. W., & Bitz, C. M. 2017, ApJ, 846, 28
Rothman, L. S., Gordon, I., Barber, R., et al. 2010, JQSRT, 111, 2139
Rudge, J. F. 2018, JGRB , 123, 10534
Rugheimer, S., & Kaltenegger, L. 2018, ApJ, 854, 19
Sagan, C., & Mullen, G. 1972, Sci, 177, 52
Santerne, A., Brugger, B., Armstrong, D., et al. 2018, NatAs, 2, 393
Schaefer, L., & Elkins-Tanton, L. T. 2018, RSPTA, 376, 20180109
Schaefer, L., Wordsworth, R. D., Berta-Thompson, Z., & Sasselov, D. 2016, ApJ, 829, 63
Schwieterman, E. W., Reinhard, C. T., Olson, S. L., Harman, C. E., & Lyons, T. W. 2019a, ApJ, 878, 19
Schwieterman, E. W., Reinhard, C. T., Olson, S. L., et al. 2019b, ApJ, 874, 9
Schwieterman, E. W., Robinson, T. D., Meadows, V. S., Misra, A., & Domagal-Goldman, S. 2015, ApJ, 810, 57
Schwieterman, E. W., Kiang, N. Y., Parenteau, M. N., et al. 2018, AsBio, 18, 663
Seales, J., & Lenardic, A. 2020, GGG, 21, e2020GC009106
Segura, A., Kasting, J. F., Meadows, V., et al. 2005, AsBio, 5, 706
Segura, A., Walkowicz, L. M., Meadows, V., Kasting, J., & Hawley, S. 2010, AsBio, 10, 751
Shaik, I., Nagamani, P., Yadav, S., Manmode, Y., & Rao, G. S. 2025, MarCh, 268, 104483
Sheldon, N. D. 2006, PreR, 147, 148
Shim, S.-H. 2014, Search for Life Beyond the Solar System. Exoplanets, Biosignatures & Instruments, ed. D. Apai & P. Gabor, (NASA),
Shue, J.-H., Song, P., Russell, C., et al. 1998, JGRA, 103, 17691
Siegel, D. A., DeVries, T., Cetinić, I., & Bisson, K. M. 2023, ARMS, 15, 329
Sleep, N. H., & Zahnle, K. 2001, JGRE, 106, 1373
Solomon, S., Qin, D., Manning, M., et al. 2007, Climate Change 2007: The Physical Science Basis: Working Group I contribution to the Fourth Assessment Report of the IPCC NCAR Report, 374
Stalport, F., Coll, P., Cabane, M., et al. 2005, GeoRL, 32, L23205
Steinberger, B., & Calderwood, A. R. 2006, GeoJI, 167, 1461
Stueeken, E. E., Som, S., Claire, M., et al. 2020, SSRv, 216, 31
Sumner, D. Y., & Grotzinger, J. P. 1996, Geo, 24, 119

Takei, Y., & Holtzman, B. K. 2009, JGRB , 114, 114
Thompson, M. A., Krissansen-Totton, J., Wogan, N., Telus, M., & Fortney, J. J. 2022, PNAS, 119, e2117933119
Tian, F., Chassefière, E., Leblanc, F., & Brain, D. 2013, in Comparative Climatology of Terrestrial Planets, ed. S. J. Mackwell, A. A. Simon-Miller, J. W. Harder, & M. A. Bullock (Univ. Arizona Press), 567
Toon, O. B., McKay, C., Ackerman, T., & Santhanam, K. 1989, JGRD, 94, 16287
Trenberth, K. E. 1998, ClCh, 39, 667
Trenberth, K. E., Christy, J. R., & Olson, J. G. 1987, JGRD, 92, 14815
Tuchow, N. W., Harada, C. K., Mamajek, E. E., et al. 2025, PASP, 137, 104402
Turcotte, D. L., & Schubert, G. 2002, Geody (Cambridge Univ. Press)
Tyndall, J. 1861, LEDPM, 22, 169
United States Committee on Extension to the Standard Atmosphere 1976, U.S. Standard Atmosphere (1976) Technical Memorandum NOAA-S/T-76-1562, National Oceanic and Atmospheric Administration
Vial, J., Dufresne, J.-L., & Bony, S. 2013, ClDy, 41, 3339
Virtanen, P., Gommers, R., Oliphant, T. E., et al. 2020, NaMet, 17, 261
Vladilo, G., Murante, G., Silva, L., et al. 2013, ApJ, 767, 65
Volk, T. 2002, ClCh, 52, 423
Walker, J. C., Hays, P., & Kasting, J. F. 1981, JGRC , 86, 9776
Walter, M., Buick, R., & Dunlop, J. 1980, Natur, 284, 443
Watanabe, K., Ohtani, E., Kamada, S., et al. 2014, PEPI, 237, 65
Watson, A. J., Donahue, T. M., & Walker, J. C. 1981, Icar, 48, 150
Way, M. J., Del Genio, A. D., Aleinov, I., et al. 2018, ApJS, 239, 24
West, A. J. 2012, Geo, 40, 811
Wielicki, B. A., Barkstrom, B. R., Harrison, E. F., et al. 1996, BAMS, 77, 853
Wild, B., Gerrits, R., & Bonneville, S. 2022, npjMD, 6, 98
Wilhelm, C., Barnes, R., Deitrick, R., & Mellman, R. 2022, PSJ, 3, 13
Williams, G. E. 2005, JGSoc, 162, 111
Windsor, J. D., Robinson, T. D., Kopparapu, R. k., et al. 2023, PSJ, 4, 94
Wogan, N., Krissansen-Totton, J., & Catling, D. C. 2020, PSJ, 1, 58
Wogan, N., Lopez, J., Batalha, N., & Fortney, J. 2025a, Resampled Opacity Databases for PICASO from the Photochem model, v1.0.0, Zenodo, doi:10.5281/zenodo.17381172
Wogan, N. F., Catling, D. C., Zahnle, K. J., & Claire, M. W. 2022, PNAS, 119, e2205618119
Wogan, N. F., Batalha, N. E., Zahnle, K., et al. 2025b, PSJ, 6, 256
Wolf, E. T., Kopparapu, R., Haqq-Misra, J., & Fauchez, T. J. 2022, PSJ, 3, 7
Wolf, E. T., Shields, A. L., Kopparapu, R. K., Haqq-Misra, J., & Toon, O. B. 2017, ApJ, 837, 107
Wordsworth, R., & Pierrehumbert, R. 2014, ApJL, 785, L20
Yang, J., Leconte, J., Wolf, E. T., et al. 2016, ApJ, 826, 222
Young, A. V., Robinson, T. D., Krissansen-Totton, J., et al. 2024, NatAs, 8, 101
Young, G. M., Brunn, V. V., Gold, D. J., & Minter, W. 1998, JG, 106, 523
Zahnle, K. J., Gacesa, M., & Catling, D. C. 2019, GeCoA, 244, 56
Zahnle, K. J., Lupu, R., Catling, D. C., & Wogan, N. 2020, PSJ, 1, 11
Zerkle, A. L., Claire, M. W., Domagal-Goldman, S. D., Farquhar, J., & Poulton, S. W. 2012, NatGe, 5, 359
Zhuang, D., Yan, H., Tucker, M. E., et al. 2018, ChGeo, 500, 64
Zsom, A., Kaltenegger, L., & Goldblatt, C. 2012, Icar, 221, 603